Astronomy & Astrophysics

The Earliest Phases of Star Formation (EPoS): a *Herschel* key project

The thermal structure of low-mass molecular cloud cores[*],[**],[***]

R. Launhardt[1], A. M. Stutz[1], A. Schmiedeke[2,1], Th. Henning[1], O. Krause[1], Z. Balog[1], H. Beuther[1], S. Birkmann[3,1],
M. Hennemann[4,1], J. Kainulainen[1], T. Khanzadyan[5], H. Linz[1], N. Lippok[1], M. Nielbock[1], J. Pitann[1], S. Ragan[1],
C. Risacher[6,5], M. Schmalzl[7,1], Y. L. Shirley[8], B. Stecklum[9], J. Steinacker[10,1], and J. Tackenberg[1]

1   Max-Planck-Institut für Astronomie (MPIA), Königstuhl 17, 69117 Heidelberg, Germany
    e-mail: `rl@mpia.de`
2   Universität zu Köln, Zülpicher Strasse 77, 50937 Köln, Germany
3   ESA/ESTEC, Keplerlaan 1, Postbus 299, 2200 AG Noordwijk, The Netherlands
4   Laboratoire AIM Paris-Saclay, Service d'Astrophysique, CEA/IRFU – CNRS/INSU – Université Paris Diderot,
    Orme des Merisiers Bat. 709, 91191 Gif-sur-Yvette Cedex, France
5   Max-Planck-Institut für Radioastronomie (MPIfR), Auf dem Hügel 69, 53121 Bonn, Germany
6   SRON Netherlands Institute for Space Research, PO Box 800, 9700 AV Groningen, The Netherlands
7   Leiden Observatory, Leiden University, PO Box 9513, 2300 RA, Leiden, The Netherlands
8   Steward Observatory, 933 North Cherry Avenue, Tucson, AZ 85721, USA
9   Thüringer Landessternwarte Tautenburg, Sternwarte 5, 07778 Tautenburg, Germany
10 Institut de Planétologie et d'Astrophysique de Grenoble, Université de Grenoble, BP 53, 38041 Grenoble Cedex 9, France

ABSTRACT

Context. The temperature and density structure of molecular cloud cores are the most important physical quantities that determine the course of the protostellar collapse and the properties of the stars they form. Nevertheless, density profiles often rely either on the simplifying assumption of isothermality or on observationally poorly constrained model temperature profiles. The instruments of the *Herschel* satellite provide us for the first time with both the spectral coverage and the spatial resolution that is needed to directly measure the dust temperature structure of nearby molecular cloud cores.

Aims. With the aim of better constraining the initial physical conditions in molecular cloud cores at the onset of protostellar collapse, in particular of measuring their temperature structure, we initiated the guaranteed time key project (GTKP) "The Earliest Phases of Star Formation" (EPoS) with the *Herschel* satellite. This paper gives an overview of the low-mass sources in the EPoS project, the *Herschel* and complementary ground-based observations, our analysis method, and the initial results of the survey.

Methods. We study the thermal dust emission of 12 previously well-characterized, isolated, nearby globules using FIR and submm continuum maps at up to eight wavelengths between 100 μm and 1.2 mm. Our sample contains both globules with starless cores and embedded protostars at different early evolutionary stages. The dust emission maps are used to extract spatially resolved SEDs, which are then fit independently with modified blackbody curves to obtain line-of-sight-averaged dust temperature and column density maps.

Results. We find that the thermal structure of all globules (mean mass 7 $M_\odot$) is dominated by external heating from the interstellar radiation field and moderate shielding by thin extended halos. All globules have warm outer envelopes (14–20 K) and colder dense interiors (8–12 K) with column densities of a few 10^{22} cm^{-2}. The protostars embedded in some of the globules raise the local temperature of the dense cores only within radii out to about 5000 AU, but do not significantly affect the overall thermal balance of the globules. Five out of the six starless cores in the sample are gravitationally bound and approximately thermally stabilized. The starless core in CB 244 is found to be supercritical and is speculated to be on the verge of collapse. For the first time, we can now also include externally heated starless cores in the L_{smm}/L_{bol} vs. T_{bol} diagram and find that $T_{bol} < 25$ K seems to be a robust criterion to distinguish starless from protostellar cores, including those that only have an embedded very low-luminosity object.

Key words. stars: formation – stars: low-mass – stars: protostars – ISM: clouds – dust, extinction – infrared: ISM

---

1. Introduction and scientific goals

The formation of stars from diffuse interstellar matter (ISM) is one of the most fundamental and fascinating transformation processes in the universe. Stars form through the gravitational collapse of the densest and coldest cores inside molecular clouds. The initial temperature and density structure of such cores are the most important physical quantities that determine the course of the collapse and its stellar end product (e.g., Larson 1969; Penston 1969; Shu 1977; Shu et al. 1987; Commerçon et al. 2010); however, deriving the physical properties of such cores from observations and thus constraining theoretical collapse models is a nontrivial problem. More than 98% of the

core mass is locked up in H_2 molecules and in He atoms that do not have a permanent electric dipole moment and that therefore do not radiate when cold. The excitation of ro-vibrational and electronic states of H_2 requires temperatures much higher than are present in these cores (e.g., Burton 1992). This problem is usually overcome by observing radiation from heavier asymmetric molecules, which are much less abundant, but have rotational transitions that are easily excited via collisions with hydrogen molecules (e.g., CO, CS; Bergin & Tafalla 2007). However, at the high densities ($n_H \geq 10^6$ cm^{-3}) and low temperatures ($T \leq 10$ K; e.g., Crapsi et al. 2007) inside such cloud cores, most of these heavier molecules freeze out from the gas phase and settle on dust grains, where they remain "invisible" (e.g., Bergin & Langer 1997; Charnley 1997; Caselli et al. 1999; Hily-Blant et al. 2010). The few remaining "slow depleters" (e.g., NH_3 or N_2H^+, $n_{crit(1-0)} \sim 10^5$ cm^{-3}) or deuterated molecular ions that profit from the gas phase depletion of CO (e.g., N_2D^+ and DCO^+; Caselli et al. 2002) can be used to identify prestellar cores and infer their kinematical and chemical properties. However, the respective observational data, in particular for the deuterated species, are still sparse and their complex chemical evolution has not been understood well enough yet to derive reliable density profiles. A very promising and robust alternative tracer for the matter in such cores is therefore the dust, which constitutes about 1% of the total mass of the ISM in the solar neighborhood.

Interstellar dust can be traced by its effect on the attenuation of background light (Lada et al. 1994), scattering of ambient starlight ("cloudshine": Foster & Goodman 2006; "coreshine": Steinacker et al. 2010; Pagani et al. 2010), or by its thermal emission (e.g., Smith et al. 1979). In principle, it is preferable to use extinction measurements to trace the column density because they are to first order independent of the dust temperature (unlike emission). However, extinction measurements require that at least some measurable amount of light from background sources passes through the cloud, which is no longer the case at the highest column densities in the core centers ($N_H >$ few $\times 10^{22}$ cm^{-2}). Another limitation of this technique is the inability to exactly measure the extinction toward individual sources with a priori unknown spectral energy distributions (SEDs), and that it relies on statistically relevant ensembles of background stars, which restricts this method to fields with high background star density (i.e., close to the Galactic plane) and limits the effective angular resolution. Consequently, most attempts to derive the density structure of cloud cores from extinction maps have been done in the near-infrared (NIR) and have targeted less-opaque cloud cores and envelopes ($A_V \leq 20$ mag; e.g., Alves et al. 2001; Lada et al. 2004; Kandori et al. 2005; Kainulainen et al. 2006). Going to wavelengths longer than optical or NIR, where the opacity is lower, also usually does not help much since the background stars also become dimmer at longer wavelengths.

In addition to the conventional NIR extinction mapping techniques, mid and far-IR (MIR, FIR) shadows, or absorption features, where the densest portions of cores are observed in absorption against the background interstellar radiation field (ISRF), can be used to map structure at high resolution. Provided the absolute background level in the images can be accurately calibrated, they provide good measurements of the line-of-sight (LoS) projected structure and column density in very dense regions. Such features have been used to study cores at 8, 24, and 70 μm (Bacmann et al. 2000; Stutz et al. 2009a,b; Tobin et al. 2010). One of the main results from these studies is that the LoS-projected geometry often drastically departs from spherical geometry both in the prestellar and protostellar phases.

Observations of scattered interstellar radiation in the form of cloudshine, although permitting certain diagnostics of cloud structure (Padoan et al. 2006; Juvela et al. 2006), also do not trace the interiors of dense cores. Scattered MIR interstellar light can penetrate most low-mass cores producing coreshine (Steinacker et al. 2010). However, the effect requires the presence of larger dust grains for scattering to be efficient and is visible in only half of the cores (Pagani et al. 2010). Beside the advantage of an only weak dependence on temperature effects, scattered light is also sensitive to the 3D structure of the core and could allow the actual density structure to be traced. But to use this information, the outer radiation field and the scattering phase function of the dust particles needs to be known precisely, which poses a problem for many cores in the complex environment of star-formation regions.

Hence, the thermal emission from dust grains remains as a superior tracer of matter in the coldest and densest molecular cloud cores where stars form. Consequently, most of our current information on the density structure of prestellar cores and protostellar envelopes comes from submm and mm dust continuum maps (e.g., Ward-Thompson et al. 1994, 1999; Launhardt & Henning 1997; Henning & Launhardt 1998; Evans et al. 2001; Motte & André 2001; Shirley et al. 2002; André et al. 2004; Kirk et al. 2005; Kauffmann et al. 2008; Launhardt et al. 2010). Nevertheless, ultimately we will need to combine information from different tracers and methods to calibrate the dust opacities as well as to derive quantities that cannot be derived from the dust emission alone (see discussion and outlook at the end of Sect. 7).

To relate the thermal dust emission at a given wavelength to the mass of the emitting matter, three main pieces of information are needed: the temperature of the dust grains, T_d, their mass absorption coefficient, κ_ν, and the gas-to-dust mass ratio. The mean opacity of the dust mixture is a function of grain optical properties, wavelength, and temperature (e.g., Henning & Stognienko 1996; Agladze et al. 1996; Draine 2003; Boudet et al. 2005) and may actually vary locally and in time as a function of the physical conditions. However, observational constraints of such opacity variations are very difficult to obtain due to various degeneracies and often insufficient data (e.g., Shetty et al. 2009a,b; Shirley et al. 2011; Kelly et al. 2012). Therefore, the conversion of flux into mass is usually done by adopting one or the other "standard" dust model that is assumed to be constant throughout the region of interest.

The definition of a common temperature for the dust requires that the grains are in local thermal equilibrium (LTE), which is fortunately the case, to first order, in the well-shielded dense interiors of molecular cloud cores where collisions with H_2 molecules occur frequently and stochastic heating of individual grains (timescales $\tau_{cool} \ll \tau_{heat}$), e.g., by UV photons, does not play a significant role (e.g., Siebenmorgen et al. 1992; Pavlyuchenkov et al. 2012). However, with typical dust temperatures inside such dense cores being in the range 8–15 K (e.g., di Francesco et al. 2007; Bergin & Tafalla 2007), the submm emission represents only the Rayleigh-Jeans tail of the Planck spectrum. Therefore, the dust temperature is only very poorly constrained by these data, which results in large uncertainties in the derived total masses and in the radial density profiles. E.g., at $\lambda = 1$ mm, where the thermal emission of low-mass cores is practically always optically thin, more than twice the amount of 8 K dust is needed to emit the same flux density as 12 K dust. Hence, a dust temperature estimate of 10 ± 2 K still leaves the mass and the (local) column density uncertain to a factor of two. The effect of unaccounted temperature gradients

on the derived density profile is even more significant and leads to large uncertainties in the observational constraints on protostellar collapse models. Earlier attempts to reconstruct the dust temperature profiles of starless and star-forming cores from, e.g., SCUBA 450/850 μm flux ratio maps or self-consistent radiative transfer modeling are discussed in Sect. 6.3, but remain observationally poorly constrained and uncertain.

This situation is currently improving as new observing capabilities start to provide data that can potentially help to better constrain the dust temperatures. The *Herschel* Space Observatory with its imaging photometers that cover the wavelengths range from 70 to 500 μm (Pilbratt et al. 2010) provides for the first time the opportunity to fully sample the SED of the thermal dust emission from these cold objects[1] at a spatial resolution that is both appropriate to resolve these cores and comparable to that of the largest ground-based submm telescopes, which extend the wavelength coverage into the Rayleigh-Jeans regime of the SEDs.

To make use of *Herschel*'s new capabilities and improve our knowledge on the initial conditions of star formation by overcoming some of the above-mentioned limitations, we initiated the GTKP "The Earliest Phases of Star Formation" (EPoS). The main goal of our *Herschel* observations of low-mass pre- and protostellar cores in the framework of this project is to derive the spatial temperature and density structure of these cores with the aim of constraining protostellar collapse models. For this purpose, we selected 12 individual, isolated, nearby, and previously well-characterized molecular cloud cores and obtained spatially resolved FIR dust emission maps at five wavelengths around the expected peak of the emission spectrum. This paper gives an overview of the observations, data reduction, analysis methods, and initial results on the temperature and column density structure of the entire low-mass sample. Initial results on one of the sources (CB 244) were already published by Stutz et al. (2010). A first detailed follow-up study of another source from this sample (B 68) was published by Nielbock et al. (2012). Initial results on the high-mass cores observed in the framework of EPoS are published by Beuther et al. (2010, 2012), Henning et al. (2010), and Linz et al. (2010). An overview on the high-mass part of EPoS is given in Ragan et al. (2012).

This paper is organized as follows. Section 2 describes the target selection criteria and the sample of target sources. Section 3 describes the *Herschel* and complementary ground-based observations and the corresponding data reduction. In Sect. 4 we introduce our method of deriving dust temperature and column density maps from the data. Section 5 gives an overview of the initial results from the survey, and in Sect. 6 we discuss the uncertainties and limitations of our approach and compare our results to earlier work by other authors. Section 7 summarizes the paper.

2. Sources

Based on the results of earlier studies (e.g., Launhardt & Henning 1997; Launhardt et al. 1997; Henning & Launhardt 1998; Stutz et al. 2009a; Launhardt et al. 2010), we selected 12 well-isolated low-mass pre- and protostellar molecular cloud

cores in regions of exceptionally low cirrus confusion noise. The absolute background levels and the point source confusion noise (PSCN) were important selection criteria to obtain deep maps at 100 μm, which is essential for a precise estimate of the dust temperature. For this purpose, contributions from spatial fluctuations of the extragalactic background are derived from Negrello et al. (2004). Estimates of the Galactic cirrus confusion noise are based on the ISOPHOT confusion noise measurements, scaled down in the power spectrum to the resolution of *Herschel*/PACS (Kiss et al. 2005). The selected globules have typical 100 μm background levels of 1 mJy/$\square''$ or lower and PSCN $\leq$ 1 mJy/beam. For comparison, typical 100 μm background levels in the Taurus cloud are in the range 2−4 mJy/$\square''$, about 5 mJy/$\square''$ in Ophiuchus, and reach values of >100 mJy/$\square''$ in regions of high-mass star formation and infrared-dark clouds (IRDCs). This specific source selection strategy enabled us to obtain deeper 100 μm maps than most large-area surveys and to derive robust dust temperature estimates.

Our target list contains only established and previously well-characterized sources and does not cover regions with unknown source content. All sources are nearby (100–400 pc, with a mean distance of 240 ± 100 pc), have angular diameters of 3' to 6', linear sizes between 0.2 and 1.0 pc, and total gas masses of 1 to 25 $M_\odot$ (see Table 6). Coordinates, distances, spectral (evolutionary) classes, and references are listed in Table 1. Figure 1 shows the distribution of the target sources on the sky. Figure 2 illustrates that even those globules in our source list that are loosely associated with larger dark cloud complexes (like ρ Oph) are still isolated and located outside the regions of high extinction and source confusion.

Seven out of the 12 target globules were known to contain starless cores (Ward-Thompson et al. 1994). Of these, only CB 17 was already shown before to be prestellar[3] in nature (Pavlyuchenkov et al. 2006), while the star-forming potential of the other sources is not known. CB 17 contains, in addition to the prestellar core, a low-luminosity Class I young stellar object (YSO) at a projected separation of ∼25'' (∼6000 AU; Launhardt et al. 2010). CB 26 contains, in addition to the starless core (Stutz et al. 2009a), a well-studied Class I YSO at a projected separation of ∼3.6' (∼0.15 pc; Launhardt & Sargent 2001; Stecklum et al. 2004; Launhardt et al. 2009; Sauter et al. 2009). Five out of the 12 target globules were known to host Class 0 protostars. Of these, three cores contain additional sources with other evolutionary classifications. CB 130 contains an additional low-mass starless core as well as a Class I YSO. BHR 12 contains an additional Class I core at a projected separation of ∼20'' (∼8000 AU). CB 244 contains an additional starless core at a projected separation of ∼90'' (∼18 000 AU; Launhardt et al. 2010; Stutz et al. 2010). Two out of the 12 target globules (CB 6 and CB 230) are dominated by embedded Class I YSOs, i.e., the extended emission in them supposedly arises from remnant post-collapse envelopes. Of these, CB 230 is known to be a binary source with a projected separation of ∼10'' (∼4000 AU; Launhardt et al. 2010).

We also re-evaluated the distance estimates toward all globules, confirming the previously- used distances for 7 sources (e.g., Launhardt et al. 2010), and adjusting the distances for 5 sources. CB 4 and CB 6, which we earlier associated with the so-called "−12 km s^{-1}" H I clouds at 600–800 pc, are unlikely to be that far away, as suggested by the lack of foreground

---

[1] The peak of the flux density of a blackbody with T = 10−20 K is at $\lambda \approx 290-145$ μm. The peak of the energy density (νS_ν) of the optically thin globules at these temperatures is at only slightly shorter wavelengths (230−130 μm).

[2] http://lambda.gsfc.nasa.gov/product/cobe/dirbe_overview.cfm

[3] We use the term "prestellar" only for those starless cores that have been shown to be gravitationally unstable or on the verge of collapse.

Table 1. Source list.

Source	Other names	RA, Dec. (J2000) [h:m:s, °:′:″]	Region	Dist. [pc]	Ref.	Evol. class	Ref.
CB 4	...	00:39:03, +52:51:30	Cas A, GB	350 ± 150	18	starless	1
CB 6	LBN 613	00:49:29, +50:44:36	Cas A, GB	350 ± 150	18	Cl. I	2
CB 17	L 1389	04:04:38, +56:56:12	Perseus, GB	250 ± 50	2, 18	starless[a]	2
CB 26	L 1439	05:00:09, +52:04:54	Taurus-Auriga	140 ± 20	2, 11	starless[b]	2, 3, 4
CB 27	L 1512	05:04:09, +32:43:08	Taurus-Auriga	140 ± 20	1, 11	starless	1, 4
BHR 12	CG 30	08:09:33, −36:05:00	Gum nebula	400 ± 50	2, 10	Cl. 0[c]	2, 10
CB 68	L 146	16:57:16, −16:09:18	Ophiuchus	120 ± 20	2, 11	Cl. 0	2
B 68	L 57, CB 82	17:22:35, −23:49:30	Ophiuchus, Pipe nebula	135 ± 15	15, 16, 17	starless	5
CB 130	L 507	18:16:15, −02:32:48	Aquila rift, GB	250 ± 50	12, 14	Cl. 0[d]	2
B 335	CB 199	19:36:55, +07:34:24	Aquila, isolated	100 ± 20	8	Cl. 0	2, 7
CB 230	L 1177	21:17:39, +68:17:32	Cepheus flare, GB	400 ± 100	2, 13	Cl. I	2
CB 244	L 1262	23:25:47, +74:17:36	Cepheus flare, GB	200 ± 30	2, 13	Cl. 0[e]	2, 9

Notes. [a] CB 17: additional low-luminosity Class I YSO 25″ from starless core. [b] CB 26: additional Class I YSO 3.6′ south-west of the starless core. [c] BHR 12: additional Class I core ∼20″ south of Class 0 source. [d] CB 130: additional low-mass prestellar core ∼30″ west and Class I YSO ∼15″ east of Class 0 core. [e] CB 244: additional starless core ∼90″ west of Class 0 source.

References. (1) This paper; (2) Launhardt et al. (2010); (3) Launhardt & Sargent (2001); (4) Stutz et al. (2009a); (5) Alves et al. (2001); (7) Stutz et al. (2008); (8) Olofsson & Olofsson (2009); (9) Stutz et al. (2010); (10) Bourke et al. (1995); (11) Loinard et al. (2011); (12) Launhardt & Henning (1997); (13) Kun (1998); (14) Straižys et al. (2003); (15) de Geus et al. (1989); (16) Lombardi et al. (2006); (17) Alves & Franco (2007); (18) Perrot & Grenier (2003).
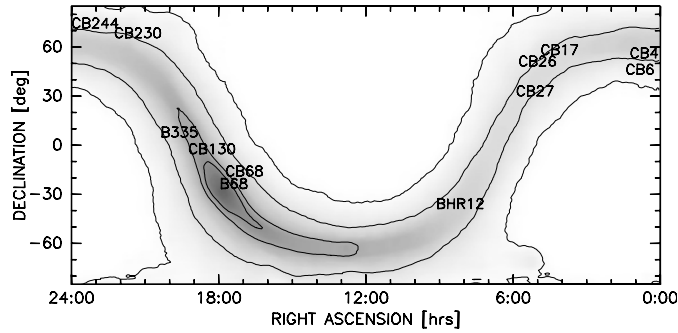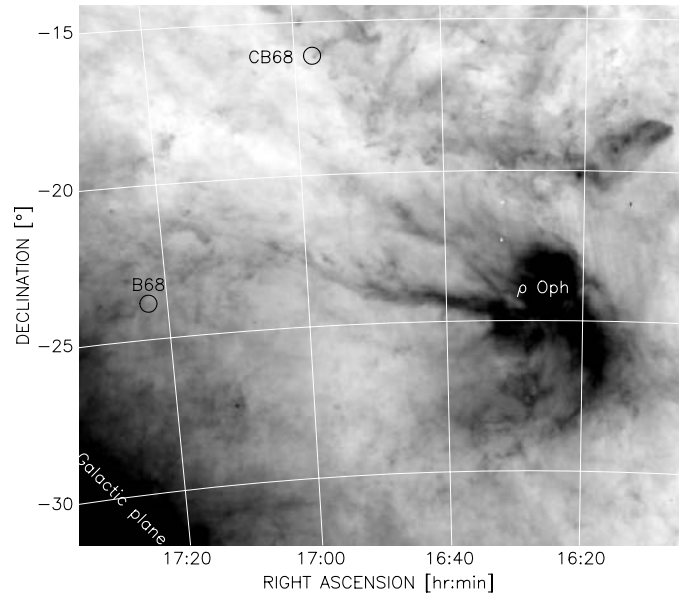

Fig. 1. All-sky map (gnomonic projection), showing the mean stellar K-band flux density distribution of the Milky Way (grayscale, derived from COBE-DIRBE NIR all-sky maps[3]) and the location of our target sources (see Table 1).

Fig. 2. IRAS 100 μm dust continuum emission map, showing the ρ Oph region and the location of two of our target sources (B 68 and CB 68). The plane of the Milky Way is visible at the lower left corner of the map. Compare to Figs. A.7 and C.7.

stars within a 3′ diameter area toward the cores. Despite their $v_{LSR} \sim -12$ km s^{-1}, they are more likely associated with the Cas A dark clouds in Gould's Belt at ∼350 pc (Perrot & Grenier 2003). CB 68 is associated with the ρ Oph dark clouds, for which we adopt the new precise trigonometric distance of 120 pc from Loinard et al. (2011). B 68 is located within the Pipe nebula and somewhat farther away from ρ Oph. Various direct and indirect estimates suggest a distance of 135 pc ± 15 pc (de Geus et al. 1989; Lombardi et al. 2006; Alves & Franco 2007). For CB 130, which is associated with the Aquila Rift clouds, we adopt the distance estimate of 250 pc ± 50 pc from Straižys et al. (2003).

3. Observations and data reduction

The *Herschel* FIR continuum data are complemented by submm dust continuum emission maps at 450 μm, 850 μm, and 1.2 mm, obtained with ground-based telescopes. Observations and reduction of both the *Herschel* and complementary ground-based data are described in the following two subsections. Representative general observing parameters are listed in Table 2, and the observations of individual sources are summarized in Table 3.

3.1. Herschel FIR observations

FIR continuum maps at five wavelength bands were obtained with two different instruments on board the *Herschel* Space observatory: PACS at 100 and 160 μm, and SPIRE at 250, 350, and 500 μm.

3.1.1. PACS data

All 12 sources were observed with the *Herschel* Photodetector Array Camera and Spectrometer (PACS; Poglitsch et al. 2010) in the scan map mode at 100 and 160 μm simultaneously. For each source, we obtained two scan directions oriented perpendicular to each other to eliminate striping in the final combined maps of effective size ∼10′ × 10′. The scan speed was set to

Table 2. General observing parameters.

λ_0 [μm]	Instr.	$\langle HPBW \rangle$ [arcsec]	$\langle$map size$\rangle$ [arcmin]	$\langle$rms$\rangle$ [mJy/beam]
100	PACS	7.1[a]	10	3
160	PACS	11.2[a]	10	13
250	SPIRE	18.2[a]	16–20	15
350	SPIRE	25.0[a]	16–20	17
450	SCUBA	8.5–9.5[b]	2	200
500	SPIRE	36.4[a]	16–20	14
850	SCUBA	14.4–15.1[b]	3	20
870	LABOCA	19.2[c]	40	8
1200	MAMBO-2	11	5–10	6

References. [a] Aniano et al. (2011); [b] Launhardt et al. (2010); [c] Nielbock et al. (2012) .

$20''$ s^{-1}, and a total of 30 repetitions were obtained in each scan direction, resulting in a total integration time of ~2.6 h per map. We emphasize that the accurate recovery of extended emission is the main driver for the following discussion and exploration of reduction schemes. The PACS data at 100 μm and 160 μm were processed in an identical fashion. They were reduced to level 1 using HIPE v. 6.0.1196 (Ott 2010), except for CB4 (processed with HIPE v. 6.0.2044), CB26 (processed with v. 6.0.2055), and CB6 (processed with v. 7.0.1931).

The rationale for using different versions of HIPE for different sources is that the latter three sources were observed much later (OD 660-770) than the other sources (OD 230-511) and the data were reduced with the respective latest HIPE version and calibration tree available at that time. Since processing of the PACS scanning data is very time-consuming, a re-reduction of all data with every new HIPE version with modifications relevant for our data is not feasible. Instead, we re-reduced the data for one source with the latest version of HIPE to verify how much the data reduction and post-processing modifications affect our results on the derived dust temperature and column density maps. Since this comparison, which is discussed in Sect. 6.1, shows that the effects are well within the range of the other uncertainties, we do not re-reduce all data, but incorporate these effects into our uncertainty assessment in Sect. 6.1.

Apart from the standard reduction steps, we applied *"2nd level deglitching"* to remove outliers in the time series data (*"time-ordered"* option) by applying a clipping algorithm (based on the median absolute deviation) to all flux measurements in the data stream that will ultimately contribute to the respective map pixel. For our data sets we applied an *"nsigma"* value of 20.

After producing level 1 data, we generated final level 2 maps using two different methods: high-pass filtering with photproject (within HIPE) and Scanamorphos (Roussel 2012), which does not use straightforward high-pass filtering, but instead applies its own heuristic algorithms to remove artifacts caused by detector flickering noise as well as spurious bolometer temperature drifts. Based on the high-pass median-window subtraction method, the photproject images turned out to suffer from more missing flux and striping than the Scanamorphos images. Because the correct recovery of extended emission is critical for accurate temperature mapping, high-pass filtering is clearly disadvantageous for our science goals. We also note that in a previous reduction, we found that the MADmap[4] processing of our brighter sources

(e.g., B 335) produces large artifacts[5] in the final maps due to the relatively bright central protostar; therefore we do not utilize this reduction scheme in this work.

For these reasons we decided to use Scanamorphos v. 9 as our standard level 2 data reduction algorithm. A comparison of final maps processed with different Scanamorphos v. 9 options showed that the *"galactic"* option recovered the highest levels of extended emission and was thus the best-suited for our data set and scientific goals. We use a uniform final map pixel scale of $1''6$ pix^{-1} at 100 μm and $3''2$ pix^{-1} at 160 μm for all objects. Furthermore, these data were processed including the non-zero-acceleration telescope turn-around data, with no additional deglitching (*"noglitch"* setting).

3.1.2. SPIRE data

All 12 sources were also observed with the Spectral and Photometric Imaging Receiver (SPIRE; Griffin et al. 2010) at 250, 350, and 500 μm. The scan maps of each source were obtained simultaneously at all three bands at the nominal scan speed of $30''$/s and over a $(16'-20')^2$ area, resulting in a total integration time of 10–16 mins per map. These data were processed up to level 1 with HIPE v. 5.0.1892 and calibration tree 5.1, which was the most up-to-date version at the time all data became available. In Sect. 6.1, we show that using the newest HIPE v. 9.1.0 only leads to nonsignificant minor changes in the SPIRE maps that are well below all other uncertainties. For this reason, we considered it unnecessary to re-reduce the data. Up to level 1 (i.e., the level where the pointed photometer timelines are derived), we performed the steps of the official pipeline (POF5_pipeline.py, dated 2.3.2010) provided by the SPIRE Instrument Control Center (ICC). The level 1 frames were then processed with the Scanamorphos software version 9 (Roussel 2012). All maps were reduced using the *"galactic"* option. The final map pixel sizes are 6, 10, and $14''$ at 250, 350, and 500 μm, respectively.

Photometric color corrections for both PACS and SPIRE data, that account for the difference in spectral slopes between flux calibration (flat spectrum) and actually observed source spectrum, are applied only in the subsequent data analysis and are described in Sect. 4.1.

3.2. (Sub)mm continuum observations

We also use complementary submm dust continuum emission maps at 450 μm, 850 μm, and 1.2 mm from ground-based telescopes for all 12 sources. Part of these complementary data we obtained and published in the past or retrieved from public archives. References to these data are given in Table 3.

Additional dedicated maps of the 1.2 mm dust emission from 6 sources were obtained with the 117-pixel MAMBO-2 bolometer array of the Max-Planck-Institut für Radioastronomie (Kreysa et al. 1999) at the IRAM 30 m-telescope on Pico Veleta (Spain) during two pool observing runs in October and November 2010. The mean frequency (assuming a flat-spectrum source) is 250 GHz ($\lambda_0 \sim 1.2$ mm) with a half power (HP) bandwidth of ~80 GHz. The HP beam width (HPBW) on sky is $11''$, and the field of view (FoV) of the array is $4'$ ($20''$ pixel spacing). Weather conditions were good, with zenith optical depths between 0.1 and 0.35 for most of the time and low sky noise. Pointing, focus, and zenith optical depth

---

[4] http://herschel.esac.esa.int/twiki/pub/Pacs/PacsMADmap/_UM_MADmapDOC.txt

[5] This problem has eventually been solved in the most recent MADmap implementation.

(by skydip) were measured before and after each map. The pointing stability was better than 3″ rms. Absolute flux calibration was obtained by observing Uranus several times during the observing runs and monitored by regularly observing several secondary calibrators. The flux calibration uncertainty is dominated by the uncertainty in the knowledge of the planet fluxes and is estimated to be ~20%. The sources were observed with the standard on-the-fly dual-beam technique, with the telescope scanning in azimuth direction at a speed of 8″/s while chopping with the secondary mirror along the scan direction at a rate of 2 Hz. Most sources were mapped twice, with different projected scanning directions (ideally orthogonal) and different chopper throws (46″ and 60″) to minimize scanning artifacts in the final maps. For one source (CB 27), we could obtain only one coverage. Effective map sizes (central pixel coverage) were adapted to the individual source sizes and were in the range 5′–10′, resulting in total mapping times per coverage of 40 min to 1.5 h.

The raw data were reduced using the standard pipeline "mapCSF" provided with the MOPSIC software[6]. Basic reduction steps include de-spiking from cosmic ray artifacts, correlated signal filtering to reduce the skynoise, baseline fitting and subtraction, restoring single-beam maps from the dual-beam scan data using a modified EKH algorithm (Emerson et al. 1979), and transformation and averaging of the individual horizontal maps into the equatorial system. Correlated skynoise correction was performed iteratively, starting with no source model in the first run. The resulting map is smoothed and the region with source flux is selected manually to represent the first source model, which is then iteratively improved in 20 successive correlated skynoise subtraction runs. Since our sources are faint, we follow the recommendation to apply this algorithm only up to level 1, except for the brightest source B335, where we go up to level 3. A third-order polynomial baseline fit to the time-ordered data stream and first-order fits to the individual scan legs are subtracted from the data, after masking out the region with source flux, to correct for slow atmospheric and instrumental drifts. Despite some unsolved electronic problems during these observing runs, which limited the efficiency of the correlated skynoise subtraction, the resulting noise levels in the final maps are ~6 mJy/beam, except for CB 27, where it is ~11 mJy/beam because only one coverage could be obtained.

The assumption of a flat-spectrum source in the definition of the nominal wavelength of the MAMBO detectors in combination with the broad bandpass made it necessary to apply a "color correction". In contrast to the *Herschel* FIR observations, (sub)mm wavelengths are sufficiently close to the Rayleigh-Jeans regime and the emission is optically thin for all our sources, such that the slope of the SED follows $S_\nu \propto \lambda^{-4}$ (for the dust opacity submm spectral index $\beta = 2$). Therefore, we follow Schnee et al. (2010) and correct the reference wavelength for all MAMBO data to 1100 μm. Color corrections for the SCUBA data are negligibly small (cf. Schnee et al. 2010) and are not applied.

We also verified the pointing in the final maps by comparing the emission peak positions with interferometric positions where available (CB 26, CB 68, CB 230, CB 244, B 335, BHR 12) and found that deviations are in all cases <2″, hence confirming the pointing stability and making additional pointing corrections unnecessary. The final maps of those sources for which we had both old and new 1.2 mm data (CB 6, CB 17, CB 26, and CB 230)

were generated by weighted averaging, after adapting beam sizes and correcting small pointing offsets.

Additional complementary NIR extinction maps as well as different molecular spectral line maps were also obtained with the aim of studying the relation between density, temperature, and dust properties on the one side, and gas phase abundances and chemistry on the other side. These latter data will be described and analyzed in forthcoming papers and are not presented here.

4. Modeling approach

4.1. Strategy and data preparation

The calibrated dust emission maps at the various wavelengths were used to compile spatially and spectrally resolved data cubes that cover the full extent of these relatively isolated sources on both sides of the peak of their thermal SEDs. Ideally, one would want to compare such data to synthetic maps from radiative transfer models convolved with the respective beams (forward-modeling, virtual observations) to constrain the physical properties of the sources. However, to avoid circular averaging with its well-known caveats, one would need 3D modeling to account for the complex structure present even in these relatively simple and isolated sources. Furthermore, not all of the observed features (like, e.g., the core-envelope temperature contrast, see Sects. 5.6 and 5.7) may be easily reproducible with existing self-consistent models, making the fully self-consistent forward-modeling approach very time-consuming. This will therefore be dealt with in forthcoming papers modeling individual cores.

For this survey overview paper, we take a simpler and more direct approach, giving up some of the spatial information in the short-wavelength maps and directly recovering and modeling beam and LoS optical-depth-averaged (hereafter LOS-averaged for short) SEDs, thus introducing as few as possible model-dependent assumptions into our analysis. For this purpose, the calibrated maps are prepared in the following way:

1. all maps are registered to a common coordinate system;
2. pointing corrections are applied where necessary (see below);
3. all maps are converted to the same physical surface brightness units (here Jy/□″) and extended emission calibration corrections are applied where necessary (see below);
4. background levels are determined and subtracted from the maps (see below), and finally;
5. all maps are convolved to the SPIRE 500 μm beam (*FWHM* 36″4).

PACS pointing corrections: since the *Herschel* spacecraft absolute 1σ pointing error was ~2″ and the PACS and SPIRE maps were not obtained simultaneously, random relative pointing errors between PACS and SPIRE maps can add up to ~3″–4″, which is about half the PACS 100 μm FWHM beam size (Aniano et al. 2011). This could severely hamper the usefulness of flux ratio (SED) maps, in particular around compact sources, if not corrected properly. For the long-wavelength SPIRE maps with beam sizes ~18″–36″ and no readily available astrometric reference, the pointing errors are fortunately negligible. For the PACS maps we utilize the fact that many 100 μm point sources are also detected in the *Spitzer* MIPS 24 μm images. We select in each field three stars detected in both the PACS 100 μm and MIPS 24 μm images to align the PACS astrometry in both the 100 μm and 160 μm images to the *Spitzer* images. The pointing

---

Table 3. Summary of FIR and submm observations.

Source	PACS Obs ID	SPIRE Obs ID	450 μm	850 μm	1.2 mm
CB 4	134221614(5, 6)	1342188689	–	–	M11
CB 6	134222272(3, 4)	1342189703	L10	L10	L10/M11
CB 17	134219100(8, 9)	1342190663	–	L10	L10/M11
CB 26	134221739(7, 8)	1342191184	L10[a]	L10[a]	L10/M11
CB 27	134219197(5, 6)	1342191182	DF08	DF08	M11
BHR 12	13421985(39, 40)	1342193794	L10	L10	L10
CB 68	134220428(6, 7)	1342192060	L10	L10	L10
B 68	134219305(5, 6)	1342191191	DF08	DF08/N12	B03
CB 130	134220598(2, 3)	1342191187	L10	L10	L10
B 335	134219603(0, 1)	1342192685	L10	L10	M11
CB 230	134218608(3, 4)	1342201447	L10	L10	L10/K08
CB 244	134218869(4, 5)	1342199366	L10	L10	L10

Notes. [a] The SCUBA maps of CB 26 cover only the western core with the embedded Class I YSO, but not the eastern starless core.

References. (L10) Launhardt et al. (2010); (M11) dedicated MAMBO-2 observations, described in this paper (see Sect. 3.2); (DF08) Di Francesco et al. (2008, SCUBA Legacy Catalogues); (B03) Bianchi et al. (2003, SEST-SIMBA observations); (N12) Nielbock et al. (2012, APEX-Laboca observations); (K08) Kauffmann et al. (2008, IRAM-MAMBO-2 observations).

corrections were found to be ≤3″ in all cases, i.e., small compared to the SPIRE 500 μm beam.

Surface brightness calibration corrections: since the PACS images are calibrated to Jy pix^{-1}, the conversion to Jy/□″ does not involve an assumption of the beam sizes. The SPIRE data, on the other hand, are calibrated to Jy beam^{-1}; to convert to surface brightness units we adopt the FWHM beam sizes from Aniano et al. (2011) listed in Table 2. The (sub)mm data have also been converted to Jy/□″ assuming the appropriate effective beam sizes for the respective observations (see references in Table 3). Since the standard calibration is done on point sources, but we are using the surface brightness to compile spatially resolved SEDs, we applied the recommended extended emission calibration corrections to the SPIRE data (see SPIRE Observer's Manual: HERSCHEL-DOC-0798, version 2.4, June 7, 2011).

PACS and SPIRE map background subtraction: the Scanamorphos *"galactic"* option preserves the large spatial frequency modes of the bolometer signal in the *Herschel* scan-maps. However, the absolute flux level of the background and spatial structures more extended than the scan-maps cannot be recovered since the exact level of the strong thermal background from the only passively cooled mirrors M1 and M2 of the observatory is unknown. Therefore, it is not clear how the extended, large-scale emission levels in the final *Herschel* maps are related to the absolute flux level of the background, which is composed of emission features larger than the map size, the general Galactic background ISRF, the cosmic microwave background (CMB), and other possible contributions, all varying differently with wavelength. Since uncertainties in additive flux contributions affect flux ratio measurements and the respective derivation of physical parameters from the SEDs, in particular at low flux levels, we subtract the background levels from all *Herschel* maps, thus making them consistent with the chopped (sub)mm data (although chopping is much more aggressive than the spatial filtering present in the *Herschel* maps). The consequences and uncertainties of this background removal on the data analysis are discussed in Sects. 4.2 and 6.1. We emphasize that this approach was feasible only because our sources were already initially selected to be relatively isolated on the sky (see Sect. 2).

To accomplish this re-zeroing, we adopt a method similar to that applied to *Spitzer* MIPS images in Stutz et al. (2009a). For each object we identify a 4′ × 4′ region in the PACS and SPIRE images that is relatively free from spatially varying emission and appears "dark" relative to the globule extended emission levels. We impose the additional requirement that this region is in or near a region in our complementary molecular line maps which is relatively free of ^{12}CO(2–1) emission. We always use the same region in all five *Herschel* scan-maps. For each band, we then calculate the representative flux level, f_{DC}, in the 4′ × 4′ region by implementing an iterative Gaussian fitting and σ-clipping scheme to the pixel value distribution at each wavelength. We do not consider pixels below 2σ from the mean and fit the main peak of the pixel value distribution. The f_{DC} value is then determined by iteratively fitting a Gaussian function to the histogram of pixel values, where at each iteration we include one more adjacent higher flux bin. The final adopted value of f_{DC} is defined as the mean value of the best-fit Gaussian that has the minimum σ value for all iterations. In this way we exclude pixels with higher flux which effectively broaden the distribution and would cause a bias in the f_{DC} calculation. The f_{DC} values are then subtracted from the corresponding *Herschel* maps at the respective wavelength (see Table 4 for the f_{DC} and σ values and coordinates of the reference region).

Image convolution: finally, all maps are convolved to the beam of the SPIRE 500 μm map, using the azimuthally averaged *Herschel* convolution kernels provided by Aniano et al. (2011). For the convolution of the (sub)mm maps, we use a Gaussian convolution kernel of width equal to the difference in quadrature between the effective FWHM of the (sub)mm observations and the SPIRE 500 μm FWHM of 36″.4.

After re-gridding to a common Nyquist-sampled pixel grid, we thus compile pixel-by-pixel SEDs for the wavelength range from 100 μm through 1.2 mm. Photometric color corrections for each pixel and each band are iteratively derived from the 100–160 μm and 250–500 μm spectral indices and polynomial fits to color correction factors provided for PACS in Table 2 of Müller et al. (2011) and in Table 5.3 of the SPIRE Observers Manual, and are applied in the subsequent SED modeling only.

The nominal point-source calibration uncertainty of the PACS photometers listed in the latest calibration notes is 3% at 100 μm and 5% at 160 μm. However, additional uncertainites that are hard to quantify are introduced by, e.g., the conversion to surface brightness units for extended emission, the beam convolution (imperfect kernels), and the color corrections. Likewise, the final recommended calibration uncertainty of 7% for SPIRE

Table 4. DC–flux levels in the *Herschel* data.

Source	RA, Dec[a] (J2000) [h:m:s, °:′:″]	f_{DC} (σ_f) 100 μm [μJy/□″]	f_{DC} (σ_f) 160 μm [μJy/□″]	f_{DC} (σ_f) 250 μm [μJy/□″]	f_{DC} (σ_f) 350 μm [μJy/□″]	f_{DC} (σ_f) 500 μm [μJy/□″]
CB 4	00:38:55, +52:56:06	8.4E2 (4.4E1)	5.9E2 (1.0E2)	2.8E2 (3.9E1)	1.4E2 (2.1E1)	6.9E1 (1.0E1)
CB 6	00:49:02, +50:42:34	1.1E3 (3.0E1)	4.6E2 (3.7E1)	1.8E2 (2.2E1)	8.7E1 (1.1E1)	3.8E1 (5.0E0)
CB 17	04:04:14, +56:53:07	1.3E3 (4.2E1)	7.5E2 (4.5E1)	2.6E2 (3.1E1)	1.3E2 (1.6E1)	6.5E1 (7.0E0)
CB 26	05:00:28, +52:00:36	7.8E2 (4.7E1)	7.7E2 (1.1E2)	1.4E2 (2.7E1)	6.8E1 (1.0E1)	3.3E1 (7.0E0)
CB 27	05:04:16, +32:38:19	1.0E3 (4.7E1)	6.7E2 (1.3E2)	1.9E2 (2.8E1)	9.4E1 (1.7E1)	5.0E1 (7.0E0)
BHR 12	08:09:10, −36:07:44	1.3E3 (5.7E1)	6.7E2 (8.5E1)	3.1E2 (2.9E1)	1.7E2 (1.3E1)	7.7E1 (5.0E0)
CB 68	16:57:07, −16:14:27	1.3E3 (5.4E1)	5.1E2 (6.9E1)	2.2E2 (3.5E1)	1.3E2 (2.0E1)	4.2E1 (1.1E2)
B 68	17:22:36, −23:44:11	9.1E2 (8.4E1)	8.9E2 (7.2E1)	1.2E2 (2.9E1)	5.9E1 (1.4E1)	1.3E1 (5.0E0)
CB 130	18:16:30, −02:29:23	1.4E3 (7.1E1)	8.0E2 (1.5E2)	3.0E2 (7.4E1)	1.6E2 (3.9E1)	7.7E1 (1.7E2)
B 335	19:36:48, +07:30:37	1.5E3 (4.3E1)	7.2E2 (7.9E1)	1.5E2 (2.1E1)	8.7E1 (9.0E0)	3.9E1 (6.0E0)
CB 230	21:17:00, +68:14:35	1.3E3 (4.8E1)	5.1E2 (1.8E2)	1.8E2 (4.3E1)	1.4E2 (7.1E1)	7.4E1 (2.8E1)
CB 244	23:24:55, +74:23:01	1.3E3 (4.0E1)	5.1E2 (7.5E1)	3.0E2 (2.7E1)	1.7E2 (1.3E1)	7.7E1 (7.0E0)

Notes. [a] Center of the DC reference field (see Sect. 4.1).

does not account for some of the uncertainties introduced in the post-processing. Recent systematic comparisons between the *Herschel* and *Spitzer* surface brightness calibrations showed that they agree to within about 10%, with intrinsic uncertainties on both sides[7]. Therefore, we adopt for all *Herschel* data the conservative value of 15% for the relative calibration uncertainty in the final maps. This number is used for calculating the weights of the individual data points and with respect to the ground-based data in the subsequent fitting procedure (Sect. 4.2).

4.2. Deriving dust temperature and column density maps

The subtraction (or chopping out) of a flat background level from the emission maps implies that the remaining emission in the map at each image pixel is given by

$$S_\nu(\nu) = \Omega \left(1 - e^{-\tau(\nu)}\right) \left(B_\nu(\nu, T_d) - I_{bg}(\nu)\right) \quad (1)$$

with

$$\tau(\nu) = N_H \, m_H \, \frac{M_d}{M_H} \, \kappa_d(\nu) \quad (2)$$

where $S_\nu(\nu)$ is the observed flux density at frequency ν, Ω the solid angle from which the flux arises (here normalized to 1 arcsec^2), $\tau(\nu)$ the optical depth through the cloud, $B_\nu(\nu, T_d)$ the Planck function, T_d the dust temperature, $I_{bg}(\nu)$ the background flux level, $N_H = 2 \times N(H_2) + N(H)$ the total hydrogen column density, m_H the proton mass, M_d/M_H the dust-to-hydrogen mass ratio, and $\kappa_d(\nu)$ the dust mass absorption coefficient. T_d and κ_d may vary along the LoS, in which case Eq. (1) has to be written in differential form and integrated along the LoS. However, for this overview paper we assume both parameters to be constant along the LoS and discuss the uncertainties and limitations of this approach in Sect. 6.2.

For $\kappa_d(\nu)$, we assume for all sources in this paper the tabulated values listed by Ossenkopf & Henning (1994) for mildly coagulated (10^5 yrs coagulation time at gas density 10^6 cm^{-3}) composite dust grains with thin ice mantles (Col. 5 in their Table 1, usually called "OH5"), logarithmically interpolated to the respective wavelength where necessary. For the hydrogen-to-dust mass ratio in the Solar neighborhood, we adopt

$M_H/M_d = 110$ (e.g., Sodroski et al. 1997). Note that the total gas-to-dust mass ratio, accounting for helium and heavy elements, is about 1.36 times higher, i.e., $M_g/M_d \approx 150$.

The exact background flux levels at the location of the individual clouds, $I_{bg}(\nu)$, are a priori unknown as explained in Sect. 4.1. At the frequencies relevant for this paper, this background radiation is composed mainly of the cmB, the extragalactic cosmic infrared background (CIB), and the diffuse Galactic background (DGB). While the first contribution (CMB) is well-known and dominates at wavelength >500 μm, the mean levels of the CIB have been compiled by, e.g., Hauser & Dwek (2001) from flux measurements in the "Lockman Hole" by various space observatories (e.g., COBE and ISO) and ground-based (sub)mm instruments (e.g., SCUBA). However, at wavelengths <350 μm, the DGB, which strongly varies with position, dominates over cmB and CIB. Here we follow the approach of Stutz et al. (2010) and use the Schlegel et al. (1998) 100 μm IRAS maps and the ISO Serendipity Survey observations at 170 μm to extrapolate approximate mean flux levels at the typical Galactic locations of our sources. Since the uncertainty in the resulting temperature and column density estimates introduced by the uncertainty in the exact knowledge of the I_{bg} levels is negligible, as discussed quantitatively in Sect. 6.1, we do not attempt to derive the local values of the DGB for each source separately. Instead, we adopt the following mean values for all sources: 0.3, 0.8, 0.5, 0.3, 0.2, 2.9, and 6.5 mJy/arcsec^2 at λ 100, 160, 250, 350, 500, 850, and 1100 μm, respectively.

From the calibrated and background-subtracted dust emission maps, we extract for each image pixel the SED with up to 8 data points between 100 μm and 1.2 mm. These individual SEDs are independently fit (χ^2 minimization) with a single-temperature modified blackbody of the form of Eqs. (1) and (2) with T_d and N_H being the free parameters. The individual flux data points are weighted with σ^{-2}, where σ is the quadratic sum of flux times the relative calibration uncertainty (see Sect. 4.1) and the mean rms noise in the respective map measured in regions of zero or lowest emission outside the sources (see Table 4). In order to minimize the effect of $T - N_H$ degeneracies in the fitting, because at the low temperatures in these cores, $T \leq 10$ K, even the 1.2 mm emission does not represent the Rayleigh-Jeans regime where the SED slope is independent of T, the weight of data points with $S_\nu < \sigma$ was set to zero, i.e., these points were not considered in the fitting. To further avoid erroneous extrapolations of the SED fit to unconstrained shorter

---

[7] See PICC-NHSC-TR-034 and PICC-NHSC-TN-029 under https://nhscsci.ipac.caltech.edu/

wavelengths, only pixels with valid fluxes in all 5 *Herschel* bands were considered. This latter criterion was usually constrained by the PACS 100 μm maps. The best-fitting parameters were derived by employing a least squares fit to all flux values between 100 μm and 1.2 mm at a given image pixel, using a "robust" combination of the classical simplex amoeba search and a modified Levenberg Marquardt method with adaptive steps, as implemented in the *"mfit"* tool of GILDAS[8].

This procedure yields LoS-averaged dust temperature and column density maps of the sources, which are presented in Sect. 5.2. The temperature maps provide a robust estimate of the actual dust temperature of the envelope in the projected outer regions, where the emission is optically thin at all wavelengths and LoS temperature gradients are negligible. Toward the source centers, where cooling and shielding or embedded heating sources can produce significant LoS temperature gradients and the observed SEDs are therefore broader than single-temperature SEDs, the central dust temperatures will be overestimated (in the case of a positive gradient in cold sources) or underestimated (negative gradient in internally heated sources). For these reasons, the column density maps are corrupted and exhibit artifacts in regions of $\sim 20''$–$40''$ radius around the warm protostars (see, e.g., Figs. B.7 or B.6). These caveats are discussed and quantified in Sect. 6.2, including some already worked-on solutions.

5. Results

5.1. Herschel FIR maps

The resulting calibrated dust emission maps at $\lambda 100$, 160, 250, 350, and 500 μm and at original angular resolution are presented in Figs. A.1 through A.12. The *Herschel* maps are accompanied by optical (red) images from the second Digitized Sky Survey (DSS2[9]), which were obtained through the *SkyView*[10] interface. These optical images clearly show the regions of highest extinction as well as, in several cases, extended cloudshine structures. All maps are overlaid with contours of the (sub)mm dust continuum emission observed with ground-based telescopes.

The 160 through 500 μm maps are usually very similar to each other in appearance, outlining the thermal dust emission from the dense cores along with the often filamentary or tail-like, more tenuous envelopes. Except for some filamentary or tail-like extensions like, e.g., in CB 17 (Fig. A.3), the $\sim 18'$ SPIRE maps usually cover the entire extent of the detectable FIR dust emission down to the more or less flat background levels. The slightly smaller PACS maps ($\sim 10'$) also usually cover the entire extent of the clouds, but in some cases cut off a bit more of some filamentary or tail-like extensions (e.g., Fig. A.3).

The PACS 100 μm maps often show significantly fainter or less extended emission than the maps at longer wavelengths, owing to the fact that 100 μm samples the steep short-wavelength side of the SED at the low temperature of the dust in these clouds
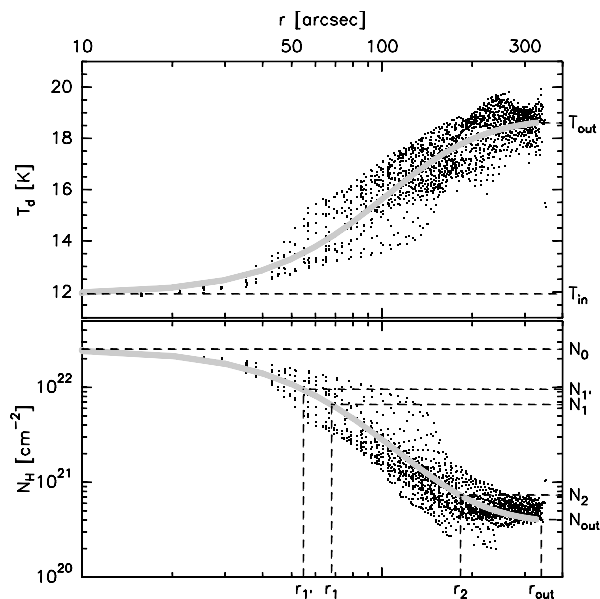
Fig. 3. Radial profiles of column density and LoS-averaged dust temperature of B 68 (cf. Fig. 9 of Nielbock et al. 2012 for the ray-tracing results of the same data). Small black dots show the data pixel values over radial distance from the column density peak (see Fig. B.8). Solid gray lines show best fits to these data with Eqs. (3) and (8) and the parameters listed in Table 5. The parameters are also labeled on the diagram axes to illustrate their meaning, with the following characteristic radii: r_1 = flat core profile radius (Eq. (3)), $r_{1'}$ = radius to define consistent dense core boundary (Eqs. (10) and (11)), r_2 = cloud radius at transition to halo (Eq. (6)), and r_{out} = outer cloud boundary (Eq. (3)).

(Fig. 4). In some cases, the diffuse 100 μm emission even exhibits a "hole" or "shadow" at the location of the column density peak (e.g., CB 27; Fig. A.5), hinting at extremely cold and dense (high column density) cores with thin warmer envelopes, which are thus good candidates of cores on the verge of protostellar collapse (see Stutz et al. 2009a, for a discussion of 24 μm and 70 μm shadows in dense cores).

On the other hand, the 100 μm maps, which also have the highest angular resolution ($\approx 7''$) of all our *Herschel* maps, are most sensitive to embedded heating sources like, e.g., protostars. Although even the previously known very low-luminosity object (VeLLO) in CB 130 (Kim et al. 2011; see also Dunham et al. 2008) is well-detected (Fig. A.9), our maps do not reveal any obvious previously unknown warm compact source in any of the globules, confirming that all our presumably starless cores are indeed starless. The only possible exception might be CB 17 (see Fig. A.3), where we find hints of an extremely low-luminosity ($L_{bol} < 0.04 \, L_\odot$) cold embedded source very close (in projection) to CB17 - IRS (Chen et al. 2012; Schmalzl et al., in prep.).

5.2. Dust temperature and column density maps and radial profiles

The LoS-averaged dust temperature and hydrogen column density maps derived with the fitting procedure described in Sect. 4.2 are presented in Figs. B.1 through B.12. All sources show systematic dust temperature gradients with cold interiors (11–14 K) and significantly warmer outer rims (14–20 K). Embedded heating sources like protostars, including the VeLLO in CB 130 (Fig. B.9; Kim et al. 2011), show up very clearly in the temperature maps.

To characterize the column density profiles quantitatively, we fit circular profiles around the column density peak to the

Table 5. Column density and dust temperature profiles.

Source[a]	N_0[b] [cm^{-2}]	N_{out}[b] [cm^{-2}]	r_1[b] [AU]	r_2[b] [AU]	r_{out}[b] [AU]	p[b]	T_{in}[b] [K]	T_{peak}[c] [K]	T_{out}[b] [K]
CB 4	7.5E21	6.0E19	2.5E4	6.2E4	9.5E4	5.0	14.0	–	19.5
CB 17 - SMM	2.5E22	1.0E21	1.0E4	3.1E4	3.5E4	3.0	11.7	–	13.1
CB 26 - SMM2	1.4E22	1.2E21	8.4E3	2.2E4	3.4E4	2.4	12.8	–	14.0
CB 27	1.9E22	2.1E21	1.6E4	2.1E4	2.8E4	4.0	11.9	–	14.2
B 68	2.5E22	4.0E20	1.0E4	2.1E4	4.6E4	5.0	11.9	–	18.5
CB 244 - SMM2	4.6E22	1.1E21	7.0E3	6.0E4	9.0E4	1.8	11.3	–	14.5
CB 130 - SMM[d]	2.6E22	2.0E21	7.2E3	2.8E4	4.7E4	1.8	12.1	–	13.5
CB 6[e,f]	5.0E21	5.0E20	...	...	1.4E5	...	14.5	18.4	15.7
CB 26 - SMM1[e]	1.0E22	9.0E20	...	...	...	...	...	19.0	14.6
BHR 12[f]	5.4E22	1.0E21	1.4E4	3.5E4	1.1E5	4.0	14.8	18.5	17.3
CB 68	2.4E22	5.0E20	1.1E4	2.7E4	2.9E4	4.0	12.7	19.0	16.5
B 335	3.1E22	6.2E20	3.6E3	1.8E4	3.8E4	2.3	14.7	18.8	16.2
CB 230 - SMM[e,f]	2.7E22	5.0E20	...	...	1.4E5	...	14.5	19.6	15.6
CB 244 - SMM1	1.5E22	1.0E21	1.2E4	5.5E4	9.0E4	1.7	11.5	19.6	14.2
starless cores	2.3 ± 1.0E22	1.1 ± 0.6E21	1.2 ± 0.6E4	3.5 ± 1.6E4	5 ± 2E4	3.3 ± 1.2	12.2 ± 0.8	...	15.3 ± 2.2
protostellar cores	2.4 ± 1.4E22	0.7 ± 0.2E21	0.9 ± 0.5E4	3.4 ± 1.2E4	9 ± 4E4	3.0 ± 0.9	13.6 ± 1.2	19.0 ± 0.4	15.7 ± 0.9
all	2.3 ± 1.3E22	0.9 ± 0.5E21	1.1 ± 0.5E4	3.5 ± 1.5E4	7 ± 4E4	3.2 ± 1.2	13.0 ± 1.2	...	15.5 ± 1.8

Notes. In contrast to the other tables, sources in this table have been grouped into starless and protostellar. [a] Coordinates are listed in Table 6. [b] Derived from circular fits to the dust temperature and column density maps; see Sect. 5.2, Eqs. (3) through (9). [c] Peak temperature at the position of the embedded heatig source (protostar), severely underestimates the true central dust temperature because of beam smoothing and LoS averaging. [d] CB 130: the embeded VeLLO causes only a very small temperature increase in the smoothed dust temperature map. [e] Bad fit due to large unresolved LoS gradients, no meaningful values for some of the parameters. [f] The embedded double sources in BHR 12 and CB 230 are not resolved in the smoothed dust temperature maps.

maps, using a "Plummer-like" profile (Plummer 1911; see also Whitworth & Ward-Thompson 2001), modified by a constant term to account for the observed outer column density "plateau" (see discussion in Sect. 5.7):

$$N_{\mathrm{H}}(r) = \begin{cases} \dfrac{\Delta N}{\left(1+(r/r_1)^2\right)^{p/2}} + N_{out} & \text{if } r \le r_{out} \\ 0 & \text{if } r > r_{out}. \end{cases} \tag{3}$$

The peak column density is then

$$N_0 = N_{\mathrm{H}}(r = 0) = \Delta N + N_{out}. \tag{4}$$

This profile accounts for an inner flat (column) density core at $r < r_1$ where

$$N_1 = N_{\mathrm{H}}(r_1) = \frac{\Delta N}{2^{p/2}} + N_{out}, \tag{5}$$

approaches a power-law with index p at $r \gg r_1$, turns over into a flat outer column density "plateau" outside

$$r_2 = r_1 \sqrt{\left(\frac{\Delta N}{N_{out}}\right)^{2/p} - 1} \tag{6}$$

where

$$N_2 = N_{\mathrm{H}}(r_2) = 2 \times N_{out}, \tag{7}$$

and is cut off at r_{out}. This outer boundary of the thin envelope or halo is not well-recovered in most cases because filamentary extensions emphasize deviations from circular/spherical geometry with increasing distance from the core center and the flux levels gradually decline below the noise cut-off (see Sect. 4.2). For the same reason, the flatness of the outer column density profile at level N_{out} might be partially an artifact of circularly averaging noncircular structure at a level just above the noise.

To empirically fit and parameterize the radial temperature profiles of purely externally heated cores, we use a similar profile of the form:

$$T(r) = T_{out} - \frac{\Delta T}{\left(1+\left(\frac{r}{r_{\mathrm{T}}}\right)^2\right)^{q/2}}. \tag{8}$$

The central temperature minimum is then given by

$$T_{in} = T_{out} - \Delta T. \tag{9}$$

Before fitting radial profiles to the maps, we mask some of the spurious low-SNR edge features and tail-like (asymmetric) extensions, always applying the same spatial mask in both the column density and dust temperature maps. For cores with embedded heating sources (protostars), we also mask the region with local temperature increase before fitting the radial profiles with Eqs. (3) and (8) and also list in Table 5 the value of the central temperature maximum T_{peak}. The radius of the masked region varied between 20″ and 40″. This extrapolation for N_0 and T_{in} of the outer profile into the core center, where both the local temperature and the column density estimates are very uncertain due to large and unresolved LoS temperature gradients, leads to an increased uncertainty in particular of the value for N_0 in the protostellar cores. This and other shortcomings of this model and the interpretation of its parameters are discussed in Sect. 6.2.

To illustrate the quality of these radial profile fits and the meaning of the various parameters, we show in Fig. 3 the radial distribution of N_{H} and T_{d} values in the resulting maps for B 68 along with the best-fit profiles and the parameters labeled on the diagram axes. The best-fit parameter values for N_0, N_{out}, r_1, r_2, r_{out}, p, T_{in}, T_{peak} (for cores with embedded heating sources), and T_{out} of all sources are listed in Table 5. We do not list parameters r_{T} and q, but note that from the core centers outward, the LoS-averaged dust temperature typically raises by 1 K at a radius of $(1 \pm 0.3) \times 10^4$ AU.

Note that in the next section, we define core and cloud sizes via the mean extent of certain column density contours in the maps, and not via the radial profile fit parameters r_1 and r_{out}. In particular for very elliptical sources and sources with extended halos, the derived mean diameters are therefore not necessarily identical to twice the corresponding radial profile-fit radii.

5.3. Source morphologies, integral properties, and SEDs

In addition to the pixel-by-pixel SEDs and the column density and dust temperature maps, we also derive integrated source properties using certain column density levels to define the integration areas. Total cloud sizes are derived by measuring the major and minor extent of the N_{out} contour in the column density maps, which is marked as the outer yellow contour in Figs. B.1 through B.12. The resulting linear diameters (invoking the distances listed in Table 1) are listed in Table 6. The mean radii of the globules in our sample range from 0.1 pc (CB 130) to 0.5 pc (CB 230), with a mean of 0.22 ± 0.1 pc ($4.8 \pm 2.2 \times 10^4$ AU), which is about twice the typical Jeans lengths of these clouds (≈ 0.13 pc, assuming the mean radius and mass and a mean temperature of 13 K; see also stability discussion in Sect. 5.5). The mean projected aspect ratio of the clouds is 0.66 ± 0.16, with the most extreme cases CB 6 and BHR 12 (0.4) and B 335 (0.98). These measures do not account for the long tails, e.g., in CB 17 or CB 68, nor do they accurately reflect the actual aspect ratios of the individual sources, since the 3D projection of the elliptical clouds onto the plane of sky remains unknown. Note that these and the following uncertainty values only represent the variance of the mean and do not include systematic uncertainties, which are discussed in Sect. 6.

Since cometary tails in globules appear to be fairly ubiquitous (see Table 6 and Sect. 5.8), we have also assessed the possibility that some of the apparently tail-less globules (e.g., B 335 or CB 130) could also have a tail pointing at us or away from us. However, given the length of the tails observed, e.g., in CB 6 (Fig. C.2), CB 17 (Fig. C.3), or CB 68 (Fig. C.7), it is extremely unlikely that a globule like B 335 has a tail that is directly aligned with the line of sight. Another argument against this possibility comes from the fact that, at least in the starless cores, the (LoS-averaged) temperature minimum always agrees with the column density maximum. Should a long tail, like the one seen in e.g., CB 17, be oriented along the line of sight, then its total column density would sum up to a value similar to or even higher than the actually observed ones. However, since the tails are not as well-shielded from the IRSF as spherical cores and therefore have approximately the same average temperature as the envelopes, such a projection could not result in a clear temperature minimum at the position of the column density maximum, as observed in all starless cores.

Total hydrogen masses are derived by integrating the column density maps within the N_{out} contour and are also listed in Table 6. These masses range from 0.8 $M_\odot$ (B 335) to 18 $M_\odot$ (CB 230), with a mean value of $\langle M_{cloud} \rangle = 5.4 \pm 5.0$ $M_\odot$. Using the somewhat more conservative column density threshold N_2 (Eq. (7)) would have the benefit of being less susceptible to inhomogeneities of the background level and having closed contours in all sources, but would cut off some of the extended emission that most likely originates from the globule. Using N_2 instead of N_{out} would lead to ≈ 10–15% lower masses and smaller sizes for the globules compared to the values listed in Table 6.

Integral cloud SEDs (not shown) are obtained by integrating the various emission maps within the N_{out} contour. Where available and appropriate, we also include ground-based optical

and NIR data, *Spitzer* IRAC and MIPS maps, as well as ISO and IRAS fluxes (see Launhardt et al. 2010). We then fit the resulting SEDs between $\lambda\,100\,\mu$m and 1.2 mm in the same way as the individual image pixel SEDs (Sect. 4.2). To facilitate integration of the SEDs at wavelengths shortward of the SED peak, fluxes at $\lambda \leq 100\,\mu$m are logarithmically interpolated as described in Launhardt et al. (2010). Bolometric luminosities (L_{bol}) are derived by integrating the SEDs over the complete wavelength range. Submillimeter luminosities (L_{smm}) are derived by integrating the SEDs at wavelengths longward of 350 μm. The resulting total cloud luminosities range from 1.3 $L_\odot$ (CB 17, B 68, B 335) to 29 $L_\odot$ (BHR 12), with a mean of $\langle L_{cloud} \rangle \sim 6.7$ $L_\odot$. See Table 6 and Fig. 7 for the distribution of masses and luminosities.

In four out of the twelve globules, the *Herschel* and submm maps reveal multiple cores (CB 26, BHR 12, CB 130, CB 244 - all known before to be multiple), while the other eight globules appear single-cored at the *Herschel* resolution. In the temperature and column density maps, the double cores are only resolved clearly in CB 26 and CB 244.

The identification of a common criterion for characterizing the extent and measuring masses and luminosities of the dense cores was less straight-forward. Since the (column) density profile of a single-cored globule continuously decreases from the center toward the outer boundary of the globule, there is no simple way to observationally distinguish between a "core" and an "envelope", like in larger molecular clouds where the outer boundary of a core is usually judged to be where the (column) density profile merges with the surrounding cloud level. The flat core radius, r_1, of the column density profile is also not a good criterion since its value depends on the derived power-law index p (Eq. (3)), which is not well-constrained in most cases since $r_2 \gg r_1$, i.e., the range where the column density profile approaches a power-law and p can be derived is too small in many cases. Therefore, we define an empirical, but well-reproducible column density threshold for all dense cores by

$$N_{1'} = N_H(r_{1'}) = \frac{\Delta N}{e} + N_{out}, \tag{10}$$

where e is Euler's number and

$$r_{1'} = r_1 \sqrt{e^{2/p} - 1}. \tag{11}$$

For $p = 2/\ln(2)$ ($\sim$2.9, which is actually very close to the mean $\langle p \rangle$ of our sample), we obtain $N_{1'} = N_1$ and $r_{1'} = r_1$ (Eq. (5)). This column density threshold is high enough to permit a reasonable separation of the subcores in CB 26 (Fig. B.4) and CB 244 (Fig. B.12), while at the same time being low enough to fully include the regions of corrupted column density values around embedded protostars (due to strong unresolved LoS temperature gradients; cf. Sect. 4.2). Note that this is an observationally driven definition of "core" that is not based on a well-characterized physical transition between core and envelope (see also discussion in Sect. 5.4). In a few cases, we had to use ellipses to define the core areas, which were however guided by the $N_{1'}$ contour. In CB 26 (Fig. B.4), the $N_{1'}$ contour still includes a bridge between cores SMM1 and SMM2, such that an artifical cut-off by an ellipse was necessary. In addition, the corruption of the column density map around SMM1 by unresolved LoS temperature gradients leads to an offset between the column density peak (artifact) and the temperature peak (actual location of the embedded YSO). This latter effect required to also use ellipses for CB 244-SMM1 (Fig. B.12) and BHR 12 (Fig. B.6).

The resulting integral SEDs of the core regions enclosed by the $N_{1'}$ contours or the respective ellipses (where marked in

Table 6. Physical parameters of globules and embedded cores.

Source	RA, Dec. (J2000)[a] [h:m:s, °:′:″]	Size[b] [AU]	b:a[b]	$M_{\rm H}$[c] [$M_\odot$]	$L_{\rm bol}$[c] [$L_\odot$]	$T_{\rm bol}$[c] [K]	$\frac{L_{\rm smm}}{L_{\rm bol}}$[c] [%]	Morphology[d] evol. class	Figures
CB 4	...	1.2E5	0.74	1.6	2.8	...	...	R, T(0.5)	A.1, C.1, B.1
CB 4 - SMM	00:39:05.2, +52:51:47	5.2E4	0.62	0.7	0.77	23	11.7	starless, unbound	...
CB 6	...	1.2E5	0.40	5.9	3.5	...	...	C, T(2.6)	A.2, C.2, B.2
CB 6 - SMM	00:49:24.3, +50:44:36	3.9E4	1.0	1.0	2.5	158	5.1	Cl. I	...
CB 17	...	8.6E4	0.67	3.0	1.3	...	...	C, T(>1.0)	A.3, C.3, B.3
CB 17 - SMM	04:04:37.7, +56:55:59	2.1E4	0.86	1.0	0.37	18	22.3	starless, stable	...
CB 17 - IRS	04:04:34.0, +56:56:16	...	...	...	0.12	80	2.2	Cl. I[e]	...
CB 26	...	7.3E4	0.75	2.4	1.9	...	...	C, M, T(0.6)	A.4, C.4, B.4
CB 26 - SMM1	04:59:49.3, +52:04:39	2.0E4[f]	1.0[f]	0.3[f]	0.47[f]	81[f]	6.5[f]	Cl. I	
CB 26 - SMM2	05:00:14.5, +52:05:59	2.2E4[f]	1.0[f]	0.6[f]	0.30[f]	20[f]	17.3[f]	starless, stable	
CB 27	...	6.7E4	0.77	3.7	2.2	...	...	C, T(0.3)	A.5, C.5, B.5
CB 27 - SMM	05:04:08.1, +32:43:30	2.6E4	0.61	1.2	0.44	18	20.5	starless, stable	...
BHR 12	...	1.2E5	0.39	11	29	...	...	C, M, T(0.9)	A.6, C.6, B.6
BHR 12 - SMM	08:09:32.7, −36:05:19	3.1E4[g]	0.82[g]	3.7[g]	14.9[g]	104[g]	3.2[g]	Cl. 0/I[h]	...
CB 68	...	6.5E4	0.55	2.1	2.1	...	...	C, T(0.7)	A.7, C.7, B.7
CB 68 - SMM	16:57:19.7, −16:09:23	1.5E4	0.79	0.5	0.86	41	6.3	Cl. 0	...
B 68	...	5.6E4	0.83	1.3	1.3	...	...	C	A.8, C.8, B.8
B 68 - SMM	17:22:38.3, −23:49:51	1.6E4	0.88	0.6	0.23	19	17.4	starless, stable	...
CB 130	...	4.9E4	0.52	2.7	1.6	...	...	M	A.9, C.9, B.9
CB 130 - SMM	18:16:15.6, −02:32:45	2.0E4	0.63	1.0	0.37	38	20.8	VeLLO[i]	...
B 335	...	4.8E4	0.98	0.8	1.3	...	...	R	A.10, C.10, B.10
B 335 - SMM	19:37:00.7, +07:34:08	8.5E3	0.80	0.2	0.57	37	4.4	Cl. 0	...
CB 230	...	2.1E5	0.69	18	25	...	...	C	A.11, C.11, B.11
CB 230 - SMM	21:17:39.9, +68:17:36	3.5E4	0.55	3.0	10.4	189	3.7	Cl. I[k]	...
CB 244	...	1.4E5	0.61	12	8.2	...	...	M	A.12, C.12, B.12
CB 244 - SMM1	23:25:47.3, +74:17:44	2.0E4[l]	0.87[l]	0.8[l]	1.82[l]	56[l]	4.3[l]	Cl. 0	
CB 244 - SMM2	23:25:26.8, +74:18:22	2.3E4	0.87	2.1	0.53	17	24.2	prestellar	...

Notes. [a] Coordinates of column density peak (starless cores) or dust temperature peak (embedded source). [b] Mean diameter ($\sqrt{a \times b}$) and aspect ratio of the $N_{\rm out}$ column density contour listed in Table 5 for the globules (i.e., $\approx 2 \times r_{\rm out}$, Eq. (3) and Fig. 3), and of the $N_{1'}$ contour (Eq. (10)) for the embedded cores (i.e., $2 \times r_{1'}$, Eq. (11)). [c] Measured inside the $N_{\rm out}$ contour (globules) or the $N_{1'}$ contour (cores), except where marked otherwise. [d] Morphology description based on visual inspection of DSS2-red optical images and *Herschel* dust emission maps: R: round or slightly elliptical; C: cometary-shaped; M: multiple cores; T(x): tail of length x pc. [e] CB 17 - IRS is identified in the PACS 100 μm map and as a local temperature maximum in the T-map, but cannot be separated from SMM in the column density map. [f] CB 26 - SMM1 and SMM2: ellipses, marked by dotted lines in Fig. B.4, were used instead of the $N_{1'}$ contour (cf. Sect. 5.3). [g] BHR 12: An ellipse, marked by dotted lines in Fig. B.6, was used instead of the $N_{1'}$ contour (cf. Sect. 5.3). [h] BHR 12: The two embedded sources SMM1 (Class I) and SMM2 (Class 0; sep. 21″; see Launhardt et al. 2010) are not resolved here. [i] CB 130: additional low-mass prestellar core ∼30″ west and Class I YSO ∼15″ east of Class 0 core. [k] CB 230: the two embedded sources IRS1 and IRS2 (sep. 10″; see Launhardt et al. 2010) are not resolved here. [l] CB 244 - SMM1: an ellipse, marked by dotted lines in Fig. B.12, was used instead of the $N_{1'}$ contour (cf. Sect. 5.3).

Figs. B.1 through B.12) are shown in Fig. 4. These SEDs were derived in the same way as described above for the integral cloud SEDs. The integral properties derived from these subregions are much more representative of the cold starless cores or warm protostellar cores than the total globule quantities which include the extended envelopes that are dominated by external heating from the ISRF. Resulting sizes, aspect ratios, masses, and bolometric luminosities of the cores are listed in Table 6. The relation between SEDs and evolutionary stages is discussed in Sect. 5.4.

The mean core diameters, as defined by the $N_{1'}$ contour and listed in Table 6, range from 8.5×10^3 AU (0.04 pc; B 335) to 5.2×10^4 AU (0.25 pc; CB 4), with a mean of $(2.5 \pm 1) \times 10^4$ AU (0.12 ± 0.05 pc). The mean aspect ratio of the cores is $\langle b : a \rangle = 0.8 \pm 0.14$, i.e., they are somewhat rounder than the globule envelopes. However, this latter difference is not significant since beam-smoothing does affect the cores more than the envelopes. The mean angular diameter of the cores derived this way is for all sources more than twice as large as the beam (*HPBW* 36″.4), and for half of the sources more than three times larger. Hence,

the effect of the beam size on the core definition is weak, although not completely negligible in some sources. A more severe limitation on the accuracy of core mass estimates may come from the fact that in the presence of unresolved warm protostars and large LoS temperature gradients, the column density maps are corrupted at the location of the protostar and the peak column density can be underestimated (see Sect. 4.2). In these cases, the core masses are underestimated and the core sizes have larger uncertainties.

The mean total hydrogen mass of all dense cores in our sample is $1.2 \pm 0.9\ M_\odot$, with the lowest-mass core being in B 335 (0.2 $M_\odot$), the highest-mass core in BHR 12 (3.7 $M_\odot$), and no significant systematic difference between starless and protostellar cores. The cores in single-core globules contain on average $25 \pm 6\%$ of the total mass of the globule, irrespective of whether they already contain a protostar or not. In globules with two cores (CB 26 and CB 244), the total core mass fraction is comparable ($30 \pm 5\%$), but the individual cores constitute only $15 \pm 6\%$ of the total globule mass. In terms of their luminosity, starless
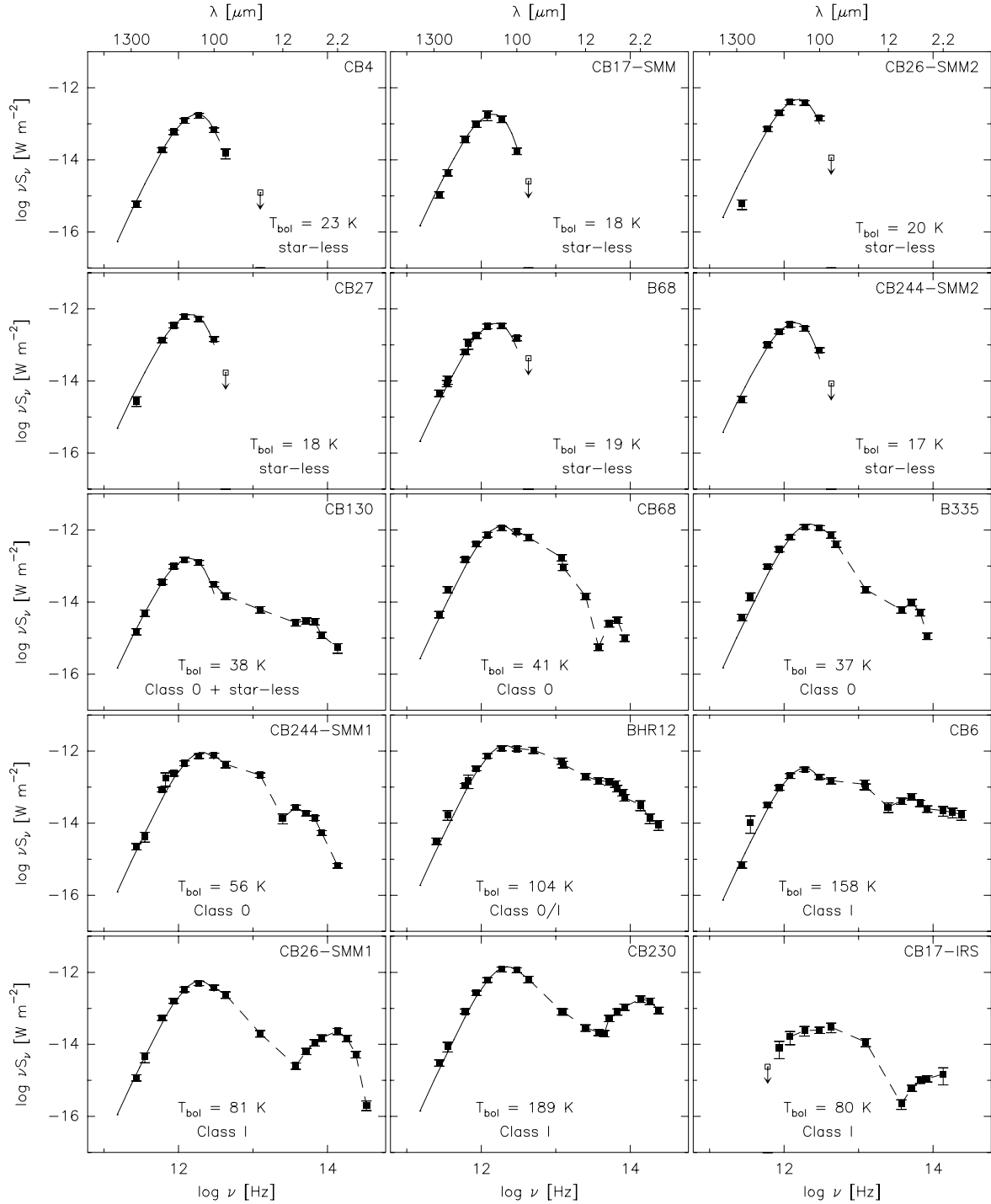
Fig. 4. Integrated spectral energy distributions of the dense cores and embedded sources listed in Table 6. Fluxes are integrated within the $N_{1'}$ contour (Eq. (10)), as are the core masses and luminosities listed in Table 6. Solid lines between 3 mm and 100 μm mark the modified blackbody fits to the data points, while dashed lines only represent a logarithmic interpolation of the data points shortward of 100 μm (see Sect. 5.3).

and protostellar cores are more distinct from each other. The mean bolometric luminosity of the seven starless cores (Table 6, including CB 130) is $0.43 \pm 0.15\ L_\odot$, while that of the cores with embedded protostars is $4.5\ L_\odot$ with a large scatter ranging from $0.5\ L_\odot$ to $15\ L_\odot$ (excluding CB 17 - IRS). The dense starless cores emit on average $20 \pm 5\%$ of the total luminosity of their hosting globules, while protostellar cores emit on average $40 \pm 10\%$. These relations are discussed in more detail and in the context of the thermal structure of the globules and the relative effects of external and internal heating in Sect. 5.6.

5.4. Evolutionary stage tracers

The spectral classes and the approximate evolutionary stages of the sources in our sample were already known from earlier observations and modeling (see Table 1 and Launhardt et al. 2010). With the *Herschel* data in hand, which provide a much more complete coverage of the thermal SEDs and allow for more robust mass, luminosity, and T_{bol} estimates than before, we re-evaluate the classical evolutionary tracers $L_{\mathrm{smm}}/L_{\mathrm{bol}}$ (André et al. 1993) and T_{bol} (Myers & Ladd 1993). Figure 5 shows the $L_{\mathrm{smm}}/L_{\mathrm{bol}}$ ratio vs. T_{bol} for all dense cores in the 12 globules of
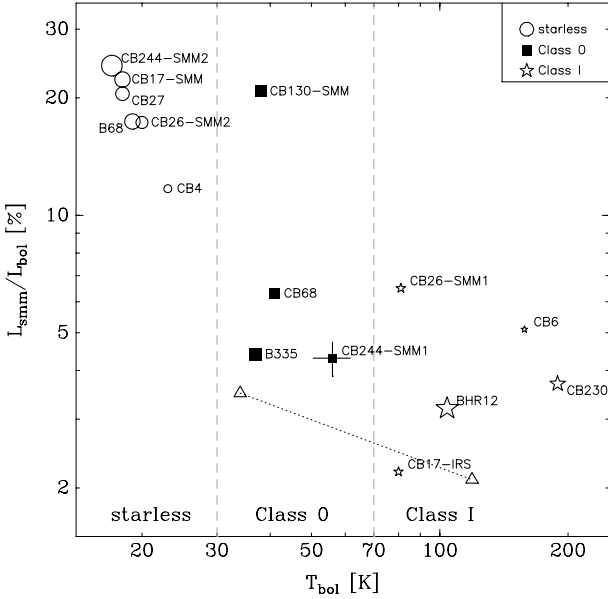
Fig. 5. L_{bol}/L_{submm} ratio vs. bolometric temperature of the globule cores (see Table 6 and Sect. 5.4). The size of the symbols scales with the peak column density of the respective sources. Error bars on CB 244 - SMM1 illustrate the 10% relative uncertainty on both values (Sect. 5.4). The "classical" T_{bol} boundaries for Class 0 protostars are indicated by the vertical dashed lines. The two triangles, connected by a dotted line, represent one synthetic protostar-envelope system taken from (Robitaille et al. 2006), once seen close to edge-on (T_{bol} = 34 K) and once seen nearly pole-on into the outflow cavity (T_{bol} = 119 K; see discussion in Sect. 5.4).

our sample. Uncertainties of these values are not straig-forward to assess because the formal error bars are much smaller than the effect of exactly how a core and the respective integration area are defined. Based on tests with slightly different core definitions we estimate the relative uncertainties to be about 10%. In contrast to earlier "pre-*Herschel*" papers, the new L_{smm}/L_{bol} vs. T_{bol} diagram now also includes purely externally heated starless cores. At the end of this section, we also use complementary information to relate the empirical "Class" of the individual sources to their actual evolutionary stage.

All starless cores in our sample, i.e., cores that do not have a compact 100 μm source or any other signs of central heating or star formation, have T_{bol} < 25 K and 10% < L_{smm}/L_{bol} < 30%. We also find a correlation between T_{bol} and L_{smm}/L_{bol} ratios and both mass and peak column density of starless cores in the sense that colder cores (lower T_{bol}) with higher L_{smm}/L_{bol} ratios tend to be more massive (see Fig. 5). Since these cores have no significant internal heating sources, this correlation is likely to reflect purely the degree of external heating by the ISRF and shielding rather than an evolutionary effect (see also discussion in Sect. 5.7). Massive cores with higher column densities are better shielded and can cool down more than less-massive and less-shielded cores. Even in the unlikely case that some of these cores would already have undetected first hydrostatic cores (FHSCs), their existence would have no measurable effect on T_{bol} or the L_{smm}/L_{bol} ratio. Furthermore, an evolution of these integral quantities through the lifetime of the FHSC is for the same reasons also not expected theoretically (e.g., Commerçon et al. 2012). On the other hand, cores in larger molecular clouds with active star formation may be expected to have both more shielding and a stronger local ISRF, which may lead to different

temperature profiles and different location in the L_{smm}/L_{bol} vs. T_{bol} diagram as compared to isolated cores.

All cores with embedded sources previously classified as Class 0 protostars are confirmed to have 30 K < T_{bol} < 70 K and and have 3% < L_{smm}/L_{bol} < 7%. The only exception is the core of CB 130 with the embedded VeLLO, which has L_{smm}/L_{bol} ~ 21%. All cores with embedded sources previously classified as Class I YSOs are confirmed to have T_{bol} > 70 K and have 2% < L_{smm}/L_{bol} < 7%.

While the L_{smm}/L_{bol} ratios we derive for the isolated Class 0 sources agree well with the upper half of the range of the values listed by, e.g., André et al. (2000) for Class 0 sources in larger molecular clouds, we find significantly higher (up to a factor of 10) L_{smm}/L_{bol} ratios for the more evolved Class I YSOs than derived and proposed as threshold by André et al. (1993) and André et al. (2000, $L_{smm}/L_{bol}^{(Class I)}$ < 0.5%). In fact, we do not find a significant systematic difference in the L_{smm}/L_{bol} ratios between Class 0 protostars and Class I YSOs, but see at most a slight trend. As in Launhardt et al. (2010), we argue here that this systematic difference in L_{smm}/L_{bol} ratios between isolated and embedded Class I YSOs is unlikely to be an artifact of distance bias, angular resolution, or SED coverage, but rather reflects a combination of different methods of identifying the core boundaries and possibly real environmental differences. Luminosities for these earlier embedded samples were derived by Andre & Montmerle (1994), Moriarty-Schieven et al. (1994), and others based on IRAS point source fluxes and ground-based 800 and 1100 μm or 1.3 mm maps only. The compact, warm embedded sources dominate the small submm maps completely and the remaining low-level emission from a possible envelope was most likely chopped out to a large extent against the extended emission from the surrounding cloud (inter-core) material. Hence, these older observations could not correctly account for the envelope emission. In contrast, the column density profile of a globule core continuously decreases toward the "edge" of the small cloud, the isolated envelopes are heated more by the ISRF, and we do have spatially resolved emission maps at wavelengths between 100 μm and 1.3 mm at hand. The net effect is that we recover more envelope emission than those earlier observations and the envelopes of the isolated sources are more luminous than those of the embedded sources, thus elevating the L_{smm}/L_{bol} ratios.

When trying to interpret the quantities T_{bol} and L_{smm}/L_{bol} as evolutionary tracers, one has to keep in mind that, as soon as an outflow starts to open a cavity in the envelope, i.e., already early in the Class 0 collapse phase, the observed SED at wavelengths shortward of the thermal peak at $\lambda \approx 160 \mu$m becomes highly dependent on the viewing angle (e.g., Whitney et al. 2003; Enoch et al. 2009; Offner et al. 2012). Correspondingly, as long as one does not take into account the full source geometry, but instead simply integrates the observed fluxes over 4π, quantities derived from the SED also become projection-dependent. To illustrate this, we take one specific synthetic protostar - envelope system from Robitaille et al. (2006, model ID: 3008984) with properties similar to our "Class 0" sources (stellar and envelope mass, luminosity, envelope radius, etc.), and analyze its synthetic SED in the same way as our real sources. This synthetic source is once "observed" close to edge-on (i = 87°, w.r.t. the outflow axis), and once close to pole-on (i = 18°). Although the absolute L_{smm}/L_{bol} ratios derived for this model are systematically somewhat lower than those of our real sources, possibly due to a combination of the simplicity of the specific model and the same physical reasons as discussed above, the T_{bol} values for the two projections (34 K and 119 K) and the L_{smm}/L_{bol} trend cover the

full range of "Class 0" and "Class I" sources (see Fig. 5). Hence, without involving more specific information on the opening angle and orientation of the outflow cavities, e.g., from NIR images and high-resolution molecular line maps, together with radiative transfer modeling, a robust evolutionary classification of sources with $T_{bol} > 30$ K just from the SEDs is not possible. Protostars seen pole-on have SEDs that can be very similar to those of more evolved YSOs ("Class I" stage) seen edge-on, i.e., for individual sources there is no clear one-to-one correspondence between spectral Class and evolutionary stage.

For CB 26 - SMM1, we know that it is seen nearly edge-on (Launhardt et al. 2009), i.e., its classification as YSO in the Class I evolutionary stage seems to be robust. BHR 12 is harder to judge since the two sub-cores with misaligned outflows are not resolved in our SED. However, the NIR images also seem to indicate that we are viewing them nearly edge-on (e.g., Hodapp & Ladd 1995). Hence, their classification as YSOs in the Class I evolutionary stage seems also robust. For CB 6 and CB 230, the NIR images suggest that we are at least partially looking into the outflow cones (Launhardt et al. 2010), i.e., they could well be protostars (Class 0 evolutionary stage) seen pole-on.

5.5. Stability of starless cores

We evaluate the total gravitational potential and thermal kinetic energies of the starless cores and compare their central densities with the theoretically predicted maximum stable central density of self-gravitating cores to assess which cores are unstable against gravitational collapse und must therefore be prestellar in nature, and which ones are stable.

In a first step, we calculate the gravitational potential energy of the cores as

$$E_{grav} = -\frac{GM^2}{R}\alpha_{vir},\qquad(12)$$

with G being the gravitational constant, and using $R = r_2$ (Eq. (6) and Table 5), $M = M_2$ the total gas mass enclosed in the N_2 contour (Eq. (7), mass not explicitly listed here), and the profile shape correction factor $\alpha_{vir} = 0.75(\pm0.15)$ (Bertoldi & McKee 1992; Sipilä et al. 2011). The thermal kinetic energy is calculated as follows:

$$E_{therm} = \frac{3}{2}\frac{MkT}{\mu m_H} \approx \frac{3kd^2}{2\mu}\int N_H T d\Omega,\qquad(13)$$

with k being the Boltzmann constant, $\mu = 2.33$ the mean molecular weight, m_H the proton mass, and $N_H \times T$ being integrated within the N_2 contour. Figure 6 (top) shows for the starless cores in our sample the ratio of gravitational to thermal energy vs. total gas mass M_2. The turbulent energy content of the starless cores (derived from $C^{18}O(2-1)$ line widths; Lippok et al., in prep.). is by a factor 20–50 lower than the thermal energy for all cores and is thus negligible in this balance. Given the uncertainties involved in this estimate, this energy ratio indicates that CB17 - SMM, CB 26 - SMM2, CB 27, and B 68 are all gravitationally bound and approximately stable. CB244 - SMM2 must be supercritical, which is consistent with the conclusion derived by Stutz et al. (2010), and CB 4 does not seem to be gravitationally bound.

We also estimate the central volume number density of the starless cores by assuming spherical symmetry and dividing the peak column density N_0 by the flat core radius r_1 (Eqs. (3), (4) and Table 5) and plot it in Fig. 6 (bottom) against the total gas mass M_2. Also indicated in this plot is the maximum stable central density of a pressure-supported, self-gravitating modified
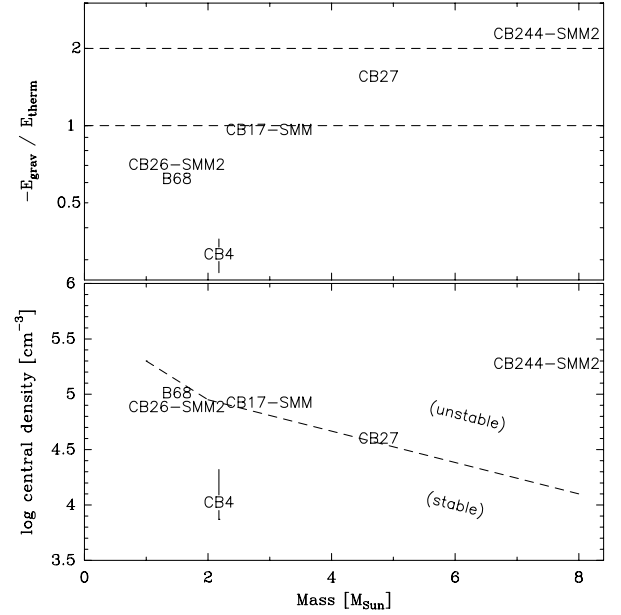

Fig. 6. Stability of starless cores. *Top*: ratio of gravitational potential to thermal kinetic energy vs. total gas mass ($1.36 \times M_H$), both integrated within the N_2 column density contours (Table 5). The lower dashed horizontal line marks the bounding limit of $-E_{grav}/E_{therm} = 1$, while the upper line marks the state of virialization at $-E_{grav}/E_{therm} = 2$. *Bottom*: estimated central density (see Sect. 5.5) vs. total gas mass for the same starless cores. The dashed line marks the maximum stable density of a pressure-supported, self-gravitating modified (nonisothermal) BES (with photoelectric heating at the core boundary taken into account) as calculated by Keto & Caselli (2008, their Fig. 14). Typical estimated uncertainties on the source parameters are indicated as Y error bars on CB 4. The uncertainty in mass corresponds to the size of the label.

(nonisothermal) Bonnor-Ebert sphere (BES; Bonnor 1956; Ebert 1955), calculated by Keto & Caselli (2008, their Fig. 14). For comparison with the isolated globule cores, we adopt their results for the model with photoelectric heating at the core boundary. This evaluation supports the previous conclusions even more clearly, i.e., CB17 - SMM, CB 26 - SMM2, CB 27, and B 68 are all gravitationally bound but seem to be thermally subcritical and just at the limit of stability.

This complies well with the notion that the mean radii of the globules are similar to or only slightly larger than their Jeans lengths (Sect. 5.3). Interestingly, the projected separations between the two sub-cores in CB 26 (0.15 pc) and CB 244 (0.09 pc) agrees quite well with the typical Jeans lengths in these clouds (~0.13 pc; see Sect. 5.3), indicating that large globules tend to fragment gravitationally on the Jeans scale. Also interesting in this respect is that in both globules one of the two cores has already formed a protostar, while the other one is still starless/prestellar.

CB 4 is clearly a subcritical globule and must be purely pressure-confined. CB 244 - SMM2 must be a supercritical prestellar core on the verge of collapse, unless it has significant other nonthermal support like, e.g., strong magnetic fields. The CB 244 region was studied by Wolf et al. (2003) with sub-mm polarization observations. The SMM1 core was indeed found to exhibit a relatively strong magnetic field ($257\,\mu G$). However, the snr for the SMM2 core was too low to derive a meaningful field strength. Hence, CB 244 - SMM2 is a good candidate to look for kinematic infall signatures or signs of a possibly already existing FHSC.
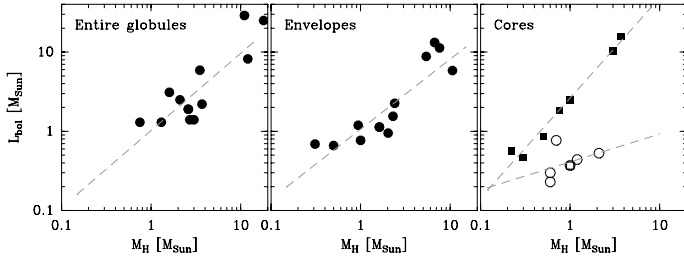
Fig. 7. Bolometric luminosity vs. total hydrogen mass of the entire globules (*left*), the envelopes only (without the dense cores; center) and the dense cores only (*right*; see Table 6 and Sect. 5.6). Filled squares in the right-most panel mark protostellar cores, empty circels mark starless cores, and the open square marks the core of CB 130 with the embedded VeLLO.

The finding that the majority of starless cores are bound and approximately stable is a natural consequence of a selection effect. Due to the short collapse time scales (at most 10^4 yrs, e.g., Schönke & Tscharnuter 2011), unstable cores should be indeed much less frequent than stable cores which can have lifetimes of up to 10^6 yrs (e.g., Enoch et al. 2008).

5.6. Thermal structure of the cores

Figure 7 shows the bolometric luminosity vs. total hydrogen mass of the entire globules, the dense cores only, and the envelopes only (globule minus core). All globules turn out to have about the same luminosity-to-mass ratio of 1.1 ± 0.6 $L_\odot/M_\odot$, irrespective of whether they harbor starless cores or protostars. The mean luminosity-to-mass ratio of the envelopes (cores subracted) is very similar, with somewhat lower scatter (1.0 ± 0.5 $L_\odot/M_\odot$). A significant difference in the luminosity-to-mass ratios between starless and protostar-harboring sources exists only for the central dense cores, with starless cores having 0.5 ± 0.25 $L_\odot/M_\odot$ and protostellar cores having 2.5 ± 1 $L_\odot/M_\odot$. This alone already points toward the dominating effect of the externally heated envelopes for the globules and the very local effect of internal heating by embedded (low-mass) protostars. The embedded protostars have very little effect on the overall energy balance of their host globule.

This dominating effect of external heating and shielding becomes even more evident in the radial profiles of the dust temperature and the local luminosity-to-mass ratios. Figure 8 shows these radial profiles along with the column density profiles for all resolved starless and protostellar cores as well as the mean profiles for these two groups. Both starless globules and globules harboring protostars approach at their outer boundaries, at radii of $\sim 5 \times 10^4$ AU and column densities of $\sim 10^{21}$ cm^{-2}, dust temperatures of 15.5 ± 1.5 K and local luminosity-to-mass ratios of 2 ± 1 $L_\odot/M_\odot$. From the outer boundaries inward, both the dust temperatures and local luminosity-to-mass ratios decrease to reach mean values of 12–13 K and ~ 0.4 $L_\odot/M_\odot$ at radii of ~ 5000 AU. Hence, all of these cores are far from being isothermal. They are heated externally by the IRSF and their innermost dense centers are well-shielded from the energetic short-wavelength radiation of this heating source. Local heating by the embedded protostars raises the dust temperature and local luminosity-to-mass ratio only inside radii of ~ 5000 AU, where the derived local temperature is only a lower limit due to the effects of beam-convolution and LoS-averaging. However, there are also some systematic differences between certain globules, which we attribute to differences in the shielding by extended

halos and difference in the local ISRF. This is discussed in the next section. Table 5 also lists the column density and temperature profile fit parameters of the mean profiles of protostellar and starless cores in our sample. Note that these mean profile parameters are averages of the individual source profile parameters, while the mean profiles shown in Fig. 8 are derived by fitting the averaged profiles. These observationally derived mean profile parameters can be used to construct representative cores for radiative transfer models. Such models must be able to explain not only the outer and inner dust temperatures, but also the temperature contrast between core and envelope.

5.7. Constraints on the interstellar radiation field

Figure 9 shows the central minimum (LoS-averaged) dust temperature, T_{in}, of all starless cores in our sample vs. their peak column density N_0 (see Table 5). The tight anti-correlation between total column density and central dust temperature indicates very clearly that the inner temperatures of passive molecular cloud cores (without internal heating sources) are controled by the shielding against the ISRF. It also indicates that these nearby and isolated globules are all exposed to about the same ISRF. The correlated errors between T_{in} and N_0 are much smaller than the range of values for these sources and therefore do not affect this conclusion.
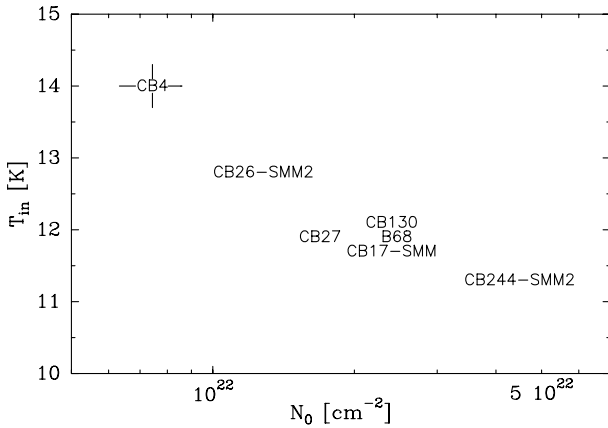
We also use the observed outer dust temperatures and halo column densities (N_{out}) of our sources to derive constraints on the mean ISRF. For this purpose, we compare the observed temperature profiles of the cores in this paper to a grid of 1D radiative transfer models (Shirley et al., in prep.). Dust temperatures are self-consistently calculated using the CSDUST3 code (Egan et al. 1988) for an input density profile, input dust opacities, and input heating conditions. The density profiles are isothermal BES with the BES temperature derived iteratively at the half-central density point of the profile from the radiative transfer calculation. The central densities of the BESs vary from 9×10^3 cm^{-3} to 6×10^6 cm^{-3} with the outer radius set to 30 000 AU. The dust opacities are taken from Ossenkopf & Henning (1994, OH5) and are augmented by scattering coefficients according to the prescription given in Young & Evans (2005). The heating is derived from the ISRF plotted in Fig. 3 of Shirley et al. (2005) and is modified in two ways: the overall strength of the UV to FIR ISRF is multiplied by a factor (S_{ISRF}), and the model core is assumed to be embedded within a medium with extinction given by $A_V(R_{out})$ affecting only the shortest wavelengths ($\lambda <$ few μm) of the ISRF. The final grid consists of 3600 models with self-consistently calculated dust temperature profiles.

Figure 10 compares the modeled relation between the outer temperature (at $R_{out} = 30\,000$ AU), the relative strengths of the ISRF, and the additional shielding of the cloud against the ISRF by a halo for a model core that matches the mean column density profile of the observed starless globules (Fig. 8) with the observed outer dust temperature and column densities of the outer halos (see Table 5). The observed outer temperatures range from 13.1 K to 19.5 K and occupy the upper half of the model outer temperatures which range from 8.1 K to 17.8 K. The general shape of the observed dependency of the outer temperature on the shielding against the ISRF agrees well with the model calculations, suggesting that the outer temperature is indeed controled to first order by the shielding against an approximately uniform (not necessarily isotropic) ISRF. The only source that deviates significantly from the observed relation toward higher outer temperature or stronger ISRF is BHR 12 (CG 30). This cometary
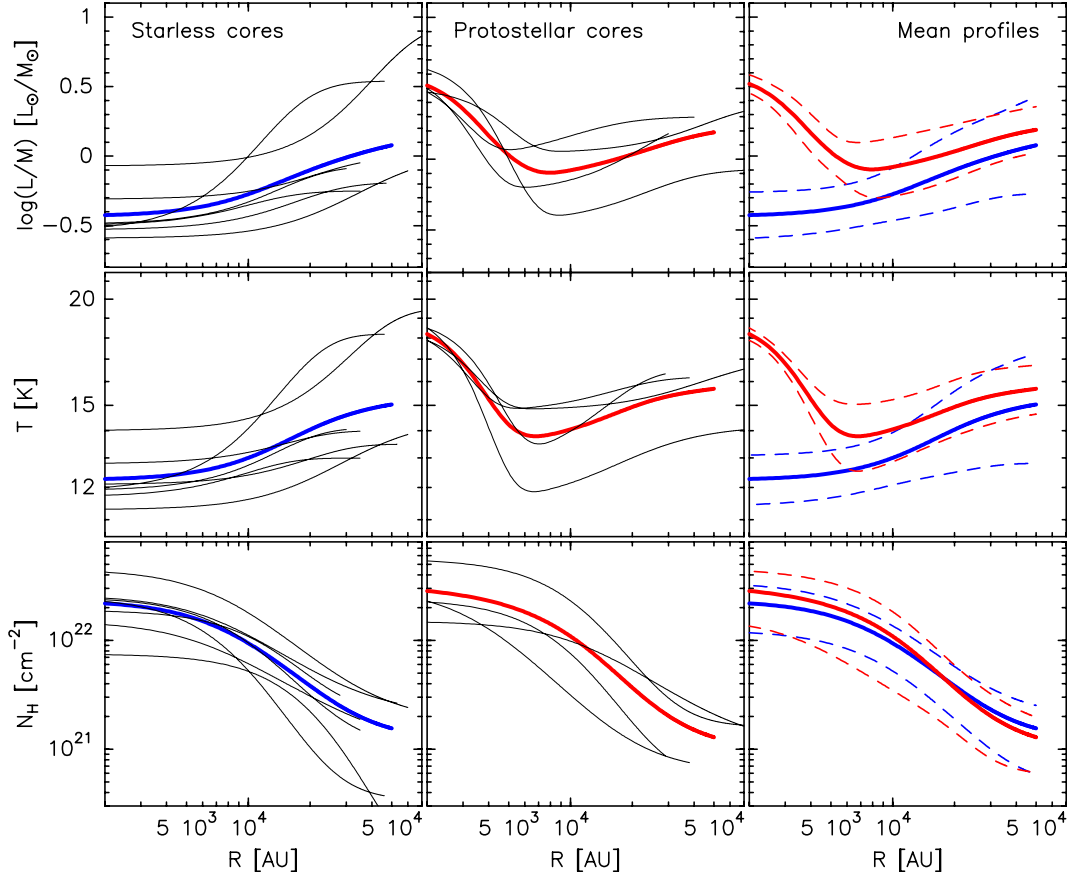
Fig. 8. Radially averaged column density profiles (*bottom*), LoS-averaged dust temperature (*center*), and luminosity-to-mass ratio profiles (*top*), for individual sources (thin black solid lines) as well as mean profiles (thick lines) of starless and protostellar cores. Note that the latter ones are fits to the mean profiles, while we list the means of the indivudual profile parameters in Table 5, which is not exactly the same. Thin lines in the rightmost panels indicate the 1σ uncertainty ranges of the mean profiles.

Fig. 9. Central minimum (LoS-averaged) dust temperature, T_{in}, of starless cores vs. peak column density N_0. Representative error bars are indicated only for CB 4.
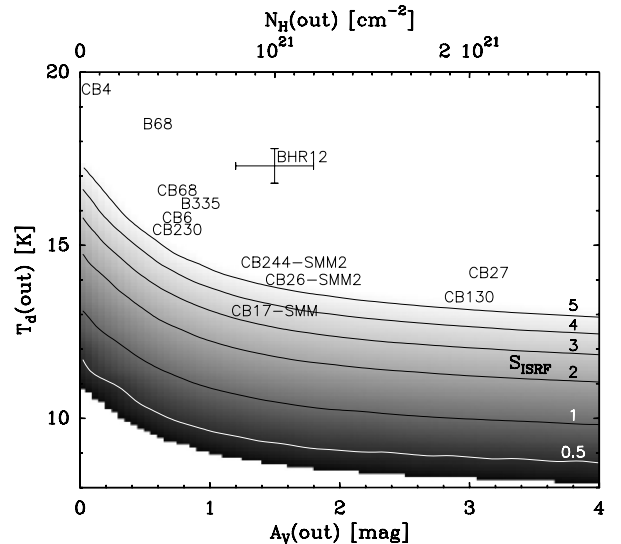
Fig. 10. Observed mean outer dust temperatures of the globules vs. column density of the outer halo (see Table 5). The conversion to A_V was done with the mean A_V-to-N_H ratio of $(1.5 \pm 0.5) \times 10^{-21}$ derived from the comparison of NIR extinction maps (not used further in this paper) of 9 globules and the N_H maps derived in this paper and thus remains somewhat uncertain. Errorbars on BHR12 mark uncertainties of ± 0.5 K for T_d and 20% for N_H(out), repectively. Plotted as grayscale and contours is the dust temperature at the outer radius (30 000 AU) of a model cloud, derived with the radiative transfer modeling descibed in Sect. 5.7, versus shielding of the cloud against the ISRF by a halo and as function of the relative strengths of the ISRF.

globule in the Gum nebula region is exposed to the Vela pulsar and supernova remnant (Large et al. 1968) and to the O4 supergiant star ζ Puppis, and might thus indeed experience a stronger local ISRF than the other globules (Fig. C.6).

However, the comparison between observations and model calculations also shows that the isolated globules have on average higher outer dust temperatures than predicted by Shirley et al. (2005). This is probably due to a combination of a stronger ISRF than adopted and lower submm opacities for grains with a smaller size distribution than OH5. For this calculation, we

used the same dust opacity model for both the dense cold cores and for the thin extended envelopes. OH5 opacities, which are calculated for coagulated dust grains with ice mantles, are certainly not appropriate for the thin extended halos around the globules. Though opacity models for smaller grains will not significantly affect the observational derivation of dust temperatures from the SEDs, they would lead to lower values of the derived outer column densities (by a factor of a few). At the same time, smaller grains would lead to higher outer dust temperatures in the self-consistently calculated models. These issues require further modeling before robust conclusions on the strength of the ISRF can be drawn and will be addressed in a forthcoming paper that will also include information from NIR extinction maps.

Nevertheless, the observed relation between outer dust temperatures and halo column densities complies very well with the general picture of external heating by the ISRF and, at the same time, suggests that our background flux level treatment and extended emission recovery (Sect. 4.1) worked well and that the detected "halos" indeed belong to the globules and do not represent unrelated background material.

5.8. Environmental effects

Although all globules selected for this study appear at first glance compact and not very filamentary, eight out of the 12 globules are cometary-shaped with one sharp rim and either a long cometary tail seen both in the optical cloudshine as well as in the FIR dust emission (e.g. CB 6, CB 17, CB 68), or at least a very diffuse side opposite the sharp rim (e.g., CB 26, CB 230; see Table 6 and Figs. C.1 through C.12). Most of these globules were not classified originally as cometary globules like, e.g., BHR 12 (CG 30; Zealey et al. 1983), but appear at first glance rather round and isolated when seen on less deep optical images or older dust emission maps. The diffuse tails have projected physical lengths between 0.3 pc (CB 27; Fig. C.5) and 2.6 pc (CB 6; Fig. C.2). In some cases, like CB 68, the long diffuse tail connects the globule to larger (diffuse) clouds (Figs. 2 and C.7). In other cases, like BHR 12, the cometary tail is pointing away from an energetic irradiating source (Fig. C.6). In some sources, like CB 17, neither a connection of the long tail to another structure nor an illuminating source could be clearly identified. This diversity suggests that cometary shape and tails may not have the same physical origin in all sources.

We also evaluated the location and orientation of warm rims on the outer edges of the globules (like, e.g., CB 26: Fig. B.4) and their relation to (potential) external heating sources, like nearby stars or the Galactic plane. Even though the one-sided warm rim appears at first glance questionable in some cases because we have recorded no information for the temperature of the opposite rim (e.g., CB 4 and CB 17: Figs. B.1 and B.3), the existence and location of the one-sided warm rims is indeed significant. The warm rims, were present, are on average 2 ± 0.4 K warmer than the opposite cold rims. Their presence can be understood by inspecting the PACS and SPIRE maps of, e.g., CB 4 (Fig. A.1). While the long-wavelength SPIRE maps, which are to first order sensitive to column density, show an approximate symmetry between northern and southern side of the globule (apart from the cometary tail), the shorter-wavelength PACS maps, which are more sensitive to temperature, show a significant asymmetry with much stronger emission on the southern side. Indeed, after fitting the data, the column density contours indicate an approximate symmetry between northern and southern side down to a few times 10^{20} cm^{-2} (Fig. B.1). At lower column densities, we can still derive the temperature at the warm

southern rim where the short-wavelength PACS emission is sufficiently strong. But on the northern side, the short-wavelength PACS flux densities drop below the detection threshold. Hence, we can no longer reliably derive a temperature for the cold material which is still traced by the SPIRE maps and may have the same column density as the warmer material on the southern side. When allowing the fitting routine to derive temperatures from only three (SPIRE) wavelengths (cf. Sect. 4.2), we obtain a temperature map that fully confirms the above result and rules out a misinterpretation due to a detection bias driven the data reduction. However, these SPIRE-only derived temperature maps are too unreliable and noisy to be used in the analysis of the source structure presented in this paper. Furthermore, the comparison of the results for CB 244 obtained with different versions of the data reduction and calibration pipeline (Sect. 6.1) also show that the extent and location of the warm south-eastern rim in CB 244 (Fig. B.12) remains unaffected by the specific data reduction version or background subtraction level.

Figures C.1 through C.12 show the large-scale morphology and surroundings of all regions studied in this paper, including the schematic indication of the warm rims and the location of potential external illumination sources. We find no clear indication for a general link between the loaction of the warm rim side in a globule and the location of identified potential external heating sources. In some globules, the warm rim points toward the Galactic plane (CB 26, B 68, CB 68, CB 230, CB 244: Figs. C.4, C.8, C.7, C.11, and C.12), in others it points in the opposite direction (CB 4, CB 27, CB 130: Figs. C.1, C.5, and C.9). In CB 6 (Fig. C.2) and CB 17 (Fig. C.3), there are bright nearby stars identified that could be located at the same distance and thus illuminate the globules directly. However, the warm rims do not point toward the potential illuminators. Except for BHR 12, no other nearby heating or illuminating sources could be uniquely identified. However, even in this globule, the tail pointing away from the illuminating source is significantly warmer than the side facing it (Figs. B.6 and C.6). Hence, we have to conclude that, as with the cometary tails, the link between warm rims and illuminating sources or the physical reason for the asymmetric warm rims remains inconclusive and needs to be addressed by future studies.

6. Discussion

6.1. Calibration and data reduction uncertainties

The total flux scale uncertainty of the *Herschel* data is assumed to be 15% (Sect. 4.1), while that for the ground-based submm bolometer data is about 20% (Sect. 3.2). These flux calibration uncertainties propagate directly into the column density and mass estimates. However, the effect on the dust temperature estimates should be much weaker for the following reason. Since all bands within one of the *Herschel* instruments were photometrically calibrated in a consistent way, any systematic uncertainties in the effective temperature of the calibrators should be correlated between the bands and thus to first order not affect the flux ratios that determine the temperature. There could still be a systematic offset between PACS and SPIRE due to different calibration procedures. However, if such an offset exists, it would have become immediately evident in the combined pixel-by-pixels SEDs since we have more than one wavelength band from each instrument. Since, after the background offset subtraction (Sect. 4.1), we did not notice any such offset, it must be very small (see also the integrated SEDs in Fig. 4). Similarly, any systematic errors that we could have possibly introduced in the various post-processing steps described in Sect. 4.1 (e.g.,

spatial filtering) should also be correlated to first order between the *Herschel* bands. Here we assess these effects quantitatively and estimate the uncertainties introduced by using different and older versions of HIPE and Scanamorphos for different sources (Sect. 3.1). In particular, we reprocessed all *Herschel* data from one source (CB 244, originally reduced with HIPE v. 5/6 and Scanamorphos v. 9) with the newest versions of HIPE (v. 9) and Scanamorphos (v. 18), with all additional post-processing steps (e.g., background subtraction) unchanged. The new reduction resulted in up to 20% lower PACS fluxes (as compared to the old reduction), but left the SPIRE fluxes unchanged within ≈1%. As a result, the LoS-averaged dust temperatures derived with the newly processed *Herschel* maps are on average 2.2% lower than the old values, and the resulting column densities are on average 7.5% higher. We also interpret these numbers here as a general assessment of the possible changes that new data reduction versions might bring, since HIPE v. 9.1.0 may not be the "final" version.

The complementary ground-based submm data were obtained independently with different instruments and processed with the respective instrument pipelines. Not only are the calibration uncertainties between the instruments and with respect to *Herschel* no longer correlated, these data are also much more and in a different way affected by spatial filtering. The sum of these effects would make any results based on simple submm flux ratio maps very susceptible to a number of calibration uncertainites. However, in this paper we use all data in a combined analysis in which the dust temperature estimate is to first order determined by the flux ratios of the *Herschel* bands, while the column density is to first order determined by the long-wavelength SPIRE bands and the submm data. In order to quantify the effect of the calibration uncertainties on our temperature estimates, we carried out a Monte Carlo test on one pixel in the center of B 68, artificially increasing all *Herschel* fluxes by 15% and randomly modifying the three individual submm fluxes with an rms of 20% and fitting the SEDs in the same way as we did for the normal analysis. As a result, the mean temperature of that pixel was elevated by 0.2 K from 11.8 K to 12.0 K with an rms scatter of 0.2 K. The mean column density was elevated by 6% with an rms scatter of 10%.

The background subtraction described in Sect. 4.2 could have potentially introduced additional uncertainties. However, since $I_{bg} \ll B_{\nu}(10 \, \mathrm{K})$ at all wavelengths for all our sources, thanks to the initial source selection in regions of low background, the difference in the final temperature estimates between considering I_{bg} or setting $I_{bg} = 0$ is $\Delta T \leq 0.15 \, \mathrm{K}$. The uncertainty introduced by not knowing the exact level of the background, but still subtracting a mean guess of I_{bg}, is correspondingly smaller, i.e., negligible. We therefore estimate the overall relative 1σ uncertainty introduced by flux calibration and data processing uncertainties to be $\sigma_T \approx 3\%$ and $\sigma_N \approx 15\%$ (quadratic sums of individual contributions described above).

6.2. Uncertainties and limitations of the modeling approach

Throughout this paper, we used OH5 opacities (Ossenkopf & Henning 1994) for all sources and regions. Although this opacity model seems to be a reasonable assumption for this kind of sources, it is not well-constrained observationally and may not accurately reflect the actual dust properties of the individual objects. Furthermore, a single opacity model may not apply to both the dust in the cold dense cores, where coagulation and ice mantle growth may have affected the effective optical properties of the grains, and that in the thin and warm outer envelopes. Since

the data do not provide a direct and unambiguous constraint on the dust opacities (this will be subject of a subsequent paper), we tested the dependency of the temperature and column density estimation on different opacity models and report the results here in the form of an uncertainty discussion. In particular, we test for one source (B 68) how the temperature and column density estimates derived with the following five dust opacity models differ with respect to the use of OH5 opacities: (1) OH1 (MRN size distribution, Mathis et al. 1977); (2) OH8 (coagulated grains like OH5, but with thick ice mantles); (3) Weingartner & Draine (WD01) opacities for $R_V = 5.5$ (Weingartner & Draine 2001; Draine 2003)[11]; and (4, 5) two pure beta models with $\beta = 1.5$ and $\beta = 2.5$, normalized to OH5 (which has $\beta \approx 1.9$) at $\lambda = 500 \, \mu$m. The first three of these models lead to deviations in the derived temperature w.r.t. OH5 of about 4% (0.4 K at 10 K), with the maximum deviation occuring for WD01 in the warm envelope (9% or 1.6 K lower than the 18 K derived with OH5). The two extreme beta models result in ≈10% higher temperatures (w.r.t. OH5) for $\beta = 1.5$ or 14−18% lower temperatures for $\beta = 2.5$, respectively. Hence, we can safely assume that the systematic uncertainty of the dust temperatures listed in Table 5 and introduced by the uncertainty in the dust opacity model is $\Delta T \approx \pm 1 \, \mathrm{K}$. Since the assumption of ISM-like dust (e.g., OH1), which is probably more appropriate for the envelopes than OH5, leads to a reduction of the derived temperature by only a few per cent (w.r.t. OH5), the LOS-averaged temperature contrast between cores and envelopes could be systematically overestimated by ≈0.5 K, i.e., less than the absolute temperature uncertainty.

The LoS-averaged dust temperature maps presented in this paper provide a robust estimate of the actual dust temperature only for the envelopes in the projected outer regions, where the emission is optically thin at all wavelengths and LoS temperature gradients are negligible. Toward the core centers, where cooling and shielding or embedded heating sources can produce significant LoS temperature gradients and the observed SEDs are therefore broader than single-temperature SEDs, the local central dust temperature is overestimated (in the case of a positive gradient in cold sources) or underestimated (negative gradient in internally heated sources). E.g., for B 68, where we already derived a model that accounts for LoS gradients, we derive a local central dust temperature of $8.2^{+2.1}_{-0.7}$ K (Nielbock et al. 2012), which is 3.7 ± 1 K lower than the LoS-averaged temperature of 11.9 ± 1 K we derive in this survey overview paper. For CB 17, where the outer dust temperature is lower than in B 68 (Table 5), we derive a local central dust temperature that is only ≈1 K lower than the LoS-averaged dust temperature derived in this paper (Schmalzl et al., in prep.). Dust opacity model uncertainties cancel out to first order if we compare only results obtained with the same opacity curves. Thus, we systematically overestimate the minimal inner dust temperatures by 1–4 K, underestimate the outer envelope dust temperature by <0.5 K, and underestimate the temperature contrast between cold core and envelope by 1−4 K.

The effect of systematically overestimating the actual minimum inner dust temperatures on the column density and mass estimates is also not negligible and can be quite significant in individual cases. Figure 11 compares the column density profiles of B 68 derived with an isothermal assumption, the LoS-averaged SED fitting used in this paper, and the full RT approach used in Nielbock et al. (2012). In this rather extreme case (one of

---

[11] See http://www.astro.princeton.edu/~draine/dust/dustmix.html
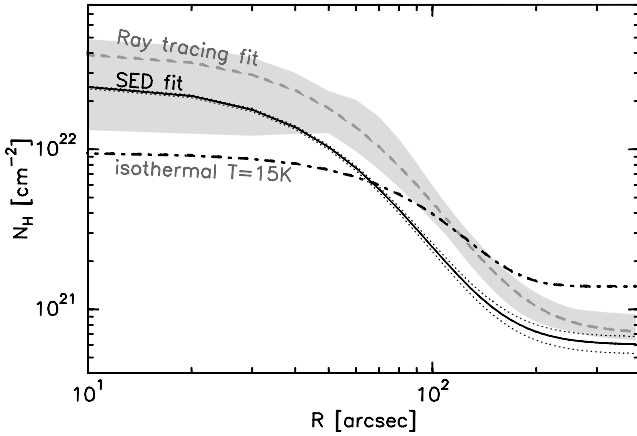
Fig. 11. Comparison of radial column density profiles of B 68, derived with the LoS-averaged temperature recovery method described in this paper (black solid line, uncertainty range marked by dotted lines), with the assumption of isothermal dust emission (dash-dotted line), and with a ray-tracing approach that takes LoS temperature gradients into account (gray dashed line, uncertainty range marked by gray-shaded area, Nielbock et al. 2012, corrected for OH5 opacities).

the highest core–envelope temperature contrasts in our sample), the LoS-averaged SED fitting underestimates the peak column density by a factor of ≈ 1.7 and the total mass by $\approx 15\%$. In sources with less-pronounced temperature contrast between core and envelope, like CB 17 (Schmalzl et al., in prep.), these systematic effects are weaker. Still, Fig. 11 also illustrates that the column density profiles recovered by our SED fitting approach are a much better approximation to the actual underlying source structure than those derived with an isothermal assumption.

The local temperature minimum and column density peak values are also affected by the angular resolution of our analysis. The $36\overset{''}{.}4$ beam size we use for all data may smooth out the central parts of the more centrally peaked profiles in some sources. Although we do not consider this effect being very significant for the starless cores, since the derived flat core radii are all significantly larger than the beam (see Sect. 5.3), it can only be verified quantitatively by using all data in their original resolution and employing full forward modeling. Beam-smoothing does affect the temperature and column density estimates much more at the position of embedded protostars where temperature and density gradients are far more pronounced and definitely not resolved. Here, the local temperatures at the position of embedded protostars are usually strongly underestimated and the temperature and column density maps are often corrupted by even very small residual pointing mismatches.

Hence, we can summarize that the uncertainties introduced by calibration and data reduction issues amount to $\approx 3\%$ for the temperature and $\approx 15\%$ for the column density. The uncertainties related to the dust opacity models are significantly larger and amount to ± 1 K ($\approx 10\%$) for the temperature and a factor of up to 3 for the column density and mass. Ignoring LoS temperature gradients leads to an overestimation of the central temperature minima in starless cores by about 1–3 K and an underestimation of the central column density by up to 50%. The temperatures and column densities of the outer envelopes are much less affected by this LoS-averaging.

The largest (systematic) uncertainties of the derived temperatures and (column) densities are clearly related to our uncertain knowledge of the underlying dust mass absorption coefficient and its spectral dependence. Therefore, our goal in future work

will be to exploit the *Herschel* data presented here along with additional complementary data to derive specific observational constraints on the properties of the dust in these globules (see also end of Sect. 7).

6.3. Comparison with earlier observations and models of dense cores

In this section we discuss some examples of previous work based on resolved observations of starless low-mass cores. For comparison with our new *Herschel* results, we specifically discuss published measurements of density and temperature profiles, as well as different attempts to model said temperature and density profiles.

The observed nonisothermality of dense clouds, derived from *Herschel* data, was already reported by other authors (e.g., Stutz et al. 2010; Peretto et al. 2010; Battersby et al. 2011; Wilcock et al. 2012; Pitann et al. 2013). While the Stutz et al. (2010) paper was the pilot study for the globule survey presented here, Peretto et al. (2010), Battersby et al. (2011), Wilcock et al. (2012), and Pitann et al. (2013) found that the LoS-averaged dust temperatures in IRDCs also systematically drop toward the highest column densities. Wilcock et al. (2012, Fig. 5) found temperature profiles of IRDCs that are qualitatively very similar to the profiles of the starless globules we report in this paper (Fig. 8), although their outer temperatures are on average ~5 K higher than those found here (20 K vs. 15 K). This is not surprising because IRDCs are generally located in distant regions of high-mass star formation with strong MIR background and may on average be exposed to a stronger ISRF than the nearby isolated globules in the local spiral arm. In more nearby sources, low central temperatures and positive temperature gradients were also inferred from observations and modeling of molecular lines in prestellar cores (e.g., Pagani et al. 2007; Crapsi et al. 2007).

Ward-Thompson et al. (2002) already found observational evidence for temperature gradients and colder interiors of starless cores using flux ratio maps of 170 and 200 μm observed with ISOPHOT. Bacmann et al. (2000) observed 24 dense starless cores in absorption with ISOCAM at $6''$ angular resolution. From modeling of the 7 μm absorption against the MIR background, they derived core structures characterized by a central flat region of $R_{flat} \approx 4000-8000$ AU, central column densities of a few 10^{22} cm^{-2}, and outer radial column density profiles close to $N_H \propto r^{-1}$. While the Bacmann et al. (2000) mean peak column densities agree well with the values we derive, our analysis results in somewhat larger flat-core radii and significantly steeper column density profiles (Table 5), which might at least partially be attributable to the larger beam sizes of our maps as compared to the Bacmann work.

Schnee & Goodman (2005) used 450 and 850 μm SCUBA observations to derive the dust temperature profile of the nearby starless core TMC-1C from the 450/850 μm flux ratio (assuming optically thin emission and a fixed $\beta = 1.5$). They found a positive temperature gradient with a central dust temperature of 6 K and an outer temperature of 12 K at the edge of the core (at 0.08 pc). They derived similar column densities as we find for the globule sources and modeled the density profile with a broken power-law with a shallow density profile inside ~4000 AU and $n \propto r^{-1.8}$ outside. Since the break radius of a broken power-law model of the density is not the same as the parameter r_1 of our column density profile fits (Eq. (3)) and should be somewhat smaller, their flat core radius is comparable or slightly smaller (up to a factor of two) than what we derive for the globule cores. Their outer density profile exponent of 1.8

is significantly lower than what would be implied by the column density profiles we derive here (Table 5) and the density profile of B 68 we derive in Nielbock et al. (2012). However, both the dependence of the resulting temperature on the above-mentioned assumptions as well as the nonnegligible calibration uncertainties of the SCUBA data, in particular at 450 μm, make the temperature scale and the (column) density profile derived from such flux ratios rather uncertain.

Shirley et al. (2000) also observed with SCUBA the 450 and 850 μm dust emission of 21 low-mass cores in different evolutionary stages. Based on these observations, Evans et al. (2001) modeled the emission of three starless cores within the context of a self-consistent radiative transfer analysis assuming a non-isothermal BES, modified OH5 dust opacities, and a modified Black (1994) and Draine (1978) ISRF. They found central densities between 10^5 and 10^6 cm^{-3} and required only fractions (0.3–0.6) of the adopted ISRF to reproduce the 450/850 μm flux ratios. They also derived positive temperature gradients with central dust temperatures of $7-8$ K and outer temperatures of $12-13$ K and found that the ISRF was the dominant heating source in the absence of a nearby star (see also Zucconi et al. 2001). Given the fact that our LoS-averaged dust temperatures overestimate the actual central temperatures by $1-4$ K, their derived central temperatures are still $2-3$ K lower than what we find here. However, one has to keep in mind that this is based on very low-number statistics and that their three cores are on average denser and more massive than ours. Therefore, this small difference in central temperatures might be real and reflect different source properties. Their outer temperatures, which are not well-constrained by the observations, are also $2-3$ K below the observationally well-constrained values we derive. However, without comparing the same sources, it is not possible to verify whether this reflects real differences in the shielding or is the result of the specific assumptions for the dust properties and the strength of the ISRF they made (see also discussion in Sect. 5.7). However, the same remarks apply as made above about the uncertainty of such quantities that are based only on SCUBA flux ratios.

Shirley et al. (2002) modeled the Class 0 cores from the Shirley et al. (2000) sample by including the internal radiation field from the protostar in addition to the heating from the ISRF to reproduce the 450 and 850 μm fluxes. They found that the dust temperature exceeded 20 K only in the inner $\approx 10^3$ AU, reached ≈ 10 K at $r \approx 5000-8000$ AU, and increased again slightly toward the outer boundary of the core at a few 10^4 AU. This is consistent with what we find, including the temperature rise at $r > 10^4$ AU, taking again into account that we overestimate the inner minimum temperature by up to 3 K, and that their models appear to underestimate the outer temperatures by $2-3$ K.

Stamatellos et al. (2005) calculated temperature profiles in the context of an evolutionary model, starting with a 5.4 $M_\odot$ BES and assuming OH5 dust opacities and a modified Black (1994) ISRF. In the initial stage, when only the ISRF heats the core, they found a central temperature of ~7 K and outer temperatures of up to ~20 K. Stamatellos et al. (2007) further studied the influence of external heating and shielding on the temperature profile of cores in the ρ Oph cloud, taking into account also the surrounding molecular cloud extinction. They found again that the inner core temperatures (at $r < 10^4$ AU) are always below 10 K, but derived rim temperatures (at $r \approx 2 \times 10^4$ AU) of only ~13–15 K. They noted that in Taurus, where the ambient radiation field is weaker, the core temperatures are found to be somewhat lower with a central value of ≈ 7 K and rim temperature of ≈ 12 K for TMC-1C. These temperatures and temperature contrasts are again consistent with what we now measure from

the *Herschel* data in similar cores. In particular the outer temperatures we measure for the isolated globules with their thin halos are all in between the values these authors derived for the unshielded and the well-shielded cores.

7. Summary and conclusions

We study the thermal dust emission from 12 nearby isolated globules using FIR dust continuum maps at five wavelength bands between 100 and 500 μm obtained with the *Herschel* satellite and submm continuum maps at up to three wavelengths beween 450 μm and 1.2 mm obtained with ground-based telescopes. Great care is taken in both the selection of truly isolated and previously well-characterized sources in regions of exceptionally low background emission and in restoring and calibrating all maps in a consistent manner to enable a combined in-depth analysis of all data. This careful preselection, data treatment, and the very deep 100 μm maps (~50 μJy/arcsec^2 rms) are essential to enable our analysis method and lead to the results presented here.

We calibrate all data to the same flux scale, subtract all general background levels in a consistent way, convolve all maps to the same angular resolution, assign weights to each pixel according to calibration uncertainties and rms noise, and extract full SEDs from 100 μm to 1.2 mm for each image pixel. These individual SEDs are independently fit (least squares) with single-temperature modified blackbody curves, using OH5 opacities for mildy coagulated dust grains with thin ice mantles. Thus, we obtain for each image pixel a column density and an LoS-averaged dust temperature. The resulting dust temperature maps have rms noise levels of only a few tenth of a K and systematic uncertainties of less than ±1 K. We then analyze the dust temperature and column density maps along with the integrated SEDs of all sources, including additional archival data at shorter wavelengths, and obtain the following main results:

1. The globules in our sample have a mean distance from the Sun of 240 ± 100 pc, mean total gas mass of 7.3 ± 6.8 $M_\odot$, mean bolometric luminosity of ≈ 6.7 $L_\odot$, and mean outer diameter of 0.45 ± 0.2 pc. Typical peak column densities (averaged over the 36.″4 beam) are $\langle N_{\rm H} \rangle \approx 3 \times 10^{22}$ cm^{-2}, which corresponds to peak visual extinctions of about 45 mag.

2. The dense cores of the globules have a mean total gas mass of 1.6 ± 1.2 $M_\odot$ and a mean diameter of 0.12 ± 0.05 pc. They constitute on average 25 ± 6% of the total globule mass.

3. Out of the 12 globules in our sample, four contain one starless core each, six contain a protostellar core (Class 0 or I), and two globules contain each one starless and one protostellar core.

4. We confirm the earlier classifications of protostars and embedded YSOs, but the better-sampled thermal SEDs do not allow for better evolutionary stage determination from the SEDs alone since projection effects dominate the spectral appearance of even Class 0 protostars. However, the *Herschel* data allow us now to also include starless cores in the $L_{\rm smm}/L_{\rm bol}$ vs. $T_{\rm bol}$ diagram (Fig. 5). We find that all starless cores have $T_{\rm bol} < 25$ K and $10\% < L_{\rm smm}/L_{\rm bol} < 30\%$. In particular the criterion $T_{\rm bol} < 25$ K can be used to identify isolated and externally heated starless cores, since even an embedded VeLLO will elevate $T_{\rm bol}$ above 30 K.

5. Most globules are surrounded by a thin ($A_V \approx 1-3$ mag) and warm ($T_{\rm d} \approx 15-20$ K) outer halo, the full extent of which we could not properly recover in most cases. These halos are evident in the dust emission-based column density maps,

NIR extinction maps, as well as in many cases on optical images as cloudshine.

6. The thermal structure of all globules is dominated by external heating through the ISRF, with warm outer envelopes (15.5 ± 1.8 K) and colder interiors (<13 ± 1 K). We find a very tight anti-correlation between the minimal central temperatures in starless cores and the total column density toward the outer edge that provides shielding against the ISRF (Fig. 9).

7. The outer dust temperature of the globules is to first order determined by external heating from an approximately uniform ISRF and shielding by thin extended halos. We find a clear anti-correlation between the outer dust temperatures and the mean column density/A_V of the halos (Fig. 10). Only one of the globules is exposed to a significantly higher than average local ISRF (BHR 12).

8. The embedded (low-mass and low-luminosity) protostars raise the local temperature of the dense cores only within radii out to about 5000 AU, but do not significantly affect the overall thermal balance of the globules.

9. Our LoS-averaged dust temperatures are accurate to about ±1 K at the outer boundaries of the globules (accounting for both statistical and systematic errors), but systematically overestimate the local central temperature minima by 1–4 K, depending on the temperature contrast to the outer rim. Thus, these globules have central dust temperatures in the range 8–12 K and temperature contrasts to the outer rim of 3–8 K. Note that the gas temperature is expected to be closely coupled to the dust temperature only in the central dense cores, but is likely decoupled and can be significantly higher toward the outer rim where the gas density drops well below 10^4–10^5 cm^{-3}.

10. Out of the six starless cores in our sample, five cores are found to be thermally stabilized against gravitational collapse. Of these, four cores (CB 17 - SMM, CB 26 - SMM2, CB 27, and B 68) have central densities that are very close to the maximum stable density of a pressure-supported, self-gravitating cloud, i.e., we cannot distinguish wheter they are starless stable or prestellar. CB 4 is thermally sub-critical and must be a purely pressure-confined starless core. The starless core in CB 244 - SMM2 is clearly super-critical and should very likely be a prestellar core on the verge of collapse.

11. The radius of the single-core globules is very similar to or only slightly larger than their Jeans length (~0.13 pc). The projected core separation in the two double-core globules agrees well with the Jeans lengths in these clouds, indicating that large globules tend to fragment gravitationally on the Jeans scale.

12. Many of the globules have one side that is signifcantly warmer than the other side at the outer rim. Although in some cases the warm side faces the direction toward the Galactic plane, we could not identify a consistent relation between warm side and potential external illuminating sources.

As a next step, we are currently analyzing individual starless cores by employing a ray-tracing algorithm that is able to restore LoS temperature gradients and derive the actual volume density structure of the cores by starting from a 1D model and allowing for local deviations from spherical symmetry (Nielbock et al. 2012; Schmalzl et al., in prep.). This way we hope to better and most robustly constrain the dust temperature structure of these cores without introducing too many model-dependent assumptions into the analysis. We are also working toward better constraining the dust opacity models. For this purpose, we have already obtained deep NIR extinction maps that recover the same angular resolution as the *Herschel* data and are currently obtaining additional deep submm and mm continuum maps. We are planning to employ and compare different approaches, including SED fitting and ray-tracing like in this paper and in Nielbock et al. (2012), self-consistent radiative transfer modeling like in Shirley et al. (2011), as well as Bayesian approaches like in Kelly et al. (2012). Furthermore, we are currently also using complementary molecular line data to derive constraints on the distribution of turbulence and molecular gas-phase freeze-out onto dust grains in the sources studied in this paper (Lippok et al., in prep.).

References

Agladze, N. I., Sievers, A. J., Jones, S. A., Burlitch, J. M., & Beckwith, S. V. W. 1996, ApJ, 462, 1026

Alves, F. O., & Franco, G. A. P. 2007, A&A, 470, 597

Alves, J. F., Lada, C. J., & Lada, E. A. 2001, Nature, 409, 159

Andre, P., & Montmerle, T. 1994, ApJ, 420, 837

Andre, P., Ward-Thompson, D., & Barsony, M. 1993, ApJ, 406, 122

Andre, P., Ward-Thompson, D., & Barsony, M. 2000, Protostars and Planets IV, 59

André, P., Bouwman, J., Belloche, A., & Hennebelle, P. 2004, Ap&SS, 292, 325

Aniano, G., Draine, B. T., Gordon, K. D., & Sandstrom, K. 2011, PASP, 123, 1218

Bacmann, A., André, P., Puget, J.-L., et al. 2000, A&A, 361, 555

Battersby, C., Bally, J., Ginsburg, A., et al. 2011, A&A, 535, A128

Bergin, E. A., & Langer, W. D. 1997, ApJ, 486, 316

Bergin, E. A., & Tafalla, M. 2007, ARA&A, 45, 339

Bertoldi, F., & McKee, C. F. 1992, ApJ, 395, 140

Beuther, H., Henning, T., Linz, H., et al. 2010, A&A, 518, L78

Beuther, H., Tackenberg, J., Linz, H., et al. 2012, A&A, 538, A11

Bianchi, S., Gonçalves, J., Albrecht, M., et al. 2003, A&A, 399, L43

Black, J. H. 1994, in The First Symposium on the Infrared Cirrus and Diffuse Interstellar Clouds, 58, 355

Bonnor, W. B. 1956, MNRAS, 116, 351

Boudet, N., Mutschke, H., Nayral, C., et al. 2005, ApJ, 633, 272

Bourke, T. L., Hyland, A. R., Robinson, G., James, S. D., & Wright, C. M. 1995, MNRAS, 276, 1067

Burton, M. G. 1992, Aust. J. Phys., 45, 463

Caselli, P., Walmsley, C. M., Tafalla, M., Dore, L., & Myers, P. C. 1999, ApJ, 523, L165

Caselli, P., Walmsley, C. M., Zucconi, A., et al. 2002, ApJ, 565, 344

Charnley, S. B. 1997, MNRAS, 291, 455

Chen, X., Arce, H. G., Dunham, M. M., et al. 2012, ApJ, 751, 89

Commerçon, B., Hennebelle, P., Audit, E., Chabrier, G., & Teyssier, R. 2010, A&A, 510, L3

Commerçon, B., Launhardt, R., Dullemond, C. P., & Henning, T. 2012, A&A, 545, A98

Crapsi, A., Caselli, P., Walmsley, M. C., & Tafalla, M. 2007, A&A, 470, 221

Draine, B. T. 1978, ApJS, 36, 595

Draine, B. T. 2003, ARA&A, 41, 241

Dunham, M. M., Crapsi, A., Evans, N. J., II, et al. 2008, ApJS, 179, 249

Ebert, R. 1955, Z. Astrophys., 37, 217

Egan, M. P., Leung, C. M., & Spagna, G. F., Jr. 1988, Comput. Phys. Comm., 48, 271

Enoch, M. L., Evans, N. J., II, Sargent, A. I., & Glenn, J. 2009, ApJ, 692, 973

Foster, J. B., & Goodman, A. A. 2006, ApJ, 636, L105
Di Francesco, J., Evans, N. J., II, Caselli, P., et al. 2007, Protostars and Planets V, 17
Di Francesco, J., Johnstone, D., Kirk, H., MacKenzie, T., & Ledwosinska, E. 2008, ApJS, 175, 277
Evans, N. J., II, Rawlings, J. M. C., Shirley, Y. L., & Mundy, L. G. 2001, ApJ, 557, 193
Emerson, D. T., Klein, U., & Haslam, C. G. T. 1979, A&A, 76, 92
Enoch, M. L., Evans, N. J., II, Sargent, A. I., et al. 2008, ApJ, 684, 1240
de Geus, E. J., de Zeeuw, P. T., & Lub, J. 1989, A&A, 216, 44
Griffin, M. J., Abergel, A., Abreu, A., et al. 2010, A&A, 518, L3
Hauser, M. G., & Dwek, E. 2001, ARA&A, 39, 249
Henning, T., & Launhardt, R. 1998, A&A, 338, 223
Henning, T., & Stognienko, R. 1996, A&A, 311, 291
Henning, T., Linz, H., Krause, O., et al. 2010, A&A, 518, L95
Hily-Blant, P., Walmsley, M., Pineau Des Forêts, G., & Flower, D. 2010, A&A, 513, A41
Hodapp, K.-W., & Ladd, E. F. 1995, ApJ, 453, 715
Juvela, M., Pelkonen, V.-M., Padoan, P., & Mattila, K. 2006, A&A, 457, 877
Kainulainen, J., Lehtinen, K., & Harju, J. 2006, A&A, 447, 597
Kainulainen, J., Beuther, H., Henning, T., & Plume, R. 2009, A&A, 508, L35
Kandori, R., Nakajima, Y., Tamura, M., et al. 2005, AJ, 130, 2166
Kauffmann, J., Bertoldi, F., Bourke, T. L., Evans, N. J., II, & Lee, C. W. 2008, A&A, 487, 993
Kelly, B. C., Shetty, R., Stutz, A. M., et al. 2012, ApJ, 752, 55
Keto, E., & Caselli, P. 2008, ApJ, 683, 238
Kim, H. J., Evans, N. J., II, Dunham, M. M., et al. 2011, ApJ, 729, 84
Kirk, J. M., Ward-Thompson, D., & André, P. 2005, MNRAS, 360, 1506
Kiss, C., Klaas, U., & Lemke, D. 2005, A&A, 430, 343
Kreysa, E., Gemünd, H.-P., Gromke, J., et al. 1999, Infrared Phys. Technol., 40, 191
Kun, M. 1998, ApJS, 115, 59
Lada, C. J., Lada, E. A., Clemens, D. P., & Bally, J. 1994, ApJ, 429, 694
Lada, C. J., Huard, T. L., Crews, L. J., & Alves, J. F. 2004, ApJ, 610, 303
Large, M. I., Vaughan, A. E., & Mills, B. Y. 1968, Nature, 220, 340
Larson, R. B. 1969, MNRAS, 145, 271
Launhardt, R., & Henning, T. 1997, A&A, 326, 329
Launhardt, R., & Sargent, A. I. 2001, ApJ, 562, L173
Launhardt, R., Ward-Thompson, D., & Henning, T. 1997, MNRAS, 288, L45
Launhardt, R., Pavlyuchenkov, Y., Gueth, F., et al. 2009, A&A, 494, 147
Launhardt, R., Nutter, D., Ward-Thompson, D., et al. 2010, ApJS, 188, 139
Linz, H., Krause, O., Beuther, H., et al. 2010, A&A, 518, L123
Loinard, L., Mioduszewski, A. J., Torres, R. M., et al. 2011, Rev. Mex. Astron. Astrofis. Conf. Ser., 40, 205
Lombardi, M., Alves, J., & Lada, C. J. 2006, A&A, 454, 781
Mathis, J. S., Rumpl, W., & Nordsieck, K. H. 1977, ApJ, 217, 425
Moriarty-Schieven, G. H., Wannier, P. G., Keene, J., & Tamura, M. 1994, ApJ, 436, 800
Myers, P. C., & Ladd, E. F. 1993, ApJ, 413, L47
Motte, F., & André, P. 2001, A&A, 365, 440
Müller, T., Okumura, K., & Klaas, U. 2011, PACS Photometer Passbands and Colour Correction Factors for Various Source SEDs
Negrello, M., Magliocchetti, M., Moscardini, L., et al. 2004, MNRAS, 352, 493
Nielbock, M., Launhardt, R., Steinacker, J., et al. 2012, A&A, 547, A11
Nutter, D., Stamatellos, D., & Ward-Thompson, D. 2009, MNRAS, 396, 1851
Offner, S. S. R., Robitaille, T. P., Hansen, C. E., McKee, C. F., & Klein, R. I. 2012, ApJ, 753, 98
Olofsson, S., & Olofsson, G. 2009, A&A, 498, 455
Ossenkopf, V., & Henning, T. 1994, A&A, 291, 943
Ott, S. 2010, in ADASS XIX, ASP Conf. Ser., 434, 139
Padoan, P., Juvela, M., & Pelkonen, V.-M. 2006, ApJ, 636, L101
Pagani, L., Bacmann, A., Cabrit, S., & Vastel, C. 2007, A&A, 467, 179
Pagani, L., Steinacker, J., Bacmann, A., Stutz, A., & Henning, T. 2010, Science, 329, 1622

Pavlyuchenkov, Y., Wiebe, D., Launhardt, R., & Henning, T. 2006, ApJ, 645, 1212
Pavlyuchenkov, Y. N., Wiebe, D. S., Akimkin, V. V., Khramtsova, M. S., & Henning, T. 2012, MNRAS, 421, 2430
Penston, M. V. 1969, MNRAS, 144, 425
Peretto, N., Fuller, G. A., Plume, R., et al. 2010, A&A, 518, L98
Perrot, C. A., & Grenier, I. A. 2003, A&A, 404, 519
Pilbratt, G. L., Riedinger, J. R., Passvogel, T., et al. 2010, A&A, 518, L1
Pitann, J., Linz, H., Ragan, S., et al. 2013, ApJ, accepted [arXiv:1301.1163]
Plummer, H. C. 1911, MNRAS, 71, 460
Poglitsch, A., Waelkens, C., Geis, N., et al. 2010, A&A, 518, L2
Ragan, S., Henning, T., Krause, O., et al. 2012, A&A, 547, A49
Robitaille, T. P., Whitney, B. A., Indebetouw, R., Wood, K., & Denzmore, P. 2006, ApJS, 167, 256
Roussel, H. 2012 [arXiv:1205.2576]
Saraceno, P., Andre, P., Ceccarelli, C., Griffin, M., & Molinari, S. 1996, A&A, 309, 827
Sauter, J., Wolf, S., Launhardt, R., et al. 2009, A&A, 505, 1167
Schlegel, D. J., Finkbeiner, D. P., & Davis, M. 1998, ApJ, 500, 525
Schnee, S., & Goodman, A. 2005, ApJ, 624, 254
Schnee, S., Enoch, M., Noriega-Crespo, A., et al. 2010, ApJ, 708, 127
Schönke, J., & Tscharnuter, W. M. 2011, A&A, 526, A139
Shetty, R., Kauffmann, J., Schnee, S., Goodman, A. A., & Ercolano, B. 2009a, ApJ, 696, 2234
Shetty, R., Kauffmann, J., Schnee, S., & Goodman, A. A. 2009b, ApJ, 696, 676
Shirley, Y. L., Evans, N. J., II, Rawlings, J. M. C., & Gregersen, E. M. 2000, ApJS, 131, 249
Shirley, Y. L., Evans, N. J., II, & Rawlings, J. M. C. 2002, ApJ, 575, 337
Shirley, Y. L., Nordhaus, M. K., Grcevich, J. M., et al. 2005, ApJ, 632, 982
Shirley, Y. L., Huard, T. L., Pontoppidan, K. M., et al. 2011, ApJ, 728, 143
Shu, F. H. 1977, ApJ, 214, 488
Shu, F. H., Adams, F. C., & Lizano, S. 1987, ARA&A, 25, 23
Siebenmorgen, R., Kruegel, E., & Mathis, J. S. 1992, A&A, 266, 501
Sipilä, O., Harju, J., & Juvela, M. 2011, A&A, 535, A49
Smith, J., Werner, M. W., Lynch, D. K., & Cudaback, D. 1979, ApJ, 234, 902
Sodroski, T. J., Odegard, N., Arendt, R. G., et al. 1997, ApJ, 480, 173
Stamatellos, D., Whitworth, A. P., Boyd, D. F. A., & Goodwin, S. P. 2005, A&A, 439, 159
Stamatellos, D., Whitworth, A. P., & Ward-Thompson, D. 2007, MNRAS, 379, 1390
Stecklum, B., Launhardt, R., Fischer, O., et al. 2004, ApJ, 617, 418
Steinacker, J., Pagani, L., Bacmann, A., & Guieu, S. 2010, A&A, 511, A9
Straižys, V., Černis, K., & Bartašiūtė, S. 2003, A&A, 405, 585
Stutz, A. M., Rubin, M., Werner, M. W., et al. 2008, ApJ, 687, 389
Stutz, A. M., Rieke, G. H., Bieging, J. H., et al. 2009a, ApJ, 707, 137
Stutz, A. M., Bourke, T. L., Rieke, G. H., et al. 2009b, ApJ, 690, L35
Stutz, A., Launhardt, R., Linz, H., et al. 2010, A&A, 518, L87
Tobin, J. J., Hartmann, L., Looney, L. W., & Chiang, H.-F. 2010, ApJ, 712, 1010
Ward-Thompson, D., Scott, P. F., Hills, R. E., & Andre, P. 1994, MNRAS, 268, 276
Ward-Thompson, D., Motte, F., & Andre, P. 1999, MNRAS, 305, 143
Ward-Thompson, D., André, P., & Kirk, J. M. 2002, MNRAS, 329, 257
Weingartner, J. C., & Draine, B. T. 2001, ApJ, 548, 296
Whitney, B. A., Wood, K., Bjorkman, J. E., & Wolff, M. J. 2003, ApJ, 591, 1049
Whitworth, A. P., & Ward-Thompson, D. 2001, ApJ, 547, 317
Wilcock, L. A., Ward-Thompson, D., Kirk, J. M., et al. 2012, MNRAS, 424, 716
Wolf, S., Launhardt, R., & Henning, T. 2003, ApJ, 592, 233
Young, C. H., & Evans, N. J., II 2005, ApJ, 627, 293
Young, C. H., Shirley, Y. L., Evans, N. J., II, & Rawlings, J. M. C. 2003, ApJS, 145, 111
Zealey, W. J., Ninkov, Z., Rice, E., Hartley, M., & Tritton, S. B. 1983, Astrophys. Lett., 23, 119
Zucconi, A., Walmsley, C. M., & Galli, D. 2001, A&A, 376, 650

Appendix A: Dust temperature and column density maps
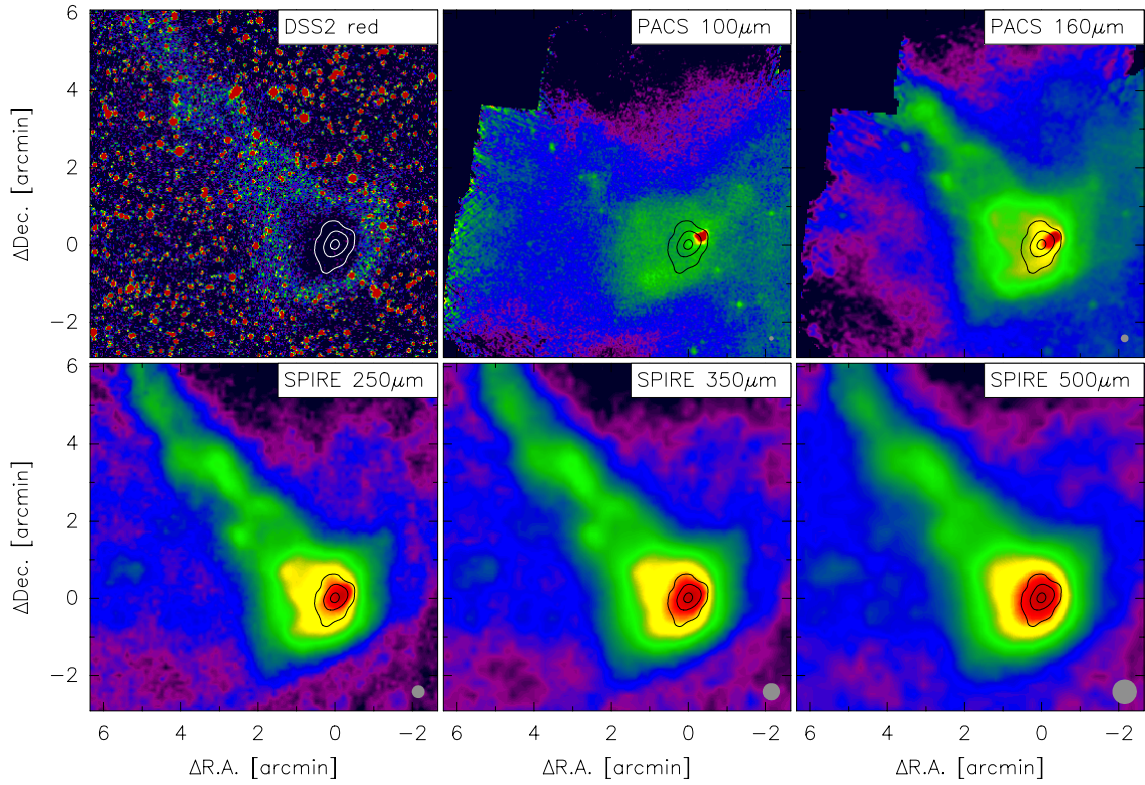
These figures are described and discussed in Sect. 5.2.
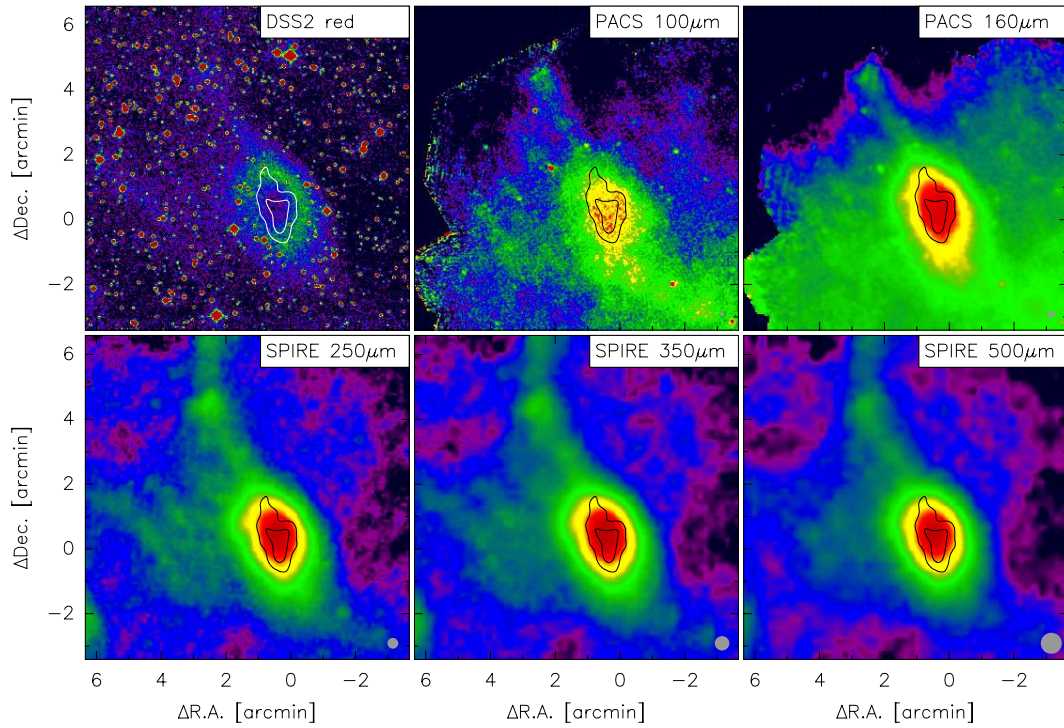
Fig. A.1. CB 4 (starless core): visual (red) DSS2 image and *Herschel* FIR maps (color; log scale) at 100, 160, 250, 350, and 500 μm, with 1.2 mm continuum contours overlaid (20 and 40 mJy/30″ beam). *Herschel* beam sizes are indicated as gray circles in the lower right corners.
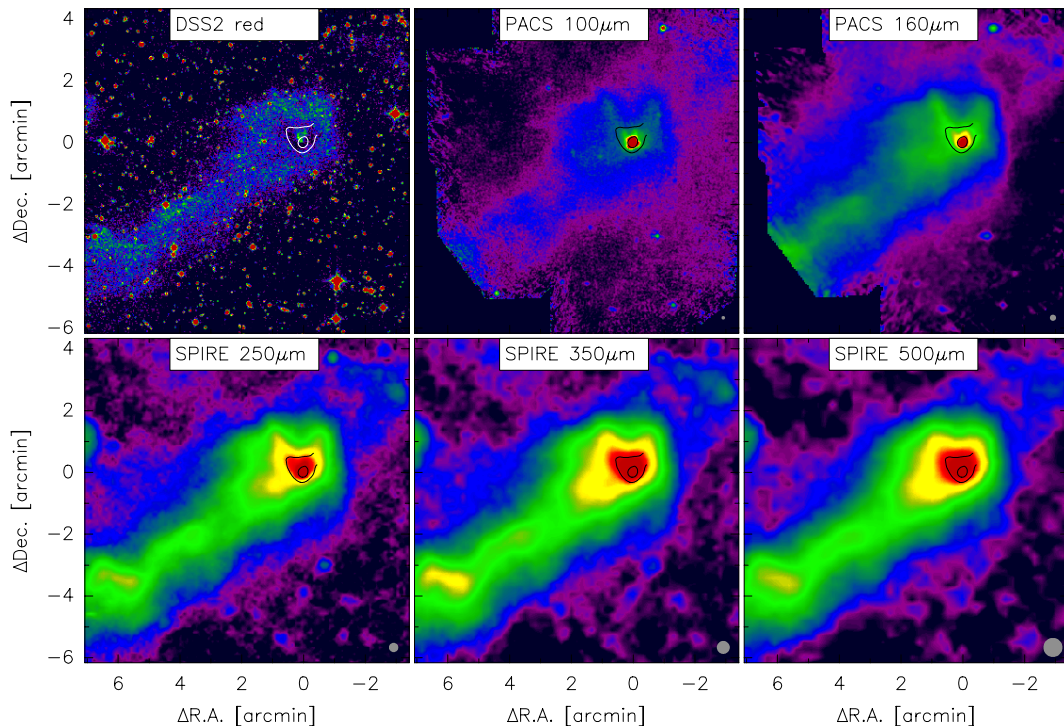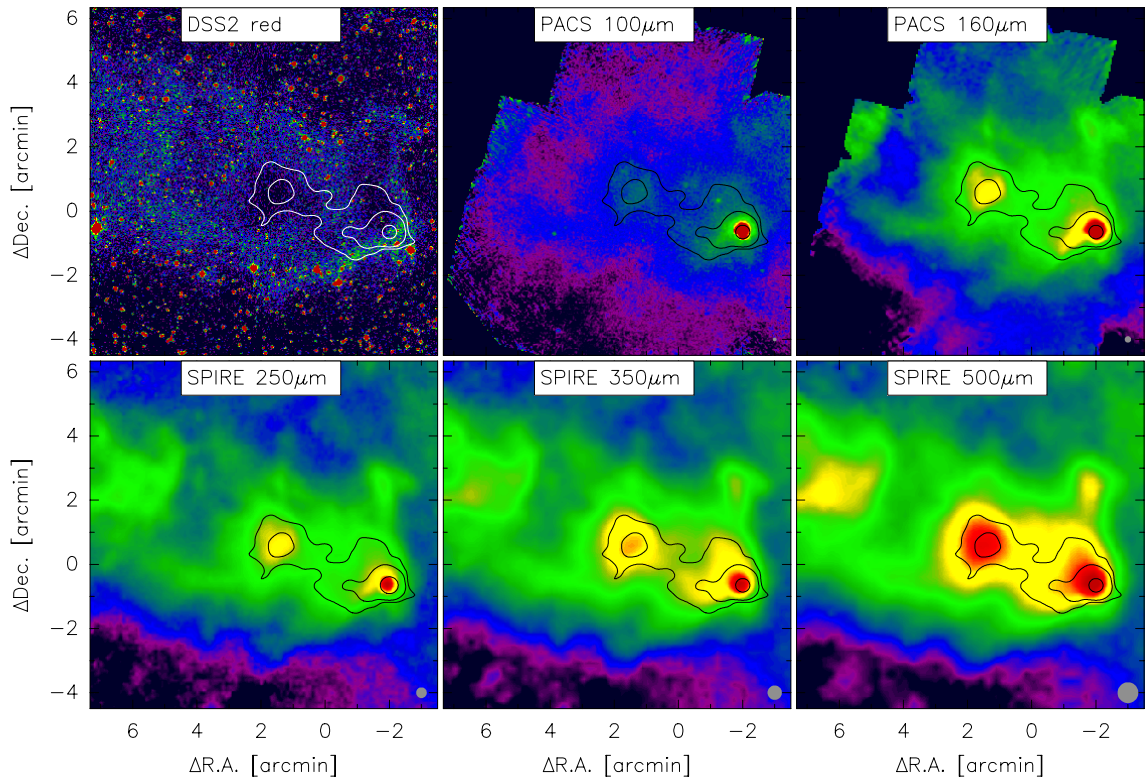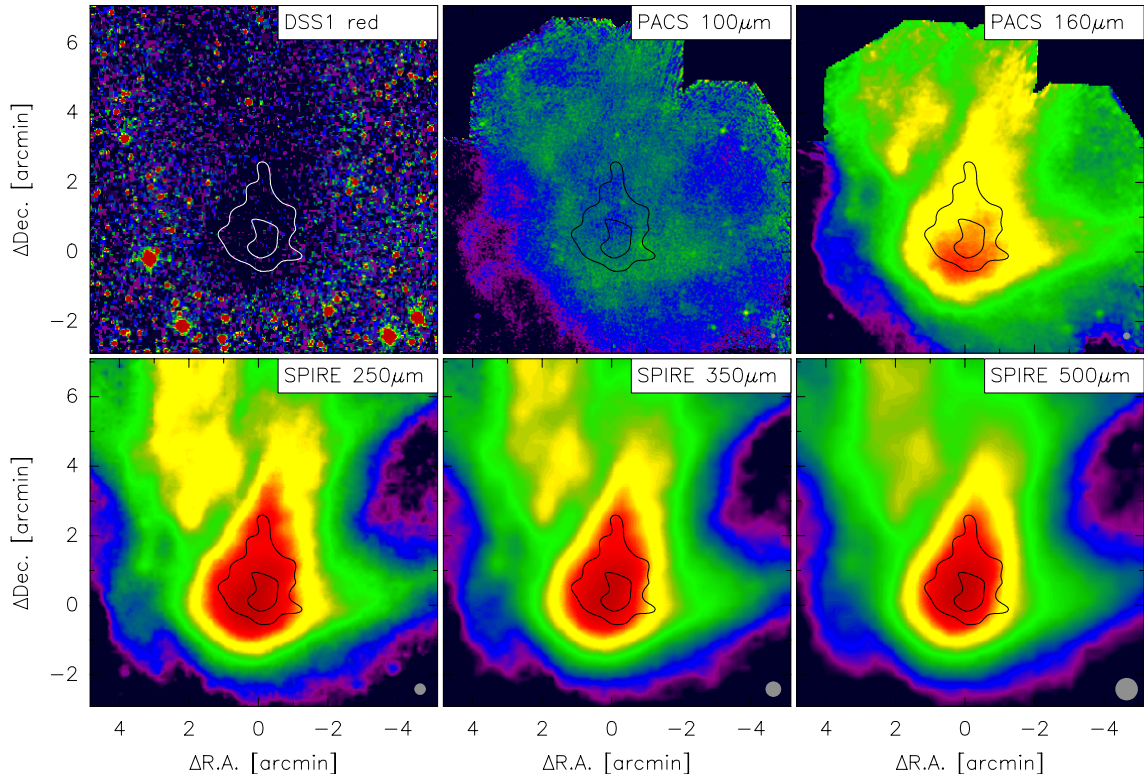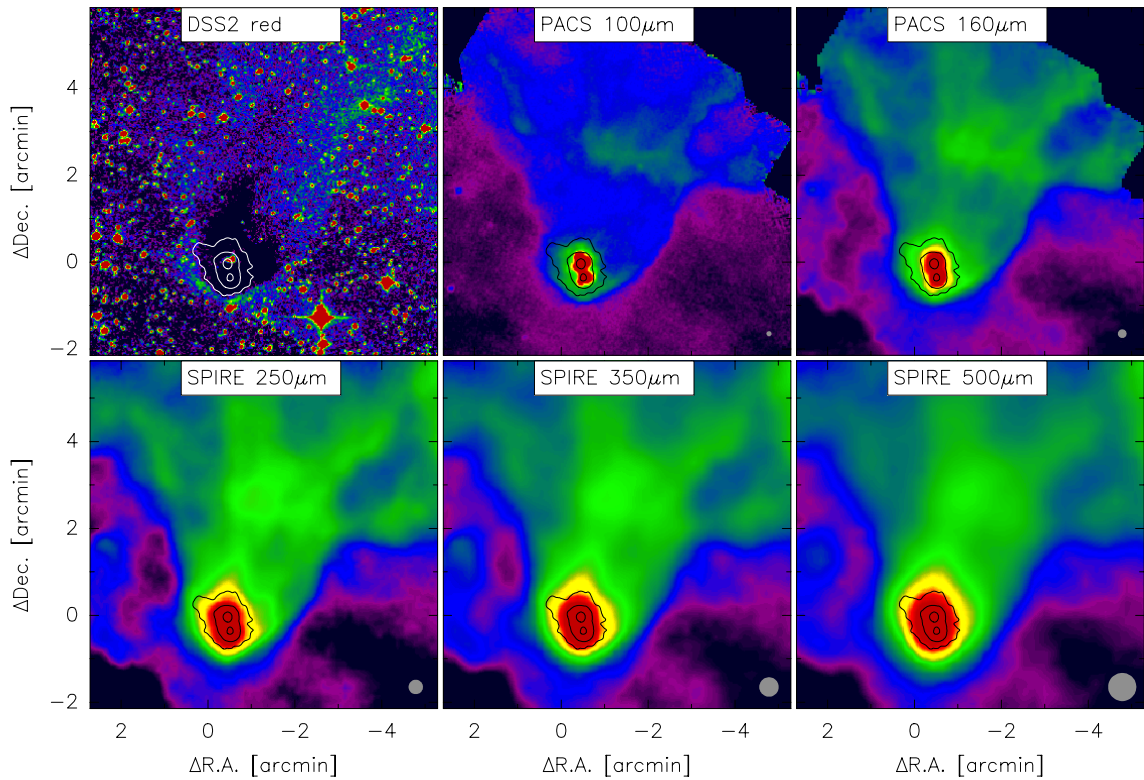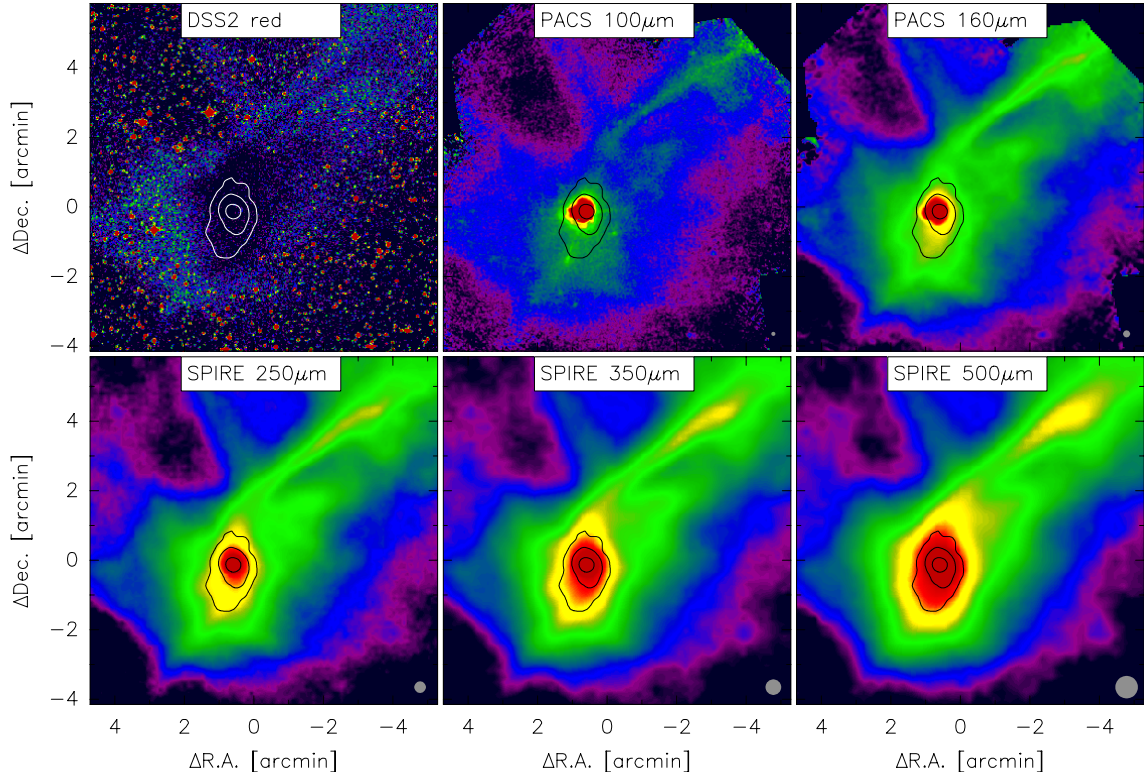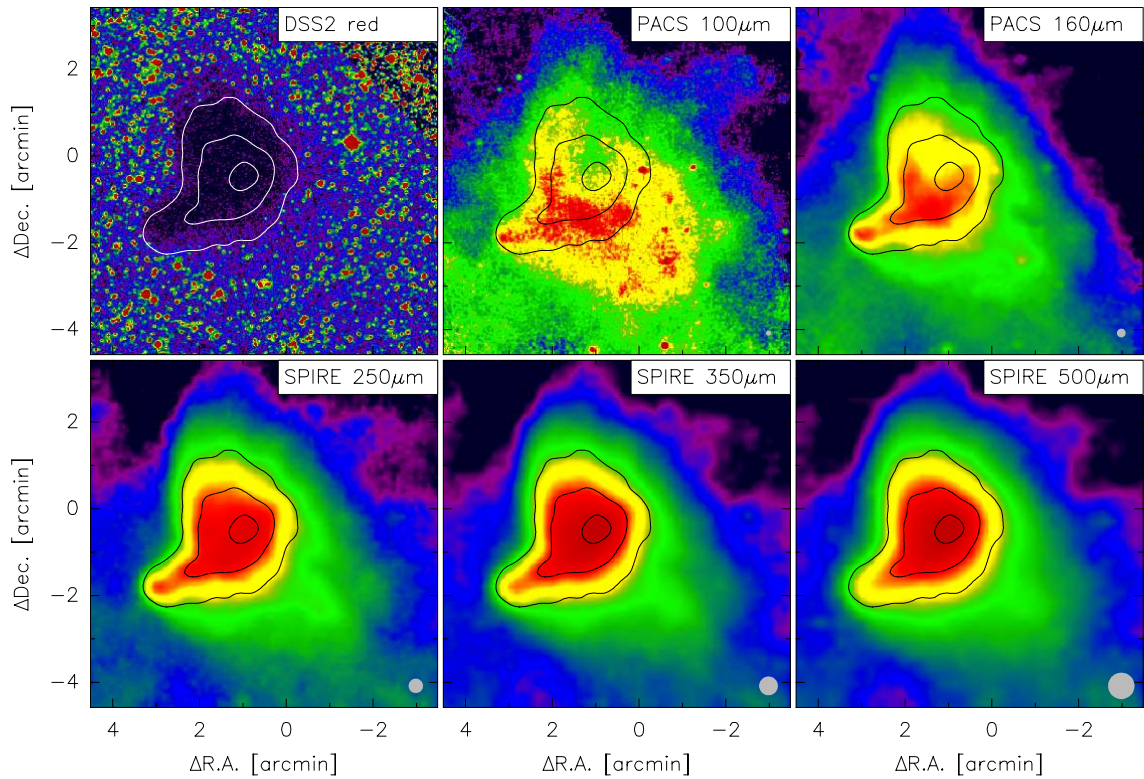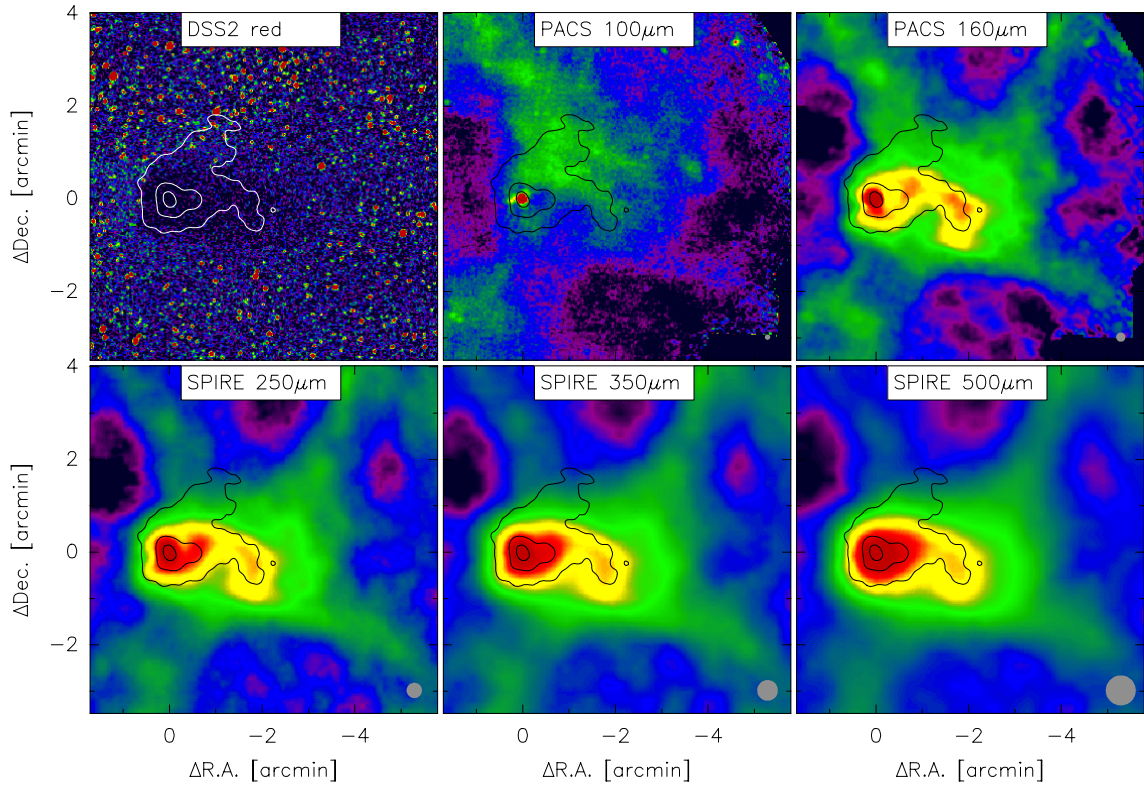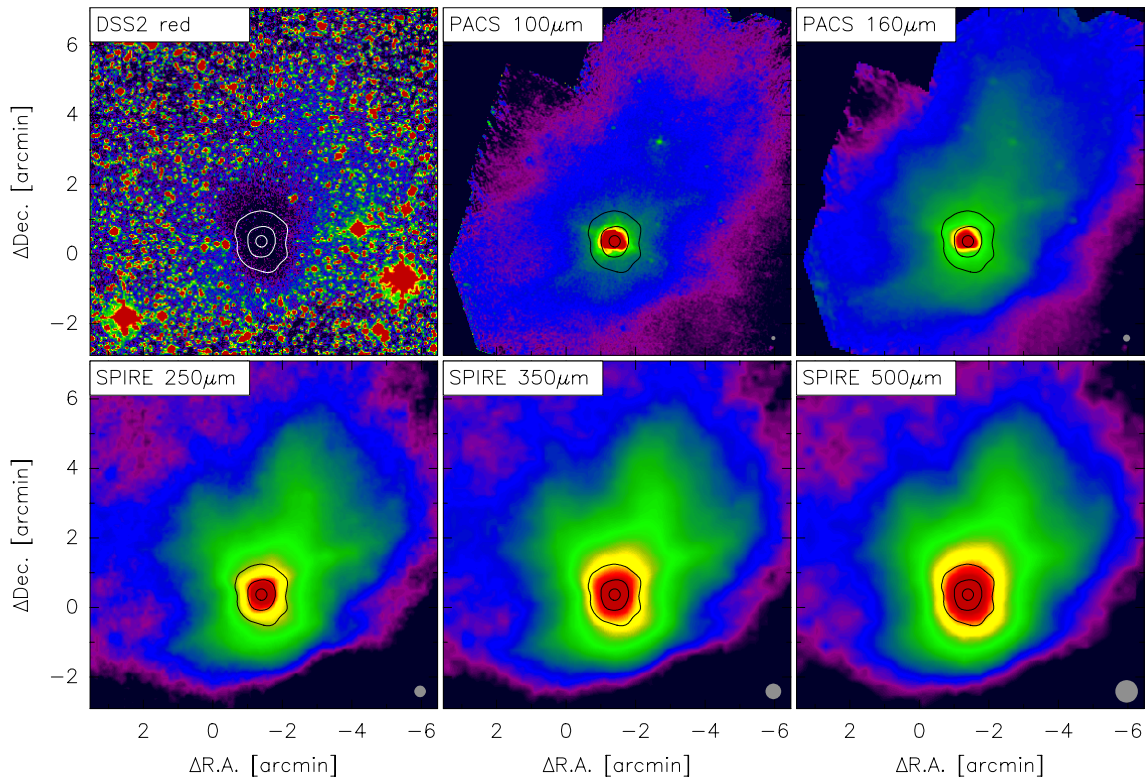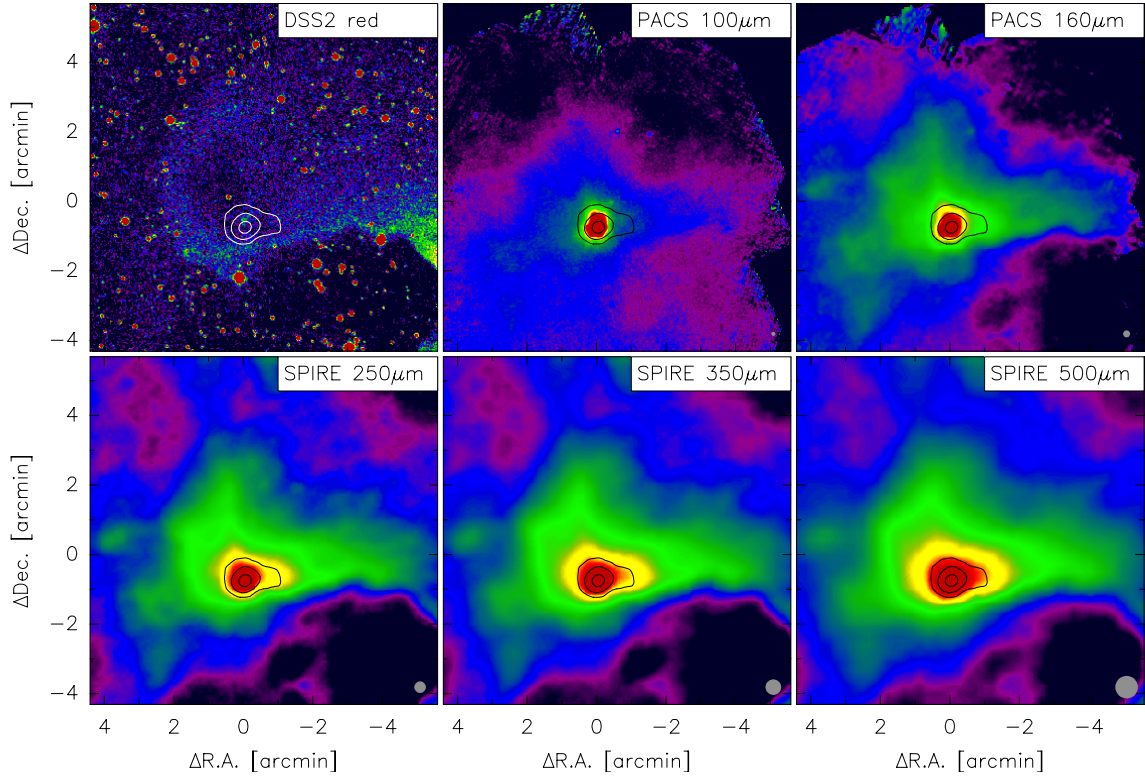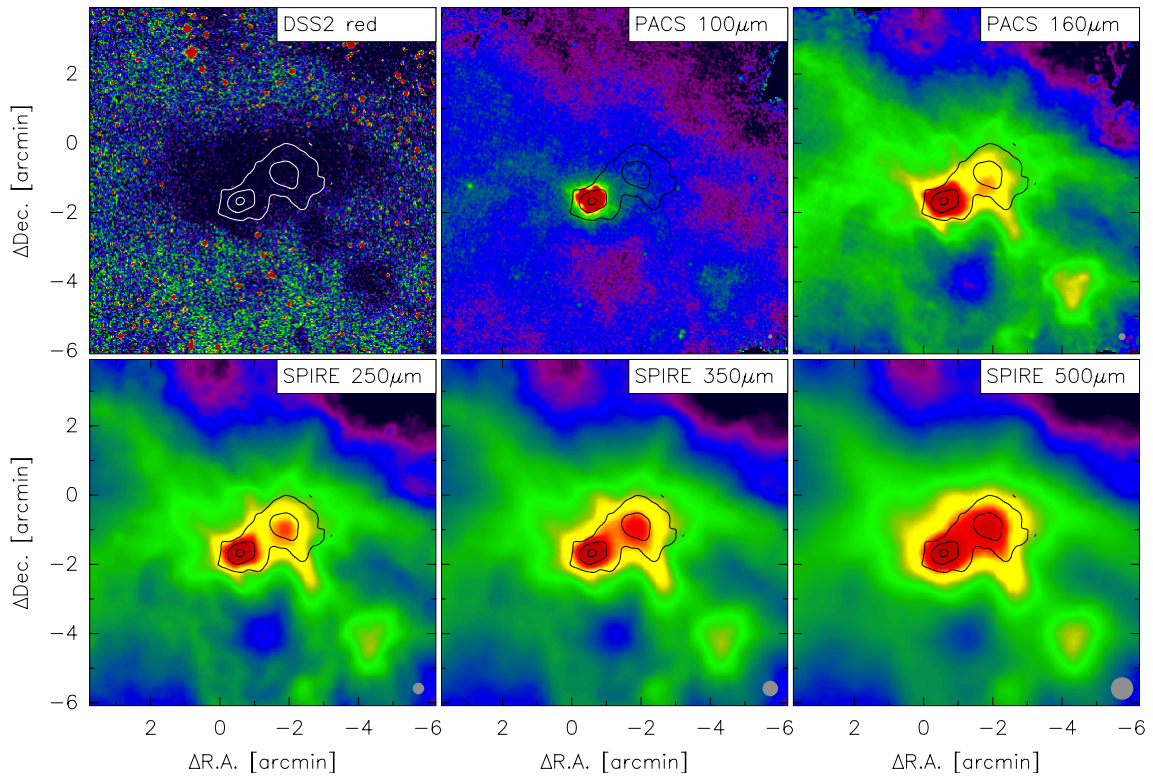

Fig. A.2. CB 6 (Class I YSO): visual (red) DSS2 image and *Herschel* FIR maps (color; log scale) at 100, 160, 250, 350, and 500 μm, with 850 μm continuum contours overlaid (180 and 300 mJy/20″ beam). *Herschel* beam sizes are indicated as gray circles in the lower right corners.

Fig. A.3. CB 17 (starless core and embedded Class I YSO): visual (red) DSS2 image and *Herschel* FIR maps (color; log scale) at 100, 160, 250, 350, and 500 μm, with 1.2 mm continuum contours overlaid (20, 40, and 65 mJy/20″ beam). *Herschel* beam sizes are indicated as gray circles in the lower right corners.

Fig. A.4. CB 26 (starless core and embedded Class I YSO): visual (red) DSS2 image and *Herschel* FIR maps (color; log scale) at 100, 160, 250, 350, and 500 μm, with 1.2 mm continuum contours overlaid (10, 26, and 150 mJy/30″ beam). *Herschel* beam sizes are indicated as gray circles in the lower right corners.

Fig. A.5. CB 27 (starless core): visual (red) DSS1 image and *Herschel* FIR maps (color; log scale) at 100, 160, 250, 350, and 500 μm, with 1.2 mm continuum contours overlaid (40 and 70 mJy/30″ beam). *Herschel* beam sizes are indicated as gray circles in the lower right corners.

Fig. A.6. BHR 12 (Class 0/I protostars): visual (red) DSS2 image and *Herschel* FIR maps (color; log scale) at 100, 160, 250, 350, and 500 μm, with 850 μm continuum contours overlaid (SCUBA; 120, 300, and 900 mJy/15″ beam). *Herschel* beam sizes are indicated as gray circles in the lower right corners.

Fig. A.7. CB 68 (Class 0 protostar): visual (red) DSS2 image and *Herschel* FIR maps (color; log scale) at 100, 160, 250, 350, and 500 μm, with 850 μm continuum contours overlaid (150, 300, and 600 mJy/20″ beam). *Herschel* beam sizes are indicated as gray circles in the lower right corners.

Fig. A.8. B 68 (starless core): visual (red) DSS2 image and *Herschel* FIR maps (color; log scale) at 100, 160, 250, 350, and 500 μm, with 870 μm continuum contours overlaid (40, 120, and 220 mJy/27″ beam). *Herschel* beam sizes are indicated as gray circles in the lower right corners.

Fig. A.9. CB 130 (Class 0 protostar): visual (red) DSS2 image and *Herschel* FIR maps (color; log scale) at 100, 160, 250, 350, and 500 μm, with 1.2 mm continuum contours overlaid (20, 60, and 100 mJy/20″ beam). *Herschel* beam sizes are indicated as gray circles in the lower right corners.

Fig. A.10. B 335 (Class 0 protostar): visual (red) DSS2 image and *Herschel* FIR maps (color; log scale) at 100, 160, 250, 350, and 500 μm, with 850 μm continuum contours overlaid (100, 300, and 900 mJy/20″ beam). *Herschel* beam sizes are indicated as gray circles in the lower right corners.

Fig. A.11. CB 230 (Class I YSO): visual (red) DSS2 image and *Herschel* FIR maps (color; log scale) at 100, 160, 250, 350, and 500 μm, with 850 μm continuum contours overlaid (70, 200, and 700 mJy/20″ beam). *Herschel* beam sizes are indicated as gray circles in the lower right corners.

Fig. A.12. CB 244 (Class 0 protostar and starless core): Visual (red) DSS2 image and *Herschel* FIR maps (color; log scale) at 100, 160, 250, 350, and 500 μm, with 1.2 mm continuum contours overlaid (30, 80, and 180 mJy/20″ beam). *Herschel* beam sizes are indicated as gray circles in the lower right corners.

Appendix B: Dust emission maps

These dust emission maps are described in Sect. 5.1.
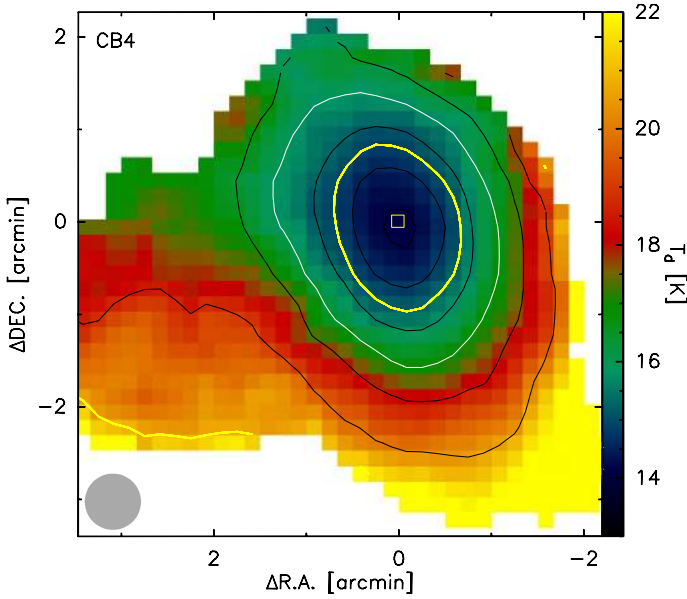
Fig. B.1. Dust temperature map of CB 4 (color scale), overlaid with contours of the hydrogen column density (white: 10^{21} cm^{-2}, black: 0.2, 0.5, 2, and 4×10^{21} cm^{-2}). Yellow contours mark N_{out} (Eq. (3)) and $N_{1'}$ (Eq. (10)). The yellow square marks the column density peak and the reference position listed in Table 5.
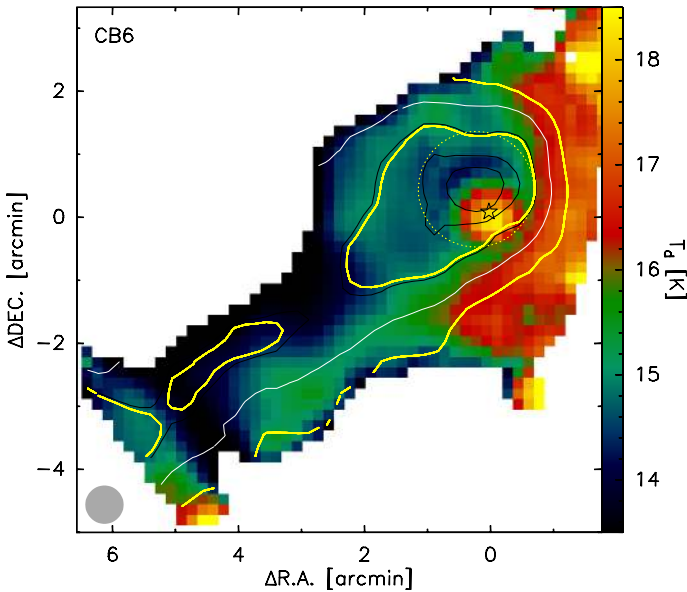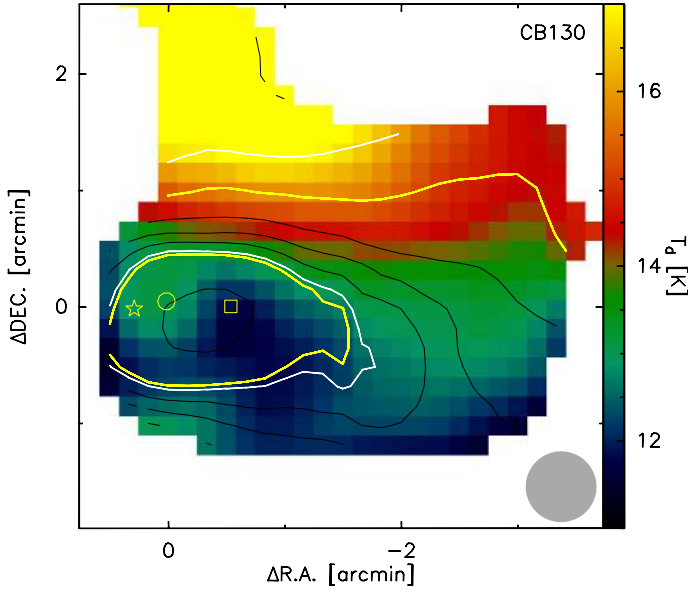

Fig. B.2. Dust temperature map of CB 6 (color scale), overlaid with contours of the hydrogen column density (white: 10^{21} cm^{-2}, black: 2, 4, and 6×10^{21} cm^{-2}). Yellow contours mark N_{out} (Eq. (3)) and $N_{1'}$ (Eq. (10)). The dotted yellow ellipse marks the $N_{1'}$ approximation described in Sect. 5.3. The asterisk marks the position of the embedded YSO.
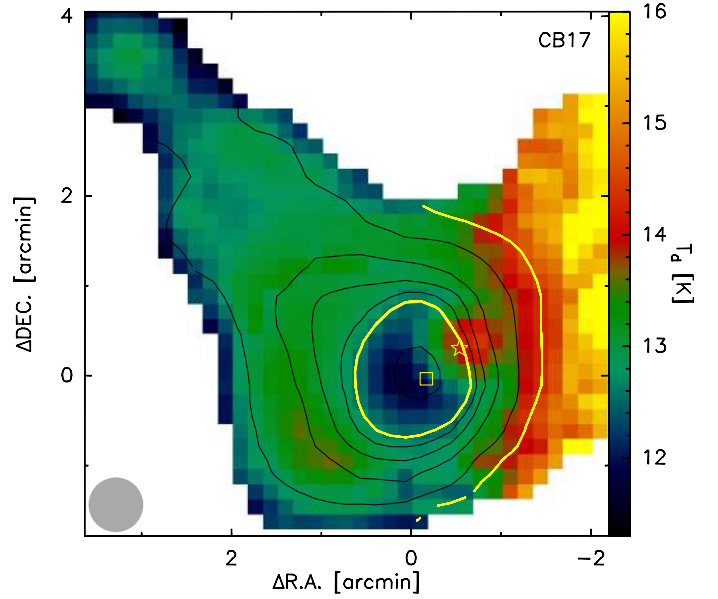
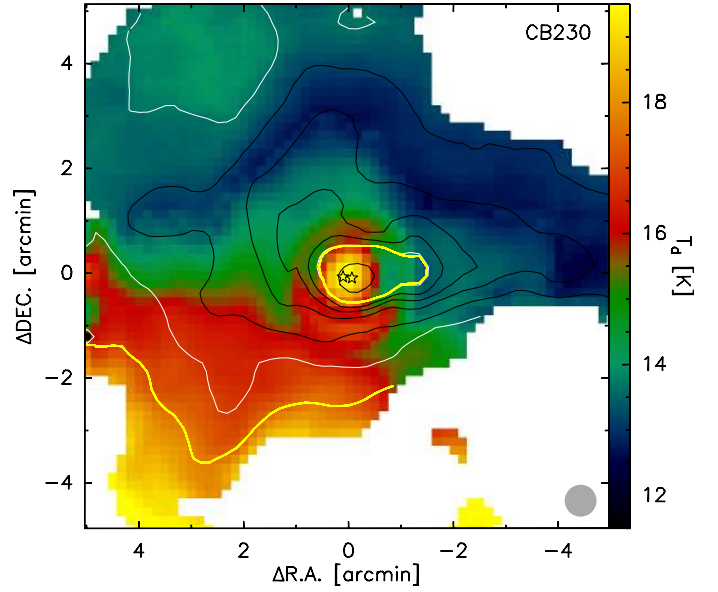**Fig. B.3.** Dust temperature map of CB 17 (color scale), overlaid with contours of the hydrogen column density (white: 10^{21} – masked by the yellow N_{out} contour – and 10^{22} cm^{-2}, black: 2, 4, 6, 8, and 20 $\times$ 10^{21} cm^{-2}). Yellow contours mark N_{out} (Eq. (3)) and $N_{1'}$ (Eq. (10)). The yellow square marks the column density peak and position of CB 17-SMM. The asterisk marks the position of CB 17-IRS (Table 5; see also Launhardt et al. 2010).
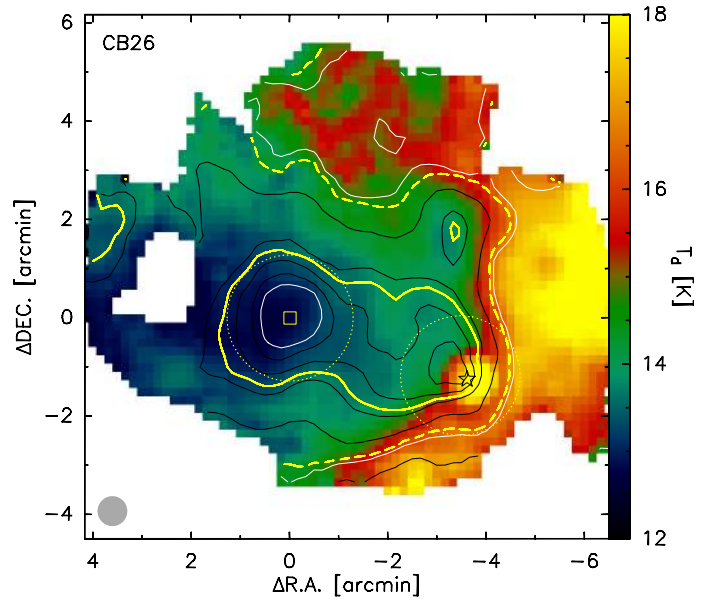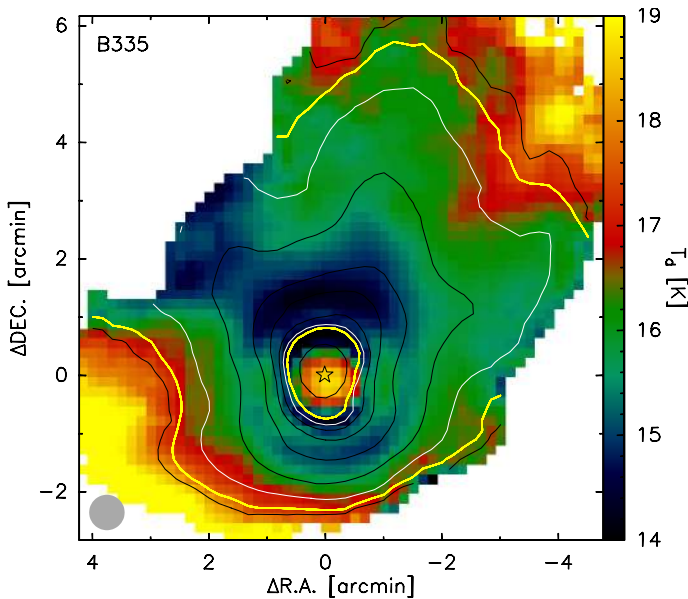

Fig. B.4. Dust temperature map of CB 26 (color scale), overlaid with contours of the hydrogen column density (white: 10^{21} and 10^{22} cm^{-2}, black: 0.5, 2, 4, 6, and 8×10^{21} cm^{-2}). Yellow contours mark N_{out} (Eq. (3)) and $N_{1'}$ (Eq. (10), referring to the starless core SMM2). Dotted yellow ellipses mark the $N_{1'}$ approximations for the two subcores described in Sect. 5.3. The yellow square marks the column density peak and position of CB 26-SMM2; the asterisk marks the position of CB 26-SMM1 (Table 5).
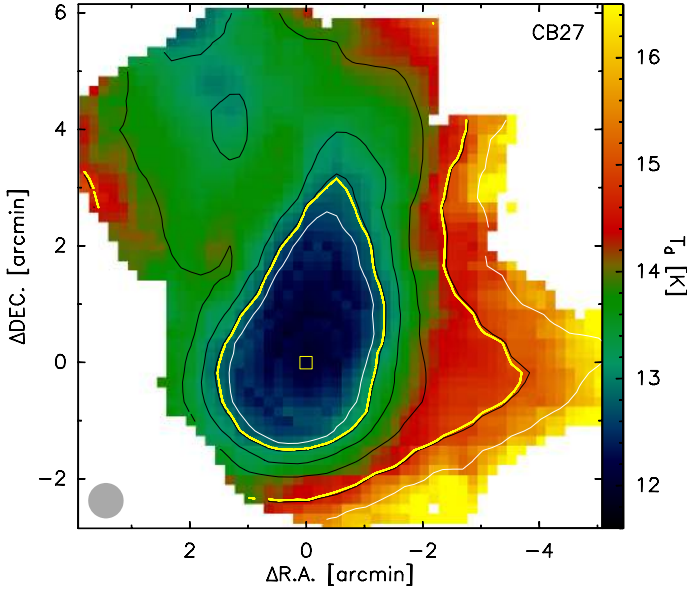
Fig. B.5. Dust temperature map of CB 27 (color scale), overlaid with contours of the hydrogen column density (white: 10^{21} and 10^{22} cm^{-2}, black: 2, 4, 6, and 8×10^{21} cm^{-2}). Yellow contours mark $N_{\rm out}$ (Eq. (3)) and $N_{1'}$ (Eq. (10)). The yellow square marks the column density peak and the reference position listed in Table 5.
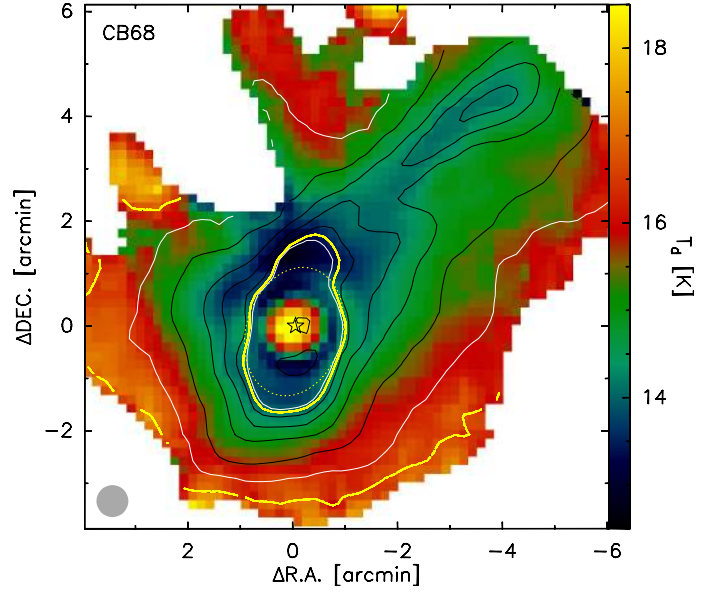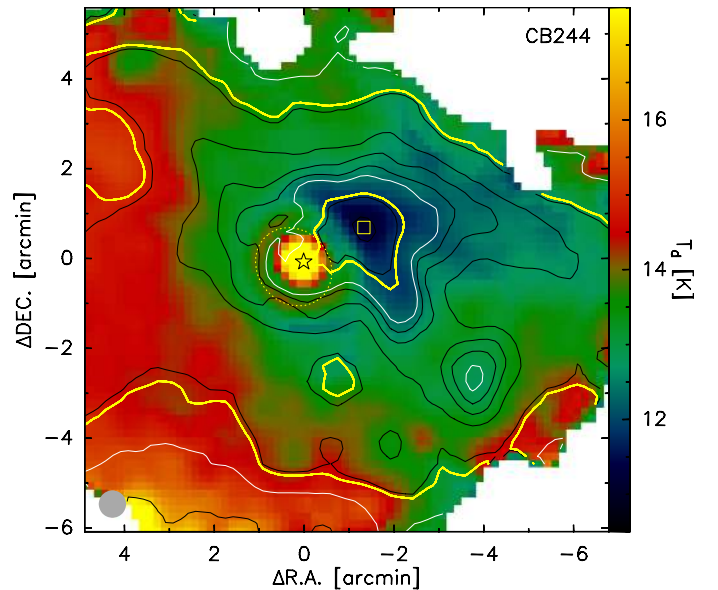

Fig. B.7. Dust temperature map of CB 68 (color scale), overlaid with contours of the hydrogen column density (white: 10^{21} and 10^{22} cm^{-2}, black: 0.5 – masked by yellow $N_{\rm out}$ contour – 2, 4, 6, 8, and 20×10^{21} cm^{-2}). Yellow contours mark $N_{\rm out}$ (Eq. (3)) and $N_{1'}$ (Eq. (10)). The dotted yellow ellipse marks the $N_{1'}$ approximation described in Sect. 5.3. The asterisk marks the position of the protostar and the reference position listed in Table 5.
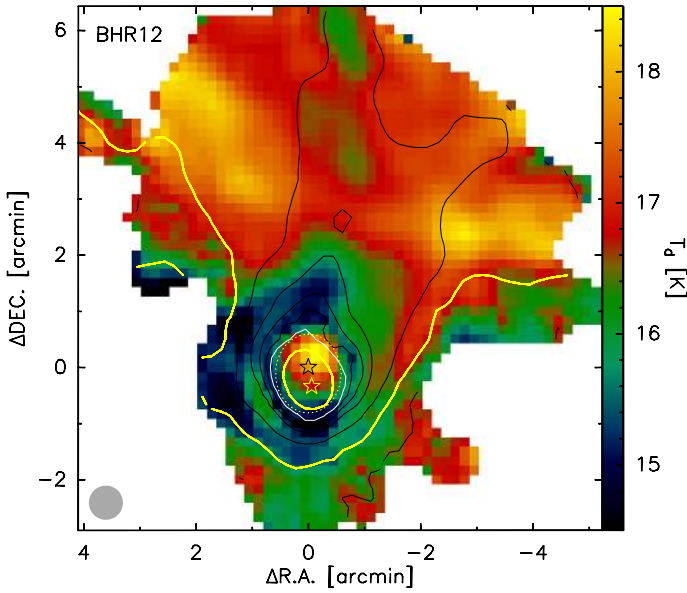
Fig. B.6. Dust temperature map of BHR 12 (color scale), overlaid with contours of the hydrogen column density (white: 10^{21} – masked by yellow $N_{\rm out}$ contour – and 10^{22} cm^{-2}, black: 0.5, 2, 4, 6, 8, and 20×10^{21} cm^{-2}). Yellow contours mark $N_{\rm out}$ (Eq. (3)) and $N_{1'}$ (Eq. (10)). The dotted yellow ellipse marks the $N_{1'}$ approximation described in Sect. 5.3. The two asterisks mark the positions of embedded sources SMM1 and SMM2 (see Launhardt et al. 2010).
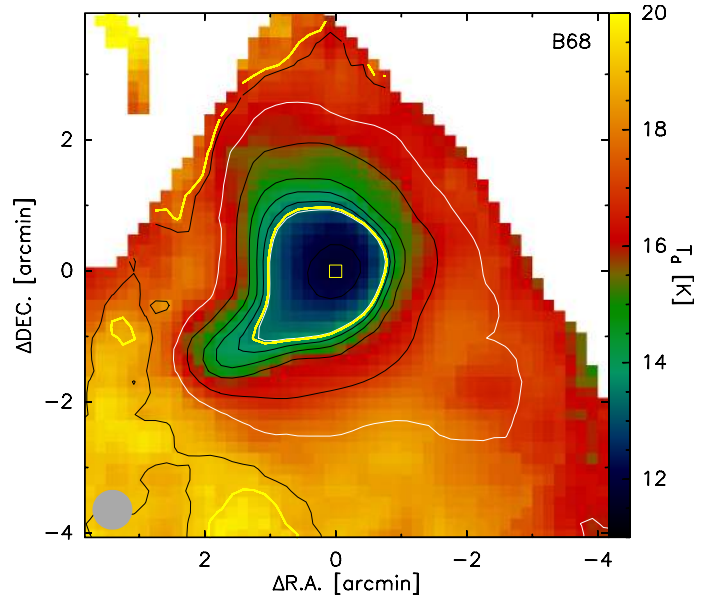

Fig. B.8. Dust temperature map of B 68 (color scale), overlaid with contours of the hydrogen column density (white: 10^{21} and 10^{22} cm^{-2}, black: 0.5, 2, 4, 6, 8 and 20×10^{21} cm^{-2}). Yellow contours mark $N_{\rm out}$ (Eq. (3)) and $N_{1'}$ (Eq. (10)). The yellow square marks the column density peak and the reference position listed in Table 5.

Fig. B.9. Dust temperature map of CB 130 (color scale), overlaid with contours of the hydrogen column density (white: 10^{21} and 10^{22} cm^{-2}, black: 0.5, 2 – masked by yellow N_{out} contour – 4, 6, 8, and 20 × 10^{21} cm^{-2}). Yellow contours mark N_{out} (Eq. (3)) and $N_{1'}$ (Eq. (10)). The yellow circle marks the position of the protostellar core CB 130-SMM1 with the embedded Class 0 VeLLO. The yellow square marks the position of the secondary starless core CB 130-SMM2. The asterisk marks the position of the Class I-II YSO CB 130-IRS, which most likely associated with CB 130, but not embedded in its dense core (see Launhardt et al. 2010).

Fig. B.10. Dust temperature map of B 335 (color scale), overlaid with contours of the hydrogen column density (white: 10^{21} and 10^{22} cm^{-2}, black: 0.5, 2, 4, 6, 8, and 20 × 10^{21} cm^{-2}). Yellow contours mark N_{out} (Eq. (3)) and $N_{1'}$ (Eq. (10)). The asterisk marks the position of the protostar and the reference position listed in Table 5.

Fig. B.11. Dust temperature map of CB 230 (color scale), overlaid with contours of the hydrogen column density (white: 10^{21} and 10^{22} cm^{-2}, black: 2, 4, 6, 8, and 20 × 10^{21} cm^{-2}). Yellow contours mark N_{out} (Eq. (3)) and $N_{1'}$ (Eq. (10)). The two asterisks mark the positions of the embedded YSOs (see Launhardt et al. 2010).

Fig. B.12. Dust temperature map of CB 244 (color scale), overlaid with contours of the hydrogen column density (white: 10^{21} and 10^{22} cm^{-2}, black: 0.5, 2, 4, 6, 8, and 20 × 10^{21} cm^{-2}). Yellow contours mark N_{out} (Eq. (3)) and $N_{1'}$ (Eq. (10)) for the starless core CB 244-SMM2. The dotted yellow ellipse marks the $N_{1'}$ approximation for CB244-SMM1 described in Sect. 5.3. The yellow square marks the column density peak of CB 244-SMM2 and the reference position listed in Table 5. The asterisk marks the position of of the protostar CB244-SMM1.
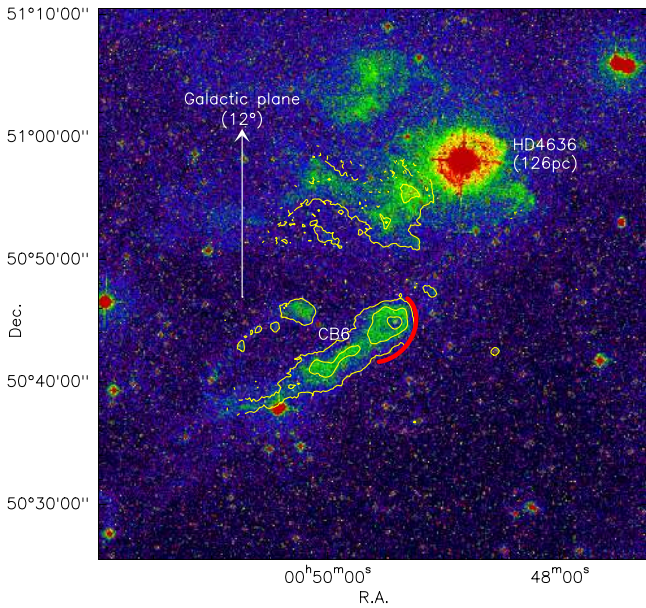
Appendix C: Images on large-scale morphology

These optical images on the larger-scale morphology of the globules are discussed in Sect. 5.8.
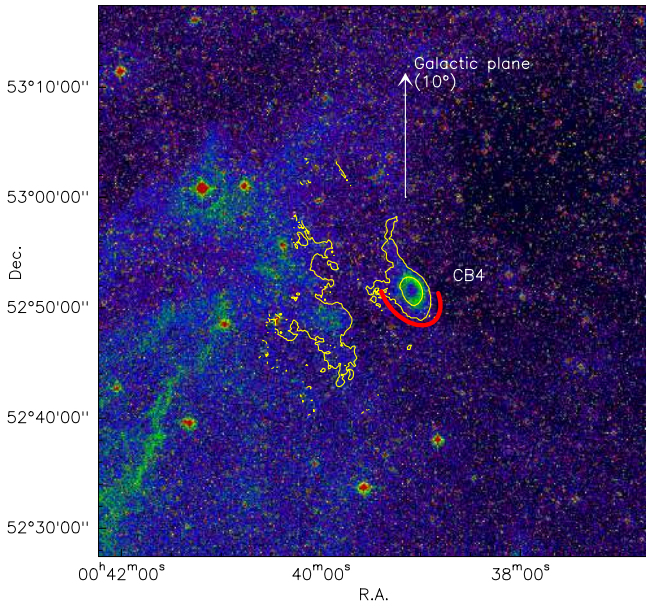
Fig. C.1. CB 4: visual (red) DSS2 image with SPIRE 500 μm continuum contours overlaid. The red arc marks the warm rim of CB 4.
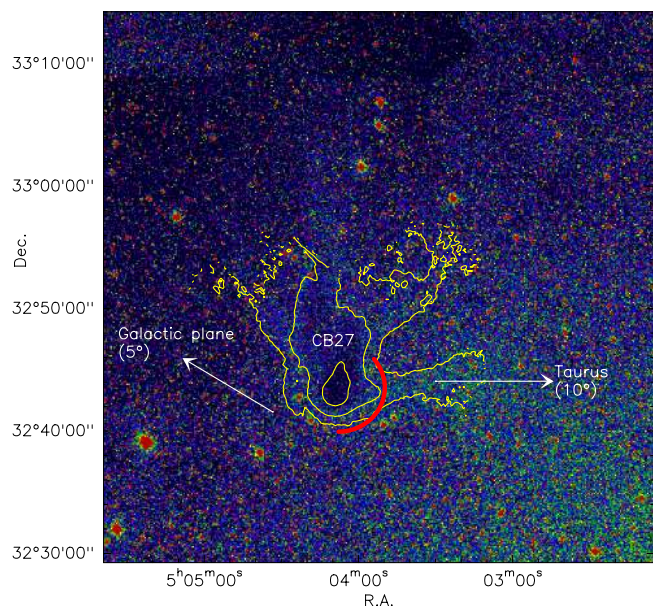

Fig. C.2. CB 6: visual (red) DSS2 image with SPIRE 500 μm continuum contours overlaid. The red arc marks the warm rim of CB 6.
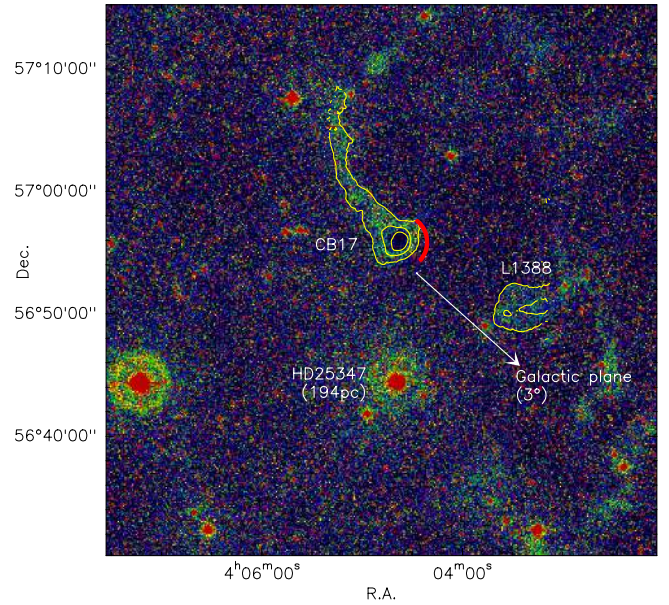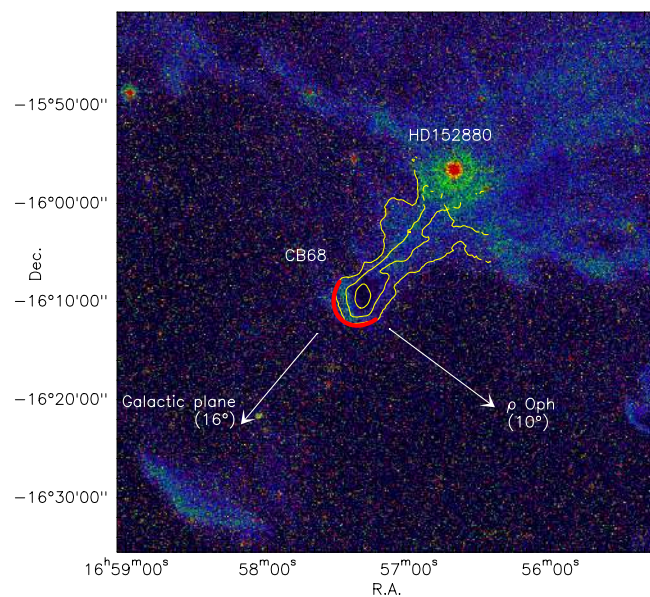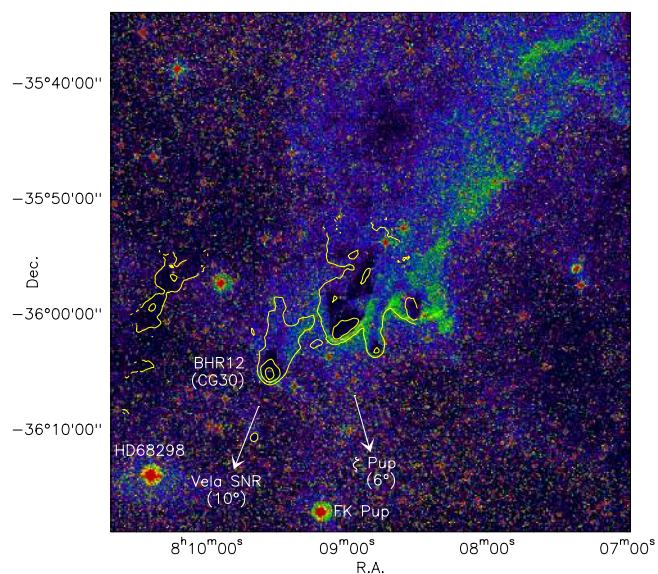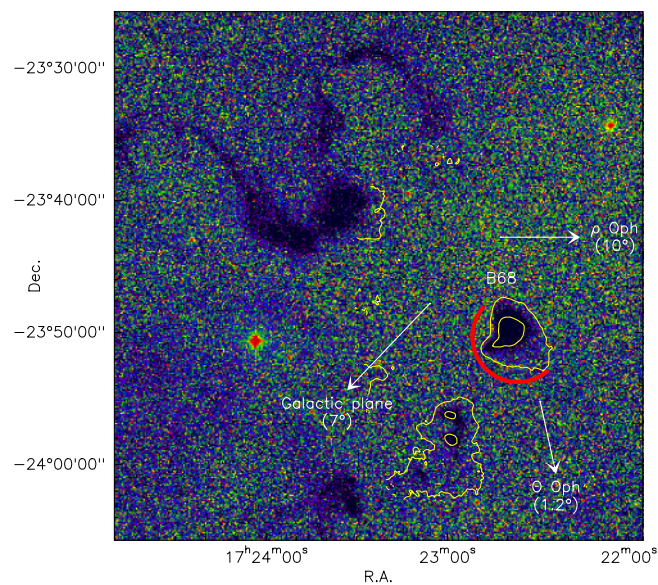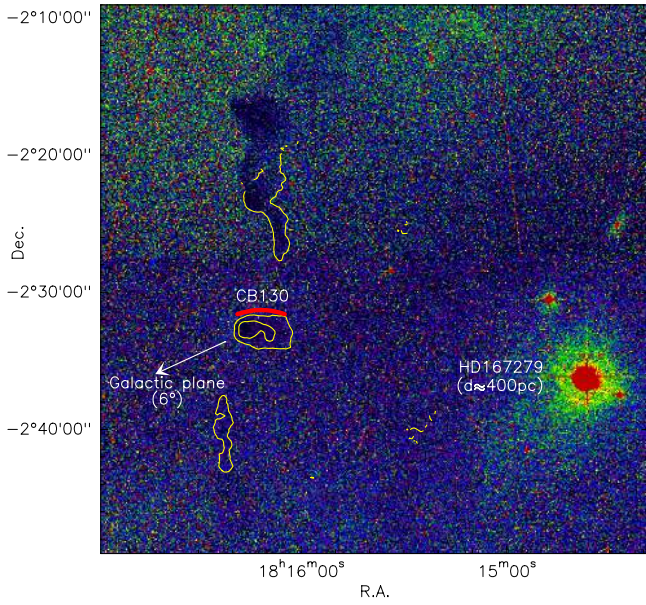

Fig. C.3. CB 17: visual (red) DSS2 image with SPIRE 500 μm continuum contours overlaid. The red arc marks the warm rim of CB 17.
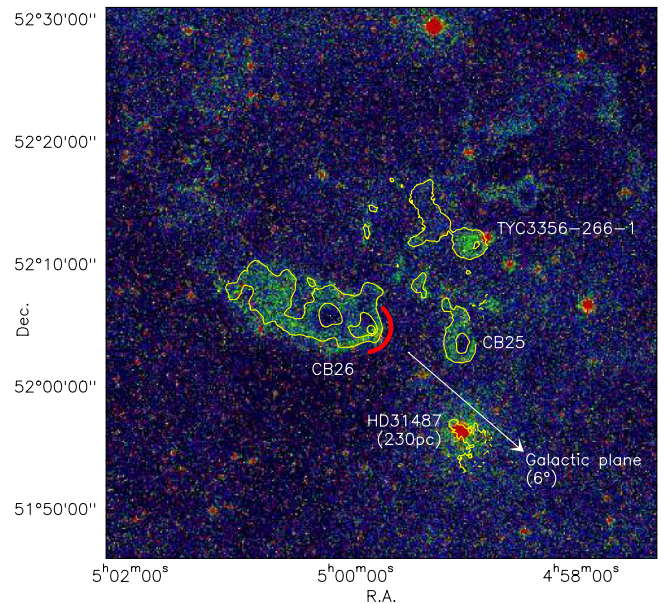
Fig. C.4. CB 26: visual (red) DSS2 image with SPIRE 500 μm continuum contours overlaid. The red arc marks the warm rim of CB 26.

Fig. C.5. CB 27: visual (red) DSS1 image with SPIRE 500 μm continuum contours overlaid. The red arc marks the warm rim of CB 27.

Fig. C.7. CB 68: visual (red) DSS2 image with SPIRE 500 μm continuum contours overlaid. The red arc marks the warm rim of CB 68.
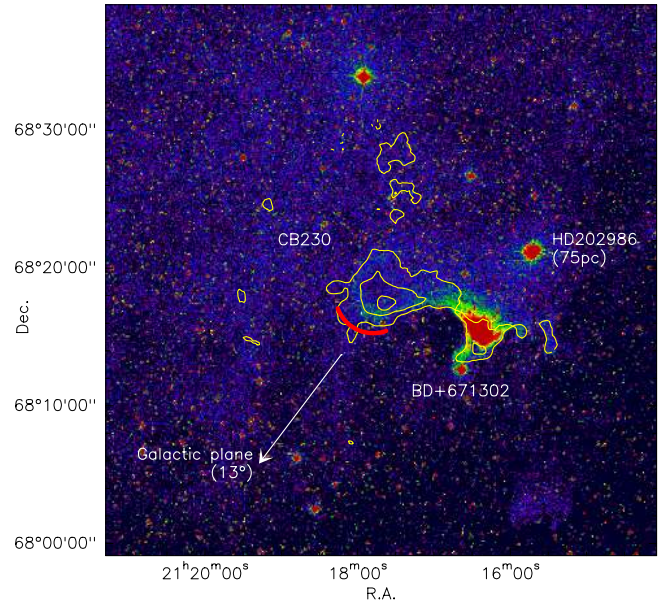

Fig. C.6. BHR 12: visual (red) DSS2 image with SPIRE 500 μm continuum contours overlaid. The tail side is warmer than the head side, but there is nor clear warm rim side.

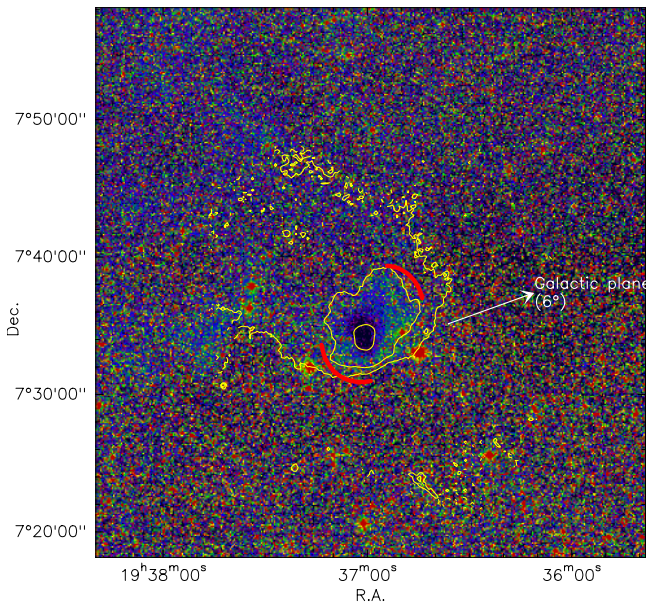**Fig. C.8.** B 68: visual (red) DSS1 image with SPIRE 500 μm continuum contours overlaid. The red arc marks the warm rim of B 68. The B2 IV star Θ Oph is located at a distance from the Sun of 134 pc, i.e., its physical distance from B 68 is only $\approx$2.8 pc.
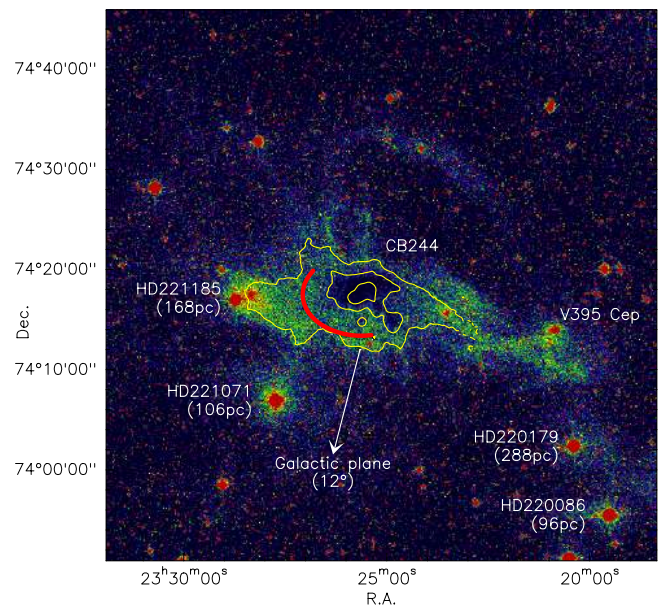
Fig. C.9. CB 130: visual (red) DSS2 image with SPIRE 500 μm continuum contours overlaid. The red arc marks the warm rim of CB 130.

Fig. C.11. CB 230: visual (red) DSS2 image with SPIRE 500 μm continuum contours overlaid. The red arc marks the warm rim of CB 230.

Fig. C.10. B 335: visual (red) DSS2 image with SPIRE 500 μm continuum contours overlaid. The red arc marks the warm rim of B 335.

Fig. C.12. CB 244: visual (red) DSS2 image with SPIRE 500 μm continuum contours overlaid. The red arc marks the warm rim of CB 244.